

Table des matières

Concepts and preliminaries	1
Propulsion system for spacecrafts	1
Hall effect Thruster (HET) research and development with Safran	6
Key phenomena of HETs	6
Plasma models and simulations	7
Problematic	9
1 Particle-In-Cell simulations of HETs	11
1.1 The Hall effect Thruster	12
1.1.1 Operating principle	14
1.1.2 Electron drift and azimuthal instability	15
1.1.3 Plasma-wall interaction	15
1.1.4 Cross field transport of the elections	16
1.1.5 Three-dimensional physics	16
1.2 Elements of the 2D PIC-MCC simulations	17
1.2.1 Principe of the PIC simulations	17
1.2.2 Monte Carlo collisions	17
1.3 Numerical implementation of the Particle in cell simulation	17
1.3.1 Data used	19
1.3.2 Particle pusher	20
1.3.3 Poisson equation solver	21
1.4 Bidimentional simulation of an HET	21
1.4.1 Neglecting curvature	21
1.4.2 Radial-azimuthal domain description	21
1.4.3 Particle balance	22
1.4.4 Axial convection	22
1.5 Dielectrics boundary condition	23
1.5.1 Non-uniform mesh	23
1.5.2 Poisson equation discretization	24
1.5.3 Poisson equation discretization	25
1.5.4 Including surfaces charges	26
1.5.5 Verifications	27
1.5.6 Interface at the cell centre	27
1.5.7 Surface charges for centred interface	29
1.6 Axial Convection model	29
1.6.1 Lafleur's model of convection	29

1.6.2	Numerical artefacts	31
1.6.3	Numerical noise of Lafleur's convection model	33
1.6.4	Effect of the noise on the electric field	34
1.6.5	Noiseless convection model	35
1.6.6	Effects on a 2 dimensions (2D) simulation domain	37
1.7	Secondary electron emission	38
1.7.1	Models of emission	39
1.7.2	Electron emission model used	39
1.8	Electron cross-field transport	40
1.9	Sheath model with electron emission	42
1.10	Conclusion	43
2	Parametric study of the dielectric characteristics	45
2.1	Simulation parameters	46
2.2	Canonical simulation results	46
2.2.1	Initial phase	46
2.2.2	Stable phase	48
2.2.3	Enhanced electron transport	48
2.3	Modeling the dielectric layer	51
2.3.1	Effect of the dielectric layer	52
2.3.2	Near wall parameters	52
2.3.3	Dielectric model comparison	54
2.4	Effect of electron emission	54
2.4.1	Impact of the electron emission on the mobility	56
2.4.2	Near wall conductivity	57
2.4.3	Three different regimes	57
2.5	Validation of the sheath model	60
2.6	Full dielectric model	62
2.7	Conclusion	63
3	Anisothermal sheath	65
3.1	Insights for the PIC simulations	66
3.1.1	Electron distribution function	66
3.1.2	Radial evolution of the electron temperature	67
3.2	Simplified 1D for the PIC simulations	69
3.2.1	Description on the simulations	69
3.2.2	Simulation results	70
3.2.3	A model for the EVDF	71
3.3	Collisionless kinetic model and polytropic state law	74
3.3.1	Vlasov equation for the sheath	74
3.3.2	Polytropic state law for the electrons	75
3.3.3	Evolution of the polytropic index	78
3.3.4	Coulomb collision and improvements	79
3.4	Monte Carlo model	79
3.4.1	Description of the Monte Carlo approach	79
3.4.2	Results	81
3.5	Non-isothermal fluid model	83

3.5.1	Comparison with the PIC simulations	84
3.5.2	Modified Bohm criterion	84
3.5.3	Plasma potential drop to the wall	85
3.5.4	Power losses at the wall	87
3.6	Conclusion	89
3.6.1	Realistic heating and ionization	89
A	Bibliographie	93

Acronyms

HET Hall effect Thruster

PIC Particle in Cell

MCC Monte Carlo Collision

DK Direct Kinetic

LPP Laboratoire de Physique des plasmas

A laboratory from Ecole polytechnique, Palaiseau, France .

Xe Xenon

Kr Krypton

3V 3 dimension for the velocity

2D 2 dimensions

3D 3 dimensions

1D 1 dimension

BNSiO₂ Boron Nitride-Silicon Dioxide. A ceramic composed of a mix of Boron Nitride and Silicon Dioxide.

ECDI Electron cyclotron drift instability. Another name of the EDI present in HET.

EDI $E \times B$ electron drift instability. Another name of the ECDI present in HET.

IAW Ion Acoustic Wave

NWC Near-Wall Conductivity. Increased cross-field transport due to electron-wall collision and electron emissions from the wall.

SEE Secondary Electron Emission. Electron emission from a wall due to an energetic impact of a primary electron.

FT Fourier Transform

FFT Fast Fourier Transform

DFT Discrete Fourier Transform

BC Boundary Conditions

EP Electric Propulsion. Propulsion engines using the electric energy, instead of the chemical energy.

CNES Centre National d'Etude Spatial. The French space agency

ML Laboratory Model

EEDF Electron Energy Distribution Function

SCL Space Charge Limit

RMS Root Mean Square

RF Radio Frequency

LEO Low Earth Orbit

The LEO corresponds to orbits of altitude lower than 2000 km. Mostly used for Earth observation, and the ISS.

GEO GEostationary Orbit

Corresponds to the Orbit that follows the Earth rotation. Used mainly for telecommunication (Like the French Canal (former Canalsat)), it lies at 36000km from the Earth.

Nomenclature and List of Symbols

Numerical Implementation

Dirichlet Boundary condition: a type of boundary conditions for which the field is fixed. For instance for grounded electrodes on the plasma potential: $\phi = 0$

Physics Constants

g_0	Standard gravity	9.80665 m/s ²
-------	------------------	--------------------------

Quantities

I_{sp}	Specific impulse, related to the exhaust velocity of a propellant
λ	Wave length
μ_e	Electron mobility
\mathcal{N}	Normal distribution.
ν_m	electron-neutral momentum transfer collision frequency
ω_{ce}	Electron cyclotron frequency $\omega_{ce} = \frac{eB}{m_e}$
ρ	Charge density
σ_{Reinj}	standard deviation of the distribution of the noise associated with the convection model
\mathbf{v}_i	ion velocity vector
c_s	ion sound speed $c_s = (eT_e/m_i)^{1/2}$
E_θ	Azimuthal electric field
L_z	Axial length
M	mass of a spacecraft
T	thrust
t	time
U_z	total potential difference in the axial direction $U_z = E_z L_z$
$u_{e,z}$	Electron mean velocity in the axial direction : $u_{e,z} = \langle v_{e,z} \rangle$
u	Electron mean velocity
Delta-V	Measure of impulse needed for a space manoeuvre

Concepts and preliminaries

The Earth is the cradle of humanity, but mankind cannot stay in the cradle forever.

Konstantin Tsiolkovsky, pioneer of the astronautic theory

Contents

Propulsion system for spacecrafts	1
HET research and development with Safran	6
Key phenomena of HETs	6
Plasma models and simulations	7
Problematic	9

Propulsion system for spacecrafts

In order to move in space, the satellites, scientific probes and spacecrafts in general rely on a propulsion system. The cost to go from one location to another can be expressed as *Delta-V*, a measure of impulse needed to perform a manoeuvre. Figure 1 illustrates the Delta-V needed to evolve in the solar system. We can see that reaching Low Earth Orbit (**LEO**) needs a Delta-V of 9400 m/s, while the GEostationary Orbit (**GEO**) is 3910 m/s further. Landing on the Moon requires a total of 15 km/s away from the Earth ground, while landing on Neptune require 43.7 km/s of impulse.

For a spacecraft of instantaneous mass $M(t)$, with a propulsion system generating an instantaneous thrust $T(t)$, the Delta-V between t_1 and t_2 is

$$\text{Delta-V} = \int_{t_1}^{t_2} \frac{|T(t)|}{M(t)} dt. \quad (1)$$

Unsurprisingly, we see from Eq. (1) that for a more massive spacecraft, a more intense, or a longer thrust is needed in order to obtain the same Delta-V.

Rocket equation

The thrust T generated by ejecting mass at high velocity is

$$T = v_{\text{ex}} \dot{M} \quad (2)$$

The Solar System

A subway map

Artwork by Ulysse Carion.
Original calculations by /u/CuriousMetaphor.

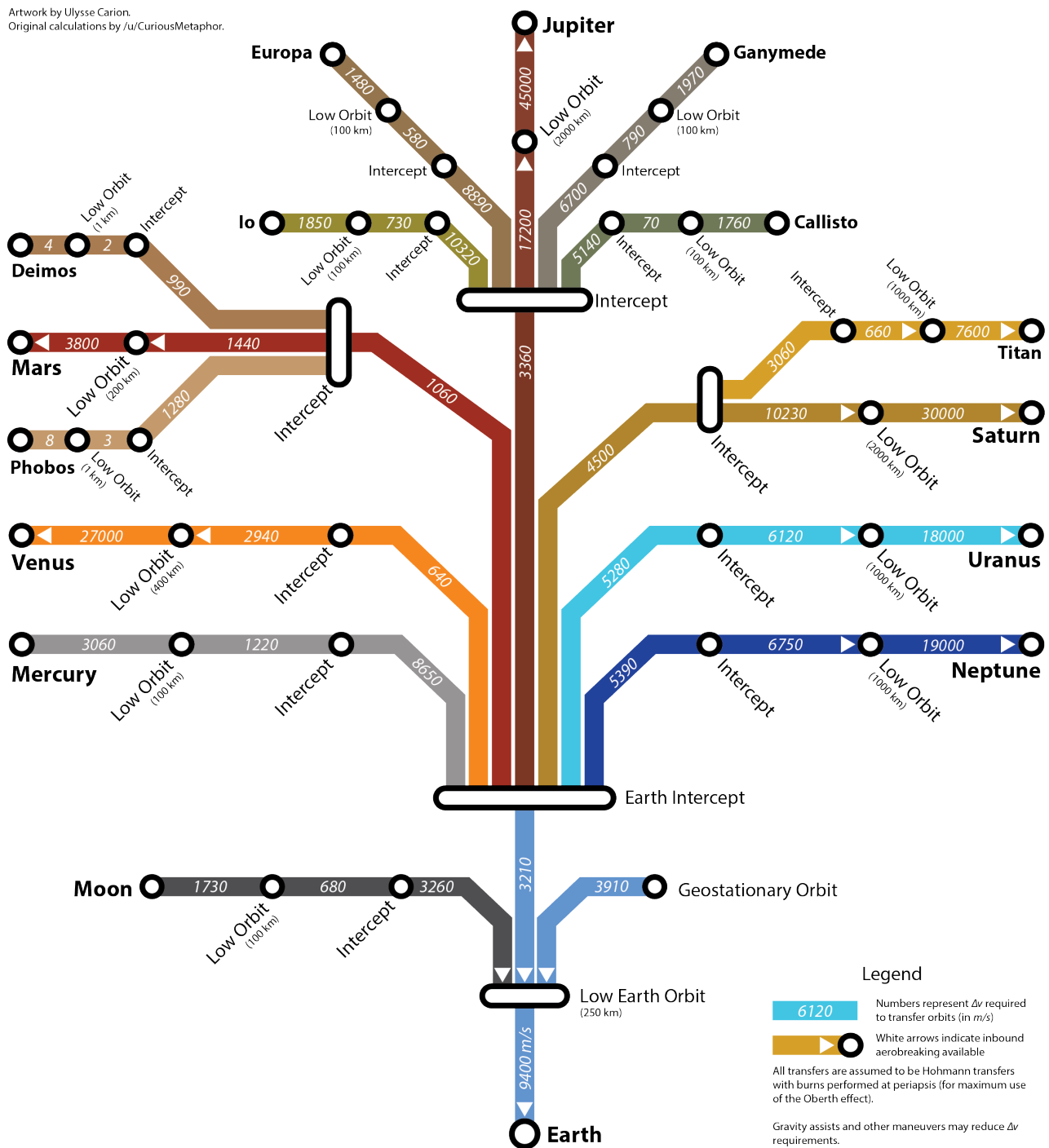


FIGURE 1 – Representation of the different Delta-V needed to go around the solar system, from u/ucarion [1]

with v_{ex} the exhaust velocity of the propellant, and \dot{M} is the propellant mass flow rate through the thruster. Hence,

$$\text{Delta-V} = \int_{t_1}^{t_2} v_{\text{ex}} \frac{|\dot{M}|}{\dot{M}(t)} dt = v_{\text{ex}} \ln \left(\frac{M_0}{M_1} \right) \quad (3)$$

with $M_0 = M(t_0)$ and $M_1 = M(t_1)$, and supposing that v_{ex} is constant. We see from Eq. (3) that for a spacecraft of dry mass M_1 to have a given Delta-V, the exhaust velocity is directly linked to the initial wet mass $M_0 = M_1 + M_{\text{prop}}$, with M_{prop} the propellant mass. Equation (3) is known as the (Tsiolkovsky) rocket equation. The exhaust velocity v_{ex} is usually referred instead by the specific impulse $I_{\text{sp}} = g_0 v_{\text{ex}}$, with g_0 the standard gravity.

Chemical space propulsion systems

The usual thruster for rocket thruster uses chemical reaction to generate the thrust. For instance, the Vulcain (the thruster engine of the main stage of the European Ariane 5 and 6, developed by ArianeGroup, ex. Safran) uses the oxygen-hydrogen combustion, the most efficient chemical reaction [2]



with the energy of 572 kJ of heat generated by 1 mol of oxygen. This means that burning 1 kg of hydrogen-oxygen mixture generates a total energy of 13 MJ.

Supposing that the entire energy is converted into the exhaust of the water produced, its velocity would be of 5.1 km/s. In reality, the exhaust velocity of the Vulcain is of 4.2 km/s, corresponding to $I_{\text{sp}} = 431$ s. The efficiency of the Vulcain is close to 80%, which is very high efficiency, and it would be difficult to increase it significantly.

The fact that the energy source is linked to the propellant mass gives an upper limit of exhaust velocity for a given combustion. Electrical propulsion engines, on the other hand, decouple the mass ejected (the propellant) from the energy source. This allows a theoretical unlimited exhaust velocity. Another advantage is the absence of reactive species, which lowers the security requirements impacting the spacecrafts.

Electric propulsion

Electric Propulsion (EP) systems mostly rely on plasma [3, 4]. They have been successfully used since the 1960s by governments, but their complexity, the limited electric power available, and the natural risk aversion of the space industry kept the EP technologies hidden from the commercial applications [5]. The breakthrough came in the '90s when the former Soviet Union's companies licensed the technology to western propulsion companies. However, many commercial satellite manufacturers were sceptical, until the first decade of the 20th century, which brought strong evidences of the competitiveness of EP. The landmark of commercial use of EP is the selling of 4 all-electric satellites for Geostationary Earth orbit by Boing in 2012, the first 2 of which launched in March 2015.

The two main EP technologies used are

- the HETs, also known as Stationary Plasma Thruster (SPT) in Russia
- the Gridded Ion Thrusters (GIT), usually referred as Ion Thrusters

Recently, the first satellites of two mega-constellations (OneWeb, 648 satellites planned, from which 6 were launched on February, the 26th 2019, and Startlink, 12 000 satellites planned, from which 62 were launched on May, 23rd 2019) were send to Low Earth orbit, both using HETs.

The Gridded Ion Thruster is a plasma chamber closed at one end by two or more grids. The plasma source can be an emitting cathode, generating energetic electrons that ionize the propellant, usually Xenon, or a Radio Frequency (RF) source. The ions are accelerated by the potential difference between the grids. Another cathode is used to neutralize the ion beam. Compared to HETs, it produces an ion beam with less divergence and an higher I_{sp} of the order of 3000 to 4000 s. Figure 2 shows a picture of the ion thruster used for the BepiColombo mission toward Mercury. We clearly see the neutralizing cathode, the accelerating grid and the ion beam.

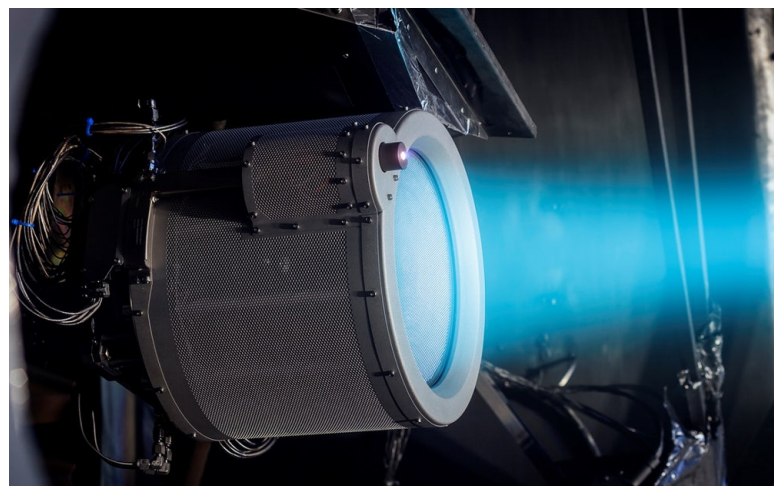


FIGURE 2 – The T6 ion thruster will help send BepiColombo to Mercury (Credit: QiniteQ)

Hall Effect thrusters uses a magnetic barrier to ~~keep the electrons on an annular trajectory~~, both increasing ~~ing~~ the ionization of the propellant and creating ~~ng~~ the accelerating electric field. A detailed description of the HET is presented in the next section. One cathode is used to start the discharge and neutralize the beam. Compared to GITs, HETs need less power ~~sources~~, hence reaching better thrust per power ratio and smaller (hence lighter) Power Processing Unit. Their typical I_{sp} is of the order of 1500 s.

Figure 3 shows a high power prototype firing. We see the emitting cathode at the center ~~and~~ and the ion beam.

EP environment in France

France is a leader country in the aerospace industry in Europe and in the world, with for example the companies Airbus, Thales, Safran and ArianeGroup. ~~Unsurprisingly~~, the French ecosystem of electric propulsion is rich. The main thrusters produced in France are the PPS series from Safran, with the PPS®1350 (version G at 1.5 kW nominal power, and the version E at 2.7 kW), and the PPS®5000, a high power HET at 5 kW, the first models of which ~~has~~ been

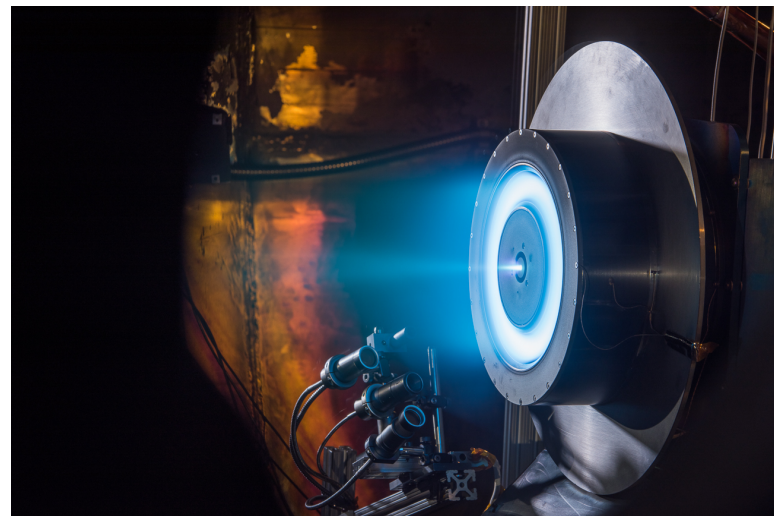


FIGURE 3 – A 13 kilowatt **HET** prototype on a testing bench in a vacuum chamber (Credit: NASA).

delivered to Boeing in May 2019. A low-power version of the PPS® is currently developed at Safran [6]. A list for the PPS® series elements and their respective characteristics can be seen in Table 1.

TABLE 1 – Members of the PPS® series developed by Safran Aircraft Engines [7, 8, 6]. The nominal operating condition of the PPS®X00 is not fixed, yet.

Name	Power	Thrust	I_{sp}
PPS®1350-G	1.5 kW	89 mN	1650 s
PPS®1350-E	2.7 kW	140 mN	1800 s
PPS®5000	3 – 5 kW	150 – 300 mN	1850 – 1700 s
PPS®X00	~ 650W	~40 mN	~ 1450 s

Several initiative concerning the small-sat sector are also undertaken, as for instance the start-ups Exotrail (micro **HET**) and Thrust Me (radio frequency Ion Thruster), or the Electron Cyclotron Resonance Thruster at ONERA.

A research group on plasma propulsion has been studying **HET** since 1996. It is composed of the Centre National d'Etude Spatial (**CNES**), laboratories as ICARE, LAPLACE and LPP, Safran and ONERA [7]. These numerous actors, combined with the support of the France and European space agencies, compose a stimulating environment that contributes both to the most mature technologies and the promising **EP** concepts that could disrupt the propulsion sector.

HET research and development with Safran



Safran Aircraft Engines has been collaborating with Laboratoire de Physique des plasmas (**LPP**) since 2014, starting with the Ph.D. thesis of Viven Croes [9]. During this first three years, a **2D** Particle in Cell (**PIC**) code has been developed simulating the radial and azimuthal directions of a **HET**. Azimuthal instabilities have been observed in Croes et al. [10], and the effects of alternative propellants have been investigated in Croes et al. [11].

From this fruitful collaboration, an ANR (Agence National de la Recherche) chair has been created. Its objective is to develop novel methods to reduce the development time and cost of the next **EP** systems. Both experiments and simulations are being developed to unlock the barriers of **HET** development. The **POSEIDON** chair is linked to the current development of a low power **HET** at Safran, the PPS®X00, which nominal operating point is of the order of 500W. The scientific part of the chair is leaded by **LPP**, while an unstructured 3 dimensions (**3D**) simulation code is developed by the CERFACS, in Toulouse. Safran leads the engineering development and experimental investigation.

At the begining of my thesis, I participated to the development of a Laboratory Model (**ML**) of the PPS®X00. The objectives of the PPS®X00-**ML** is to represent the physics of the PPS®X00 while allowing parametric study of the main parameters of a **HET**, as the geometry, the magnetic field topology, or the wall material. The PPS®X00-**ML** has successfully showed its usefulness, as the first tests allow to obtain state of the art performances [6]. My work at Safran showed us that the development of **HET** are currently driven by experiments, because numerical tools are not yet predictive. Simulations are helpful for the engineers to have some insights for the thruster behaviour, but cannot be used for development with confidence. However, experiments are costly and time-consuming. They also are prone to delays in the conception schedule, and reduce innovation as designers take less risks.



The lack of numerical tools for **HET** comes from some keys physical phenomena ill-understood.

Key phenomena of **HETs**

Even though **HET** have been studied and used for more than 40 years, some keep phenomena are still ill-understood, making the development of **HET** by manufacturers a *trial and error method*. These key phenomena are

- the electron transport toward the anode
- the plasma-surface interaction
- the wall erosion
- the propellant nature

The electron axial transport through the magnetic barrier has been measured much higher than the expected value from the classical collisional theory by Meezan et al. [12]. Different phenomena have been proposed to explain the origin of this *anomalous* transport. Two phenomena are supposed mainly responsible for this mobility: the azimuthal instability and the near wall mobility due to electron emission. A significant part of the work of the thesis concerns the quantitative comparison of the relative influence of the two phenomena.



Plasma-wall interaction concerns the phenomena that depends of the wall material and affect the discharge. Indeed, depending ~~the~~ the nature of the wall, the discharge behaviour can vary [13]. The phenomena responsible for this observation is the electron emission, as an electron reaching the wall will have a different probability to emit one or more electrons for different material. This affect the particle and power balance of the plasma, hence affecting the sheath and plasma characteristics. Ion induced electron emission is much less likely to happen as the ions have a small energy of impact.

Wall erosion is due to sputtering of the ceramic induced by ions impact. This large erosion is the main limitation of HETs lifetime. While most aspects of the erosion are well understood, we observe the apparition or pattern the eroded surfaces that could affect the performances. The origin, and implication, of these erosion striations stays an open question.

The propellant nature affects the chemistry of the plasma in the thruster. Because of its high mass and low ionization energy, xenon has been used since the beginning of HET. However, it is very costly. The cheaper, but less effective, propellant of choice is krypton, that started to be used. Iodine could also be interesting, as it can be stored at room temperature in a solid state. The impact of the propellant mass and chemistry is not yet clear, and slows down the use of alternative propellants.

The objectives of my thesis, in the context of the POSEIDON chair focuses on the **two** first point – the plasma wall interaction and the electron mobility – and how they can influence each-other.

Plasma models and simulations

The plasma is the state of matter ~~were~~ where the internal energy is high enough to ionize the atoms. Depending ~~of~~ the pressure, energy, and time scale, different models are better to describe the plasma. There are mainly two distinct models. The first is the *kinetic* description of the species of the plasma, via the Boltzmann equation. The second uses a *fluid* description of the species, by means of moments.

Boltzmann equation

The Boltzmann equation in Eq. (4) describes the evolution of the particles (atoms, ions and electrons) in the phase space. The phase space is the set of all ~~possible~~ position \mathbf{x} and velocity \mathbf{v} that can be attained by a particle. The evolutions in the phase space are due to forces, diffusion and collisions.

$$\frac{\partial f}{\partial t} + \mathbf{v} \cdot \nabla_{\mathbf{x}} f + \mathbf{F} \cdot \nabla_{\mathbf{v}} f = \frac{\partial f}{\partial t} \Big|_{\text{coll}} \quad (4)$$

where f is the distribution function of the particle at \mathbf{x}, \mathbf{v} , and $\frac{\partial f}{\partial t} \Big|_{\text{coll}}$ denotes the effects of the collisions, ∇ is the gradient in both the positions (subscript \mathbf{x}) and the velocities (subscript \mathbf{v}) and \mathbf{F} is the force applied to the particle. In the general electro-magnetic case,

$$\mathbf{F} = q\mathbf{E} + q\mathbf{v} \times \mathbf{B}$$

with q the particle charge, \mathbf{E} the electric field, and \mathbf{B} the magnetic field.

Fluid equations

The description in 7 dimensions (3 of space, 3 of velocity, and one of time) can complicate the resolution of the Boltzmann equation. If the precise description of f is not needed, we can instead use the first moments of Equation (4) on the velocity.

The first equation is obtained by integrating Eq. (4) over the velocity space ~~gives~~

$$\begin{aligned} \iiint_{\mathbf{v}} \frac{\partial f}{\partial t} d^3 v + \iiint_{\mathbf{v}} \mathbf{v} \cdot \nabla_{\mathbf{x}} f d^3 v + \iiint_{\mathbf{v}} \mathbf{F} \cdot \nabla_{\mathbf{v}} f d^3 v &= \iiint_{\mathbf{v}} \frac{\partial f}{\partial t} \Big|_{\text{coll}} \\ \Leftrightarrow \frac{\partial n}{\partial t} + \nabla_{\mathbf{x}} \cdot (\mathbf{u} n) + 0 &= S_{iz} \end{aligned} \quad (5)$$

where $n = \iiint f d^3 v$ is the density, $\mathbf{u} = \frac{1}{n} \iiint \mathbf{v} f d^3 v$ is the mean velocity, and S_{iz} is the source term of particle due to ionization. Equation (5) is the continuity equation for a given species.

In the similar fashion, integrating the Boltzmann equation times the velocity or the kinetic energy gives the momentum conservation equation and the energy conservation equation. This set of equation is simpler to approach, although it relies on more hypotheses. One of them being the closure of the system. Indeed, the continuity equation describes the evolution of the density n but needs the mean velocity \mathbf{u} . However, the velocity is described by the momentum conservation equation that need the temperature T , and so on.

In order to close the system, one has to make a hypotheses on the higher moment of the distribution function. A usual closure is the isothermal hypotheses, that fix the temperature. Hence, the energy conservation equation is not needed. Other closures ~~possibles~~ are the adiabatic hypotheses (no heat flux, the 3rd moment of f), the polytropic law linking the evolution of n with T , or the Fourier law for heat diffusion.

Should we write the closes as equations ? $q = 0$, $T_e n_e^a = cst$, etc. ?

<



Plasma simulation models

As there are two different models to describe the plasma, there are two different simulation methods : the fluid simulations and the kinetic simulations.

The fluid simulations solve the moments of the distribution function (the density, mean velocity and usually the temperature of the species), and the electromagnetic fields. Depending of the conditions, the system of equation can be simplified before resolution. In electrodynamic conditions, mainly for space plasmas and fusion, the Maxwell equations are coupled to the fluid equations leading to magnetohydrodynamics (MHD). In the case of electrostatic conditions, as it is usual for Low Temperature plasmas, the Poisson equation is coupled to the fluid equations. Due to the low mass of the electrons compare to the ions, we can also suppose the quasi-neutrality of the plasma, leading to the drift-diffusion approximation. The fluid equations can be solved in 3D, 2D or 1 dimension (1D) for space. In low dimension model, the effects of the missing dimensions is usually added, for instance in the source terms as done by Barral et al. [14].

However, some phenomena can only be described via the distribution function. An example of such phenomena is the particle-wave interaction, as the Landau Damping [15, 16] or the

plasma-beam instability [17], for which the gradient of the distribution function in the velocity space is important. In contrast to the fluid descriptions, *kinetic* simulations solve for the distribution function for both position and velocities. Two approaches are usually used for kinetic simulations:

- The Direct Kinetic (**DK**) simulations, that discretize Equation (4) in the full phase space.
- The **PIC**, that uses an ensemble of particles to discretize the distribution function.

While the **DK** simulations use an Eulerian description of the distribution function, we can see the **PIC** simulations as a Lagrangian approach. The **DK** simulations can theoretically better describe the plasma, mostly because there is less numerical noise and we can model binary collision more easily, especially Coulomb collisions. On the other hand, **PIC** simulations are much more simpler to develop on both a mathematical and a computation perspective. For instance, the kinetic effect of electron emission have been recently studied using **DK** simulation by Cagas et al. [18], while it has been done since the last century in **PIC** simulations [19].

Problematic

We have seen in the previous sections that the **HETs** have been studied and used since several decades. However, several challenges are currently tackled in the **EP** industry, as the most prominent listed by Samukawa et al. [20] :

1. Performance improvement: efficiency, lifetime and cost-effectiveness. Lifetime is an important issue and is limited by electrode or wall erosion. Lifetime of an electric thruster must be larger than 10 000 h of (reliable) operation.
2. Design of more versatile thrusters, i.e. able to operate at different combinations of thrust/propellant velocity.
3. Extension of domain of operation to lower power (μN to 10 mN thrust range) for microsatellites or very precise attitude control.
4. Extension to higher power for orbit raising of telecommunication satellites (several tens of kW) and interplanetary missions (100 kW and more).
5. Extension of EP to low-altitude spacecraft: there is an increasing interest in civil and military spacecraft flying at altitudes around 100 km where the drag is significant and must be constantly compensated.

The **HET** technology has the potential to answer many of these challenges. for instance, the lifetime is approached with wall-less and magnetically fielded configuration. Versatility is tackled with dual-mode **HET** configuration [7], low power thruster is attained with μ -thrusters [21], and so forth.

Unfortunately, the ~~developed~~ of **HETs** remains principally empirical. Two physical phenomena are still unclear, and block the understanding of **HETs** [20, 22]:

- the electron transport,
- the plasma-wall interaction.

In parallel to sophisticated diagnostics, efforts in the development of kinetic simulations is pursued. Indeed, the electron transport is affected by instabilities that can only be described by kinetic models [23, 24]. In addition, the plasma-wall interaction is also affected by kinetic

effects, both concerning the electron emission induced by electron impact [14, 25, 26] and the wall erosion by ion impact sputtering.

Relatively few simulation codes highly parallelized have been developed, that could allow parametric studies. But the ever increasing computational power available allows bigger simulations to be conducted, with for instance 3D simulation recently performed [27, 28], even if a scaling still was needed to obtain the results under a reasonable time.

The objective of the work performed during this thesis was to better understand the inner physics of the HET discharge, more precisely the electron transport and the plasma-wall interaction. In order to answer this question, a kinetic simulation code, highly parallelized, is developed and used, and order to pin-down the main mechanisms, and propose macroscopic  model by the mean of parametric studies.

In Chapter 1, we introduce the simulation model. Chapter 2 presents the results of a parametric study investigating the wall effect PIC. In chapter 3, we revisit the sheath model in order to explain the simulation results. The content of Chapter 4 and 5 are not yet fixed. 



Chapitre 1



Particle-In-Cell simulations of HETs

Is missing an overview all of the HET physics. Like the Boeuf Tutorial. Should I add one ?



The **HET** has been studied since its first designs in the 1960's. However, the physical processes that govern its behaviour stay ill-understood. For most of them, as the electron cross field mobility or the plasma-surface interactions, kinetic informations are needed. This first chapter presents the basics of the **PIC** - Monte Carlo Collision (**MCC**) simulations, and the simulations code **LPPIC** that is developed at **LPP**. Then is described the simulation model, focussing of the wall and the convection models.

Contents

1.1	The Hall effect Thruster	12
1.1.1	Operating principle	14
1.1.2	Electron drift and azimuthal instability	15
1.1.3	Plasma-wall interaction	15
1.1.4	Cross field transport of the electrons	16
1.1.5	Three-dimensional physics	16
1.2	Elements of the 2D PIC-MCC simulations	17
1.2.1	Principle of the PIC simulations	17
1.2.2	Monte Carlo collisions	17
1.3	Numerical implementation of the Particle in cell simulation	17
1.3.1	Data used	19
1.3.2	Particle pusher	20
1.3.3	Poisson equation solver	21
1.4	Bidimentional simulation of an HET	21
1.4.1	Neglecting curvature	21
1.4.2	Radial-azimuthal domain description	21
1.4.3	Particle balance	22
1.4.4	Axial convection	22
1.5	Dielectrics boundary condition	23
1.5.1	Non-uniform mesh	23
1.5.2	Poisson equation discretization	24
1.5.3	Poisson equation discretization	25
1.5.4	Including surfaces charges	26

1.5.5	Verifications	27
1.5.6	Interface at the cell centre	27
1.5.7	Surface charges for centred interface	29
1.6	Axial Convection model	29
1.6.1	Lafleur's model of convection	29
1.6.2	Numerical artefacts	31
1.6.3	Numerical noise of Lafleur's convection model	33
1.6.4	Effect of the noise on the electric field	34
1.6.5	Noiseless convection model	35
1.6.6	Effects on a 2D simulation domain	37
1.7	Secondary electron emission	38
1.7.1	Models of emission	39
1.7.2	Electron emission model used	39
1.8	Electron cross-field transport	40
1.9	Sheath model with electron emission	42
1.10	Conclusion	43

1.1 The Hall effect Thruster



The **HET** is an electrostatic electrical propulsion system accelerating ions by the mean of an imposed voltage difference. Figure 1.1 shows a picture of an **HET** switchon and off. We can clearly see the plasma in the annular chamber.



FIGURE 1.1 – Front view off an **HET**, the BHT-1500 from Busek, USA

We can summarize the composition of an **HET** with four parts:

1. The annular chamber.

2. The injecting anode
3. The cathode
4. The magnetic circuit

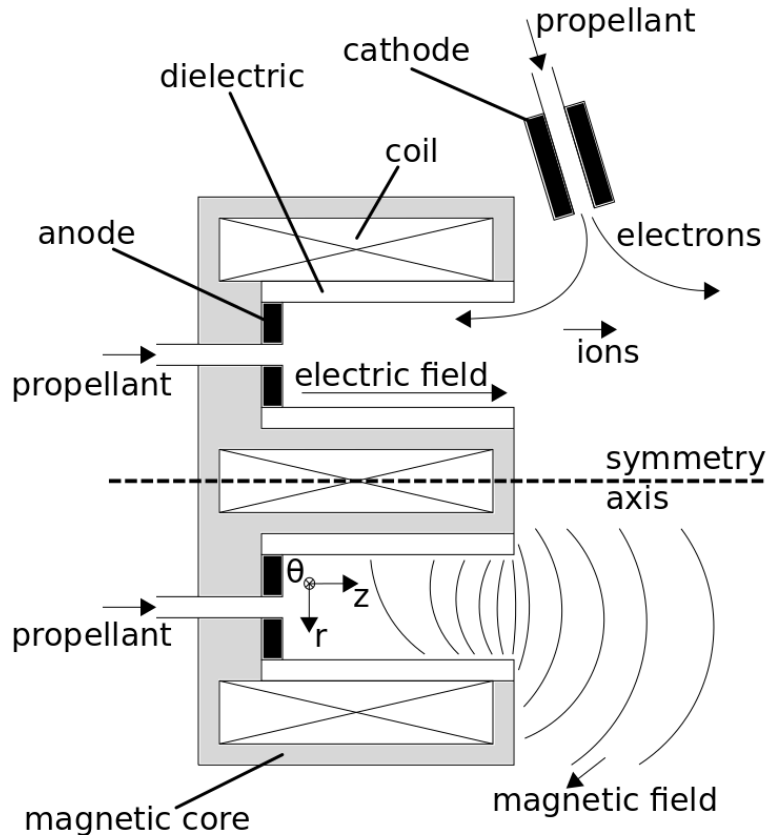


FIGURE 1.2 – Schematic cut of an HET, illustrating its different parts.

Figure 1.2 presents a schematic cut of the HET along its axial and radial direction.

The chamber has an annular shape. It is closed at the anode side, and kept open at the other side. The axial length of the chamber is between 1 and 3 cm, the radial width of the chamber is between 1 and 2 cm. The walls are usually constituted by a ceramic, as the Boron Nitride-Silicon Dioxide (**BNSiO₂**). The material needs to be resistant to erosion by ion impact sputtering. But changing the material is also known to affect the discharge behaviour. The usually supposed phenomena for this impact is the secondary electron emission yield that is a function of the material nature.

The anode is at the bottom of the chamber. The anode voltage is imposed to a few hundred volts. Usually, the neutral gas injection is made by the anode itself, or it is close to the anode. The mass flow rate is of the order of a few mg/s.

The cathode is outside of the chamber. It is grounded, and injects electrons for two reasons:

- most of the electrons ($\sim 90\%$) are used to neutralize the ion flux, for both allowing the ions to leave the thruster and avoid charging of the spacecraft.

- some of the electrons are attracted by the anode, hence entering the chamber and allowing the plasma discharge to switch and remain on.

The magnetic circuit is composed of electromagnets and a magnetic circuit made of different ferromagnetic pieces. It creates a constant radial magnetic field in the annular chamber. The maximum value of the radial magnetic field is located close to the exit plan of the chamber. Its amplitude is on the order of 200 Gauss (2×10^{-2} T).

Figure 1.3 illustrates the axial profile of the amplitude of the radial magnetic field.

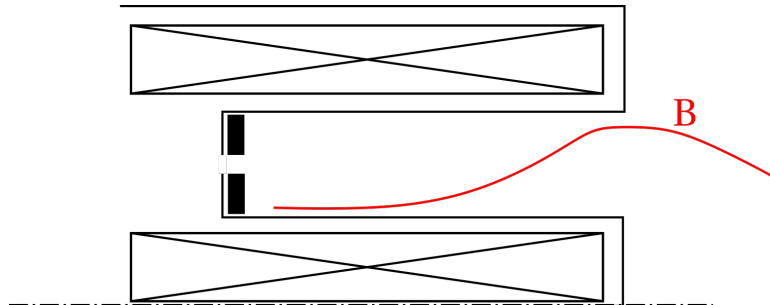


FIGURE 1.3 – Usual shape of the axial profile of the radial magnetic field on the centreline of the channel.

1.1.1 Operating principle

The operation principle of an **HET** is rather simple. The objective is to ionize the propellant and impose an electric field to accelerate the ions.

Ionization Due to the low pressure (around 1×10^{-4} Pa), the mean free path of the electrons is larger than the chamber size. In consequence, we impose the magnetic field in order to trap the electrons in a cyclotron motion, increasing the residence time of the electron, and the ionization. In average, 90% of the propellant is ionized in a well designed **HET**.

Acceleration The potential difference between the anode and the cathode is used to accelerate the ions outside of the chamber and create the thrust. Because the magnetic field slows the electrons down, the plasma resistivity increases in the region where the magnetic field amplitude is large. Hence, the axial profile of the amplitude of the axial electric field presents a maximum close to the maximum of the magnetic field.

Ionization and Acceleration regions overlay As both the ionization region and the acceleration region are governed by the magnetic field, it can be difficult to obtain a net separation. However, if ionization appears in the acceleration region, the newly created ions will not be accelerated at their maximum velocity, hence resulting in a loss compared to the maximum theoretical thrust.

Figure 1.4 shows an illustration of the amplitude of the ionization and the acceleration due to the electric field.

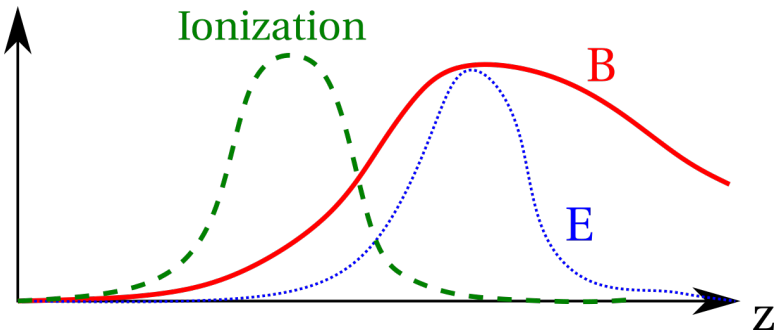


FIGURE 1.4 – Illustration of the usual axial profiles of the ionization and acceleration amplitude compared to the magnetic field.

The thruster efficiency, in the usual configuration, is governed by its magnetic field topology. Hence, it can be difficult to find the best topology that will optimize the ionization and the location of the regions.

Some concepts of double stage HET have been proposed to decouple the two phenomena in order to control them independently. However, the preliminary results are not as satisfactory as expected. Moreover, the double-stage system needs more parts and power sources, resulting in a more complicated system.

1.1.2 Electron drift and azimuthal instability

The axial electric field E and the radial magnetic field B induces an azimuthal $E \times B$ drift of the electron Because their large mass, the ions are not significantly affected by the magnetic field, hence they do not drift .

As a consequence, there is a strong drift of the electron in respect to the ions. This drift can lead to instability in the azimuthal directions. Because the drift is perpendicular to the magnetic field, it is usually called Electron cyclotron drift instability (**ECDI**). However, as it rises from an $E \times B$ drift, some authors uses the name $E \times B$ electron drift instability (**EDI**) .

Azimuthal oscillations have been observed both experimentally and in simulations. However as the **ECDI** characteristic are very close to usual Ion Acoustic Wave (**IAW**), the community is still arguing about the actual kind of wave observed. A part of the work conducted during my theses concerns the study and characterization of the instabilities observed in the simulations .

1.1.3 Plasma-wall interaction

The ceramic wall closes the chamber in the radial directions. As usually observed in bounded plasmas, a floating plasma sheath forms between the plasma and the dielectric wall. The sheath confines the electrons in the plasma and accelerates the ions toward the walls. This allows to obtain a flux of electron equals to the flux of ion , resulting in a charge conservation in the plasma, and a neutral flux, also named zero-net current to the surfaces.

Due to the relatively high electron energy, the material can emit electrons induced by electron impact. These secondary electrons are accelerated toward the plasma, and so modify the plasma and the sheath properties. The probability of Secondary Electron Emission (**SEE**)

depends of the electron impact characteristics (energy, angle) but also of the material: some material are more emitting than others 

1.1.4 Cross field transport of the electrons

The electrons are not only drifting in the azimuthal directions. For instance, because of collisions, the electrons can move from one magnetic line to another. This leads to a cross-field transport in the direction of the electric field. Indeed, considering the electron momentum conservation equation [24]

$$\partial_t(m_e n_e \mathbf{v}_{de}) + \nabla \cdot (m_e n_e \mathbf{v}_{de} \mathbf{v}_{de}) = q_e n_e (\mathbf{E} + \mathbf{v}_{de} \times \mathbf{B}) - \nabla \cdot \boldsymbol{\Pi}_e - m_e \nu_m n_e \mathbf{v}_{de}, \quad (1.1)$$

where m_e , q_e , n_e , \mathbf{v}_{de} and $\boldsymbol{\Pi}_e$ are the electron mass, charge, density, drift velocity and pressure tensor, and ν_m is the electron-neutral momentum transfer collision frequency. Ignoring the electron inertia and the pressure term, and with $\mathbf{B} = B_0 \mathbf{e}_r$, we can write the balance equation projected on the axial and azimuthal direction

$$\begin{cases} 0 = n_e E_z - n_e v_{de\theta} B_0 - \frac{m_e}{q_e} \nu_m n_e v_{dez} \\ 0 = n_e E_\theta - n_e v_{dez} B_0 - \frac{m_e}{q_e} \nu_m n_e v_{de\theta} \end{cases} \quad (1.2)$$

Supposing no electric field in the azimuthal direction ($E_\theta = 0$), we can combine the two equations of Eq. (1.2) and have [29, 12]

$$\mu_{\text{classical}} = \frac{n_e v_{dez}}{n_e E_z} = \frac{\frac{|q|}{m \nu_m}}{1 + \frac{\omega_{ce}^2}{\nu_m}} \quad (1.3)$$

with $\omega_{ce} = \frac{|q| B_0}{m}$ the cyclotron frequency. However, it has been observed in **HET** that the electron cross-field transport is higher than $\mu_{\text{classical}}$ only due to collisions. Recently, the **ECDI** has been proposed to induce this so-called anomalous transport of the electrons.

Another phenomena that can leads to increased cross-field transport in the Near-Wall Conductivity (**NWC**). It is due to electron collisions with the wall, inducing **SEE**. 

1.1.5 Three-dimensional physics



The physics of the **HET** is really three dimensional:

- The plasma is accelerated in the axial direction. The axial profile of the magnetic field is responsible for the performance of the thruster.
- The radial dimension is closed by the chamber walls. The walls are responsible for most of the plasma losses, both on the particle and energy balances.
- The electrons drifts in the azimuthal direction, leading to instabilities.

Consequently, when simulating an **HET**, if one of the direction is not model, a part of the physics will be missing:

- **Missing** axial direction: the ionization or the acceleration and the **convection** are missing
- **Missing** radial direction: the wall losses and interactions are missing
- **Missing** azimuthal direction: the **ECDI** is missing, hence the electron cross-field transport is not well represented.

While 3D-simulations have recently been proposed, they uses scaling laws to simulate the system in a reasonable amount of time. A 3D simulation at scale 1:1 is not yet accessible. Hence, we need to rely on 1D or 2D simulations. Consequently, we need to take into account the missing physics or include a model of its effects on the system.

1.2 Elements of the 2D PIC-MCC simulations

1.2.1 Principle of the PIC simulations

The PIC simulation models particles moving freely on a grid. The grid is used to compute the electric field, in the electrostatic approximation by solving the Poisson equation

$$\Delta\phi = -\frac{\rho}{\epsilon_0} \quad (1.4)$$

where ϕ is the electric potential, ρ is the charge density, and ϵ_0 the vacuum permittivity. If the electrostatic approximation is not correct, one need to solve the Maxwell equations.

The particles move following the Lorenz forces

$$m\mathbf{a} = q\mathbf{E} + q\mathbf{v} \times \mathbf{B} \quad (1.5)$$

with m and q the particle mass and electric charge respectively. The numerical particles followed in the simulations correspond to q_f physical particles, with

$$q_f = \frac{nV}{N_{pc}} \quad (1.6)$$

with n the particle density, V the volume of a cell, and N_{pc} the number of numerical particle in a cell. A large enough number of particle is needed in order to obtain physical results. Indeed, insufficient number of particles leads to numerical heating [30]. Usually, a minimum of 100 particles per cell are used, but recent results seem to encourage to use more particle [31].

1.2.2 Monte Carlo collisions

In PIC simulations, collisions between charged and neutral particles can be modeled by binary collision, but this approach is computationally costly. Instead, a Monte-Carlo algorithm can be used [32]. This approach is very efficient, and allow scattering, momentum transfer and ionization to be consistently modeled. The propellant used in HET usually is Xenon (Xe), even if the recent constellation Starlink uses Krypton (Kr). The cross sections used for modeling Xe or other gases collisions are taken from the LXCAT database project [33]. Except if otherwise stated, the elastic, inelastic scattering and ionization reactions listed in Table 1.1 are used. The cross section values are summarised in Fig. 1.5.

1.3 Numerical implementation of the Particle in cell simulation

LPPIC is an explicit electrostatic PIC-MCC simulation code. Every time-steps, the simulation loop presented in Fig. 1.6 is computed. The different steps constituting the PIC-loop

TABLE 1.1 – Reactions for xenon used in the PIC simulations

Reaction	Threshold	Reference
<i>Elastic scattering</i>		
$e + Xe = e + Xe$	–	[34, 35]
<i>Excitation</i>		
$e + Xe = e + Xe^*$	8.315eV	[34, 35]
$e + Xe = e + Xe^*$	9.447eV	[34, 35]
$e + Xe = e + Xe^*$	9.917eV	[34, 35]
$e + Xe = e + Xe^*$	11.7eV	[34, 35]
<i>Ionization</i>		
$e + Xe = e + Xe^+$	8.315eV	[34, 35]

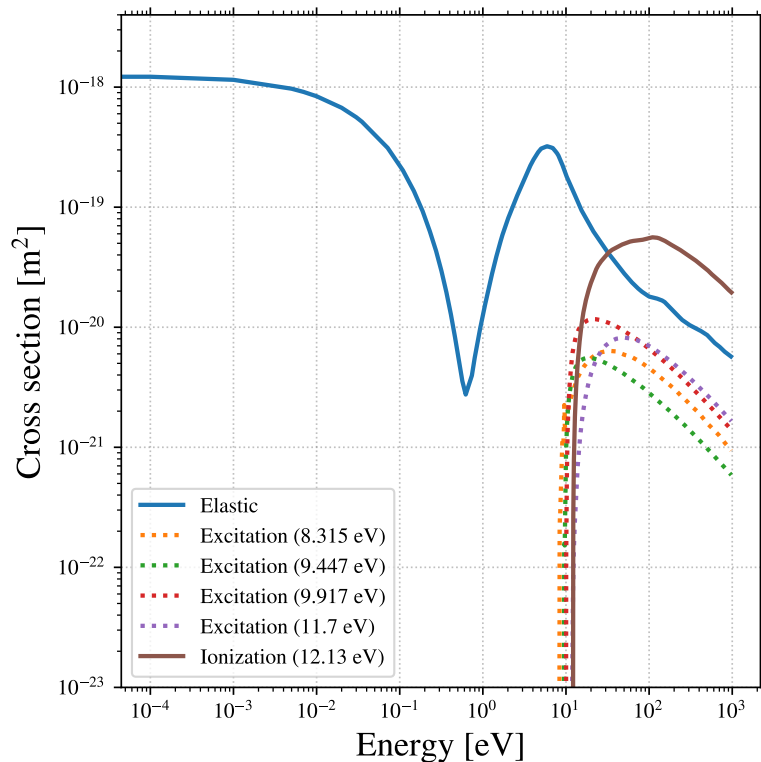


FIGURE 1.5 – Cross section values used in the Monte Carlo procedure [34, 35].

are described in the next subsections.

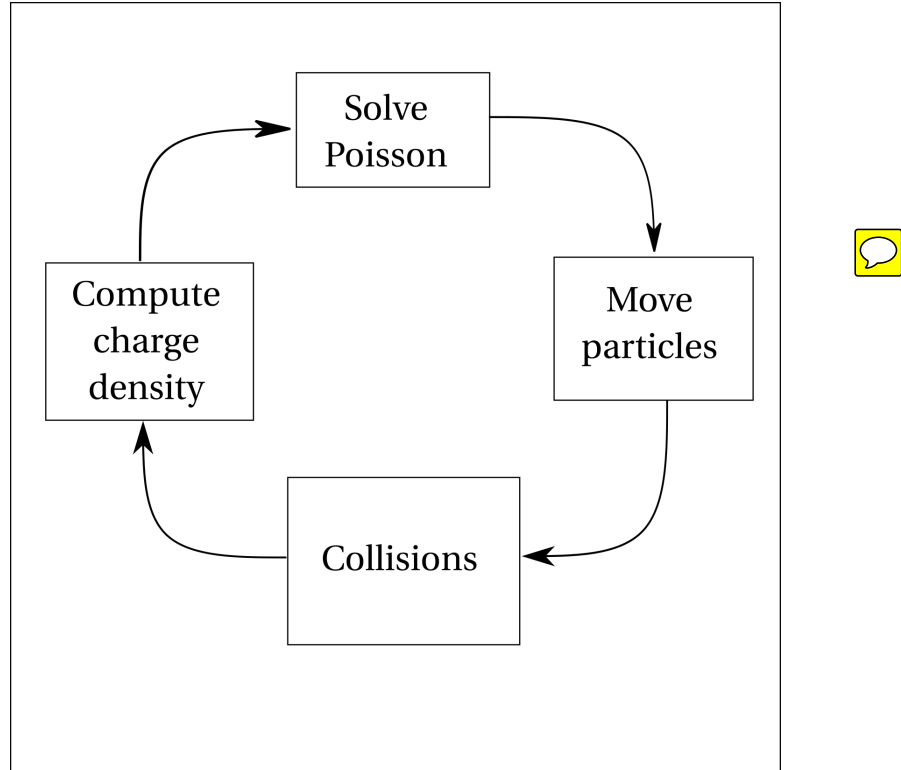


FIGURE 1.6 – **PIC-MCC** loop executed every time steps.

1.3.1 Data used

In **PIC** simulations, there are two kind of data used:

- Particles (electron, ions, neutral) can be followed as well but not in LPPIC)
- Mesh, also named fields (densities, electric and magnetic fields, and so on)

Particles

For each particles, are known its position \mathbf{x} and its velocity \mathbf{v} . In most **PIC-MCC** simulations, the 3 directions of the velocity vector are followed in order to ~~in order to~~ take into account scattering. It is abbreviated as **3V**.

Fields

The fields are defined at the center of each cell of the mesh. The charge density ρ is computed by depositing the particle on the mesh, using the Cloud-in-cell model [36]. The electric field at the position of the particle is also obtained by bi-linear interpolation. The mesh dimension defines the dimension of the simulation. It is usual to find **1D3V** or **2D3V PIC** simulations, for particles with 3 directions on the velocity but 1 (or 2) dimensions in space.

1.3.2 Particle pusher

The interaction of the movement equation Eq. (1.5) is different for magnetized and non-magnetized particles.

For non-magnetized particles, we use the leapfrog scheme [36]

$$\mathbf{v}^t = \mathbf{v}^{t-1} + \frac{q}{m} \mathbf{E} \Delta t, \quad (1.7)$$

$$\mathbf{x}^t = \mathbf{x}^{t-1} + \mathbf{v}^t \Delta t, \quad (1.8)$$

with the superscript t designing the time step, q and m the particle electric charge and mass, \mathbf{E} the electric field at the particle position, and Δt the time step duration.

It is important to note that the leapfrog induces a shift of $\frac{\Delta t}{2}$ between the position and the velocity, as illustrated in Fig. 1.7. This shift can lead to erroneous diagnostics when computing

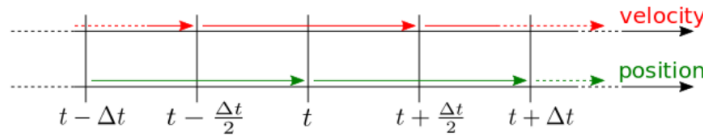


FIGURE 1.7 – Illustration of the shift between the particle velocity and position.

moments of the particles distribution. For instance, the mean velocity of an ensemble of N particles at the instant t is computed as:

$$\bar{\mathbf{v}}^t = \frac{1}{N} \sum_i^N \left(\mathbf{v}_i^t + \frac{q}{m} \mathbf{E}_i \frac{\Delta t}{2} \right). \quad (1.9)$$

Other moments like the mean energy or heat flux follow the same correction. We can see that the error between $\bar{\mathbf{v}}$ defined above and

$$\tilde{\mathbf{v}} = \frac{1}{N} \sum_i^N \mathbf{v}_i^t$$

is

$$\bar{\mathbf{v}} - \tilde{\mathbf{v}} = \frac{q \Delta t}{2m} \frac{1}{N} \sum_i^N \mathbf{E}_i.$$

Hence, the error in the diagnostic is larger in the region of large electric field (as in the sheaths).

Magnetized particles For magnetized particles, we use a modification of the leapfrog algorithm proposed by Boris [37]. It corresponds to an operator splitting between the electrostatic acceleration and the magnetic rotation. This splitting is described below:

1. accelerate the particle during $\frac{\Delta t}{2}$: $\mathbf{v}^{t-\frac{\Delta t}{2}} = \mathbf{v}^{t-1} + \frac{q}{m} \mathbf{E} \frac{\Delta t}{2}$
2. rotate the particle velocity with the magnetic field
3. accelerate the particle during $\frac{\Delta t}{2}$: $\mathbf{v}^t = \mathbf{v}^{t-\frac{\Delta t}{2}} + \frac{q}{m} \mathbf{E} \frac{\Delta t}{2}$

1.3.3 Poisson equation solver

The Poisson equation Eq. (1.4) is an elliptic equation. We can directly discretize the differential operator by finite volume on the cell mesh. The formal discretization is developed in Section 1.5, but a short summary is given here.

In 1D, the obtained linear system is tridiagonal. It can be solved directly using THOMAS algorithm, which simply stores the Gauss elimination's coefficient. In 2D, the linear system is pentadiagonal. A direct solver, like the *LU* decomposition, would require a large amount of memory to store the factorisation matrices. On the other hand, as the time step is usually small in PIC simulation, we expect the plasma potential ϕ not to change rapidly. Hence, an iterative solver using the previous solution as initial guess seems more reasonable from both the memory storage and the computational time.

In practice, we use HYPRE's multigrid solver to solve Poisson equation in 2D in LPPIC.

1.4 Bidimensional simulation of an HET

We are interested in studying the azimuthal instabilities and the induced electron transport in the axial direction. In addition, we want to study the plasma-wall interactions.

As realistic 3D simulations are not yet achievable, we choose to simulate the radial-azimuthal plan. The axial location where the electron drift is the highest is close to the exit plan, where the axial electric field is the highest. Hence, we choose this location to be simulated.

1.4.1 Neglecting curvature

The ECDI features oscillations of short wavelength of the order of the mm. Hence, neglecting the curvature of the channel is expected not to change the ECDI characteristics while improving the simulation performances.

In Héron and Adam [38], the authors have performed an 2D simulation including the channel curvature. They have observed a small difference between the inner and the outer walls. In Domínguez-Vázquez et al. [39], the authors studied the effect of the curvature using a 1D radial model. They have shown asymmetries due to the combination of the geometric expansion, the magnetic mirror effect and the centrifugal force. However, the global behaviour of the discharge is not affected compared to simulations without the curvature model. Hence, we choose to neglect the curvature.

Consequently, we can use a Cartesian mesh (also called a rectangular mesh). For the sake of clarity, the usual notation x, y is used in the simulation for the radial (r) and azimuthal directions θ , respectively.

1.4.2 Radial-azimuthal domain description

The azimuthal directions is closed using periodic boundary condition for both the particles and the fields. The radial boundary conditions can be of different kind. They are described in Section 1.5.

A constant and uniform magnetic field B_0 is imposed in the radial direction. A constant and uniform axial electric field E_0 is imposed. Figure 1.8 shows a schematic representation of the simulated domain, overlaid with the computed azimuthal electric field E_y .

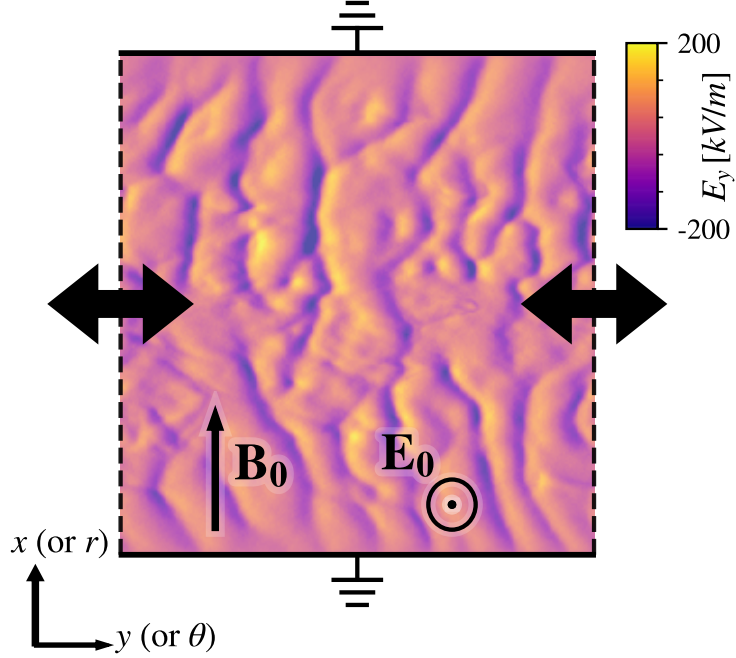


FIGURE 1.8 – Schematic representation of the radial-azimuthal simulation domain. Overlaid is the computed azimuthal electric field given as an example.

1.4.3 Particle balance

As the axial position simulated is the exit plane, the ionization is too low to balance the particle losses to the wall. Instead, the ionization takes place upstream, and the particles are convected downstream. In these conditions, two models can be used,

- having a simulation that dies off, as done in Janhunen et al. [31],
- forcing an arbitrary ionization to occur in order to compensate the radial losses [39].

The second option is slightly less realistic, but allows to obtain a steady state and is supposed not to affect significantly the simulation.

1.4.4 Axial convection

Due to the imposed axial electric field, ions and electrons gain energy. In the HET, the axial convection of the particles balances the energy gain. However, in purely 2D simulations, the convection is missing, resulting in an ever rising particle energy. This prevents the possibility to reach a steady state regime, as observed in Héron and Adam [38], Janhunen et al. [31].

We implement a model of convection initially proposed for a 1D simulation by Lafleur et al. [24], and adapted in 2D by Croes et al. [10]. The model uses a finite axial length L_z . When a particle reaches the boundary $z = 0$ or $z = L_z$, it is removed from the simulation. In order to

conserve the particle (and charge) balance, a particle is created at $z = 0$ for the ions (that are accelerated toward $z > 0$) or at $z = L_z$ for the electrons.

It has been observed that using a radial position chosen uniformly at random for the newly injected particle would affect the sheath [10]. Hence, the radial position of the new particle is the same of the removed particle.

Concerning the azimuthal particle position, it is more difficult to choose between a random position or the same position as the removed particle. In Lafleur et al. [24], Croes et al. [10], ~~the author chooses to use a random azimuthal position~~. However, ~~as we show it in Section 1.6~~, this induces a numerical noise that can be harmful in some cases.

1.5 Dielectrics boundary condition

Figure 1.8 ~~on the facing page~~ showed the simulation of the radial-azimuthal domain without dielectric wall, but instead grounded electron. Figure 1.9 illustrate the configuration in the radial-azimuthal plan highlighting the more realistic radial boundary conditions. The plasma is bounded in the radial direction by dielectric layers isolating the magnetic circuit. The magnetic circuit can be considered electrically grounded.

The particles are absorbed when touching the dielectric wall, and we suppose an infinite residence time. Hence, we obtain a surface charge σ at a time t with

$$\sigma(t) = e \int_0^t (J_i - J_e) dt \quad (1.10)$$

with J_i and J_e the ion and electron flux respectively and e is the elementary charge and supposing that there is no surface charge at the interface at the beginning.

A common approach is to suppose that the electric field inside the dielectric is zero  Using Gauss theorem, we obtain a Neumann boundary condition at the plasma-wall interface for the potential

$$|\partial_r \phi| = \frac{|\sigma|}{\epsilon_0} \quad (1.11)$$

with σ the surface charge and ϵ_0 the vacuum permittivity. However, the electric field in a dielectric material is not zero, but depends on the global system. Hence, in order to model correctly the dielectric wall of the HET, we choose to include the whole dielectric layers inside of the simulation domain.

In this section, we derive the discretization of the Poisson equation with non-uniform permittivity in the 2D radial azimuthal plan using the finite volume approach.

1.5.1 Non-uniform mesh

In the dielectric layers, there is no particle nor charge. Hence, the numerical constraints on the cell size are not applicable, and the cell size can be increased. In order to reduce the cell size difference between two neighbouring cells, we use an exponential growth of the cell size in the radial direction. The cell size in the azimuthal direction Δy is kept constant. The resulting non-uniform mesh can be seen in Fig. 1.9.

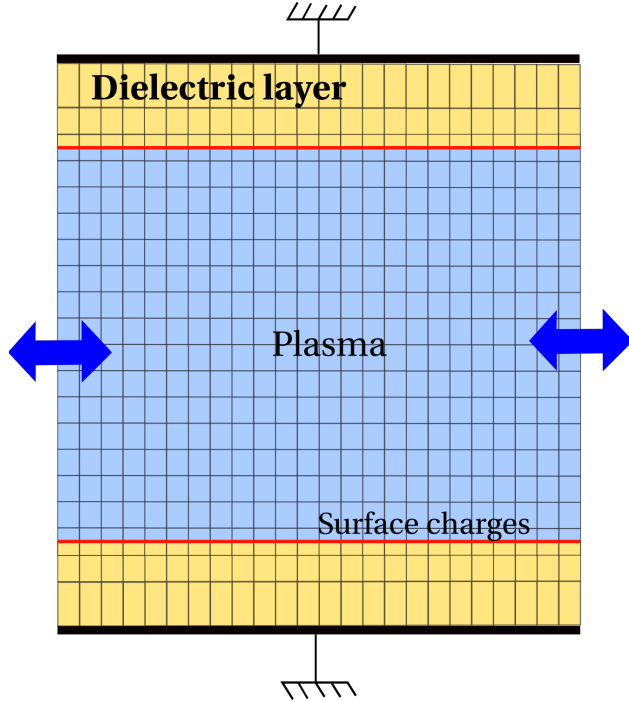


FIGURE 1.9 – Schematic representation of the dielectric layers between the plasma in the 2D radial-azimuthal plan. Are present the dielectric in yellow, the plasma in blue, the surface charges in red and the grounded magnetic circuit in black.

1.5.2 Poisson equation discretization

The dielectric permittivity is $\epsilon = \epsilon_R \epsilon_0$ with ϵ_R the relative permittivity of the dielectric.

The Poisson equation with not-constant permittivity is

$$\nabla \cdot \epsilon \nabla \phi = \rho \quad (1.12)$$

with ρ the charge density. We note $\mathbf{D} = \epsilon \mathbf{E} = \epsilon \nabla \phi$ the electric flux.

Figure 1.10 shows the Cartesian decomposition of the 2D domain. The cell (i, j) has four direct neighbours:

- the est E in $(i + 1, j)$
- the west W in $(i - 1, j)$
- the north N in $(i, j + 1)$
- the south S in $(i, j - 1)$

The cell dimensions are $\Delta x_{i,j}$ and $\Delta y_{i,j}$, and $\Omega_{i,j} = \Delta x_{i,j} \Delta y_{i,j}$ is the cell volume. As the mesh is Cartesian, we have for a given j $\Delta x_{i,j} = cst$ for all i . Hence, we note $\Delta x_{i,j} = d_i$ and $\Delta y_{i,j} = d_j$.

The boundaries are noted $S_{i,j}^s$ with $s = E, W, N$ or S . We can see that $S_{i,j}^W = S_{i-1,j}^E$, and the same goes for the other borders. We note $C_{i,j} = S_{i,j}^E \cup S_{i,j}^W \cup S_{i,j}^N \cup S_{i,j}^S$ the cell surface boundary. The center of the cell is located in i, j and the borders are located in $i \pm 1/2$ in the Est-West direction and $j \pm 1/2$ in the North-Sourth direction.

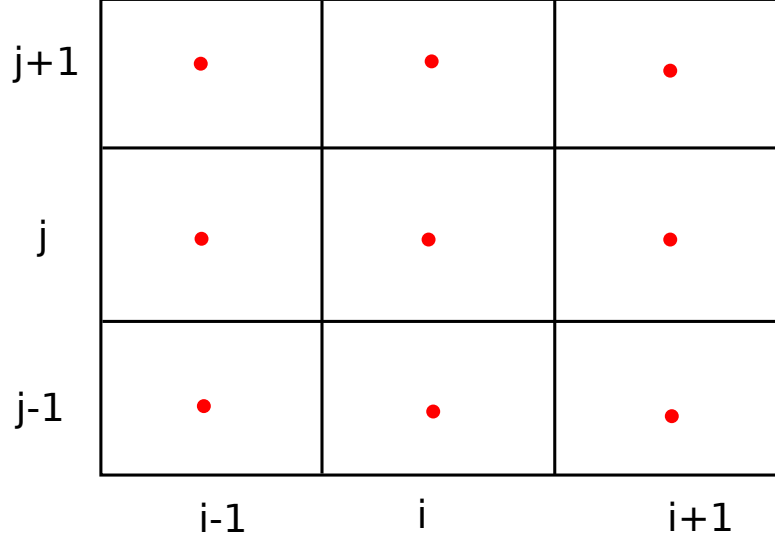


FIGURE 1.10 – Illustration of the Cartesian decomposition of the 2D domain

1.5.3 Poisson equation discretization

We start by positioning the plasma-dielectric interface on the surface between two cells. This means that the permittivity $\epsilon = \epsilon_0 \epsilon_R$ is constant over a cell. In order to discretize the Poisson equation, we integrate Eq. (1.12) ~~on the preceding page~~ over the cell volume

$$\int_{\Omega_{i,j}} -\nabla \cdot (\epsilon \nabla \phi) dv = \int_{\Omega_{i,j}} \rho dv. \quad (1.13)$$

Using Gauss-Ostrogradsky theorem, we obtain

$$\oint_{C_{i,j}} (-\epsilon \nabla \phi) \cdot \mathbf{n} dS = Q_{tot} = \Omega_{i,j} \bar{\rho}, \quad (1.14)$$

with \mathbf{n} ~~is~~ normal vector directed outward, Q_{tot} is the total charge of the cell and $\bar{\rho}$ is the mean value of ρ in the cell. We can decompose the integration over the cell boundary with the four surfaces $S_{i,j}^k$ as

$$\oint_{C_{i,j}} (-\epsilon \nabla \phi) \cdot \mathbf{n} dS = \sum_{k \in \{E,W,N,S\}} S_{i,j}^k \mathbf{D}_{i,j}^k \cdot \mathbf{n} \quad (1.15)$$

with $\mathbf{D}_{i,j}^k$ the flux through the surface k of the cell (i, j) .

Electric flux

Let us define the electric flux through the ~~E~~ border $\mathbf{D}_{i,j}^E$. We suppose there is no surface charges on S^E . We can hence write the electric flux as

$$\mathbf{D}_{i,j}^E \cdot \mathbf{n} = \epsilon_{i,j} E_{x,i+1/2,j}^- \quad (1.16)$$

$$= -\epsilon_{i,j} \frac{\phi_{i+1/2,j} - \phi_{i,j}}{d_i/2}, \quad (1.17)$$

with an off-center discretization of the electric field.

Using the Gauss's law without charges

$$\epsilon_{i,j} E_{x,i+1/2,j}^- - \epsilon_{i+1,j} E_{x,i+1/2,j}^+ = 0, \quad (1.18)$$

we have

$$\epsilon_{i,j} \frac{\phi_{i+1/2,j} - \phi_{i,j}}{d_i/2} = \epsilon_{i+1,j} \frac{\phi_{i+1,j} - \phi_{i+1/2,j}}{d_{i+1}/2}. \quad (1.19)$$

Hence

$$\phi_{i+1/2,j} = \frac{\epsilon_{i,j} d_{i+1} \phi_{i,j} + \epsilon_{i+1,j} d_i \phi_{i+1,j}}{\epsilon_{i,j} d_{i+1} + \epsilon_{i+1,j} d_i}, \quad (1.20)$$

which corresponds to the usual discretization when ϵ and d_i are both constant. Using Eq. (1.20) in Eq. (1.16) we obtain

$$\mathbf{D}_{i,j}^E \cdot \mathbf{n} = 2 \frac{\epsilon_{i,j} \epsilon_{i+1,j}}{\epsilon_{i,j} d_{i+1} + \epsilon_{i+1,j} d_i} (\phi_{i,j} - \phi_{i+1,j}) = 2\epsilon_0 \frac{\epsilon_R i, j \epsilon_R i + 1, j}{\epsilon_R i, j d_{i+1} + \epsilon_R i + 1, j d_i} (\phi_{i,j} - \phi_{i+1,j}) \quad (1.21)$$

We note $Q_{i,j}^E \equiv \frac{\epsilon_{i,j} \epsilon_{i+1,j}}{\epsilon_{i,j} d_{i+1} + \epsilon_{i+1,j} d_i}$. reproducing the same decomposition on the other borders, we obtain

$$S_{i,j}^E Q_{i,j}^E \phi_{i+1,j} + S_{i,j}^W Q_{i,j}^W \phi_{i-1,j} + S_{i,j}^N Q_{i,j}^N \phi_{i,j+1} + S_{i,j}^S Q_{i,j}^S \phi_{i,j-1} - Q_{i,j}^C \phi_{i,j} = -\Omega_{i,j} \rho_{i,j} \quad (1.22)$$

with

$$\begin{cases} Q_{i,j}^E &= 2 \frac{\epsilon_{i,j} \epsilon_{i+1,j}}{\epsilon_{i,j} d_{i+1} + \epsilon_{i+1,j} d_i} \\ Q_{i,j}^W &= Q_{i-1,j}^E \\ Q_{i,j}^N &= 2 \frac{\epsilon_{i,j} \epsilon_{i,j+1}}{\epsilon_{i,j} d_{j+1} + \epsilon_{i,j+1} d_j} \\ Q_{i,j}^S &= Q_{i-1,j}^N \\ Q_{i,j}^C &= Q_{i,j}^E S_{i,j}^E + Q_{i,j}^W S_{i,j}^W + Q_{i,j}^N S_{i,j}^N + Q_{i,j}^S S_{i,j}^S \end{cases}$$

as well as $S_{i,j}^E = S_{i,j}^W = d_i d_z$, $S_{i,j}^N = S_{i,j}^S = d_j d_z$ et $\Omega_{i,j} = d_j d_i d_z$. We observe that the evolution of the vacuum permittivity and the cell size affects the coefficients to be used, but the system stays symmetric.

1.5.4 Including surfaces charges

Let's now considerer the presence of surface charges on the surface $S_{i,j}^E$. Gauss's law now reads

$$-\epsilon_{i,j} E_{x,i+1/2,j}^- + \epsilon_{i+1,j} E_{x,i+1/2,j}^+ = \sigma^E, \quad (1.23)$$

with σ^E the surface charge on the surface. The surface charge is not taken into account when computing the total charge in a cell. Using the same discretization as before, we obtain

$$\epsilon_{i,j} \frac{\phi_{i+1/2,j} - \phi_{i,j}}{d_i/2} - \epsilon_{i+1,j} \frac{\phi_{i+1,j} - \phi_{i+1/2,j}}{d_{i+1}/2} = \sigma^E \quad (1.24)$$

so that

$$\phi_{i+1/2,j} = \frac{\epsilon_{i,j}d_{i+1}\phi_{i,j} + \epsilon_{i+1,j}d_i\phi_{i+1,j}}{\epsilon_{i,j}d_{i+1} + \epsilon_{i+1,j}d_i} + \frac{1}{2}\sigma^E \frac{d_id_{i+1}}{\epsilon_{i,j}d_{i+1} + \epsilon_{i+1,j}d_i} \quad (1.25)$$

hence

$$\mathbf{D}_{i,j}^E \cdot \mathbf{n} = 2 \frac{\epsilon_{i,j}\epsilon_{i+1,j}}{\epsilon_{i,j}d_{i+1} + \epsilon_{i+1,j}d_i} (\phi_{i,j} - \phi_{i+1,j}) - \sigma^E \frac{\epsilon_{i,j}d_{i+1}}{\epsilon_{i,j}d_{i+1} + \epsilon_{i+1,j}d_i}$$

We obtain the same relation that Eq. (1.21) updated by $-\sigma^E \frac{\epsilon_{i,j}d_{i+1}}{\epsilon_{i,j}d_{i+1} + \epsilon_{i+1,j}d_i}$

Hence, we finally obtain

$$S_{i,j}^E Q_{i,j}^E \phi_{i+1,j} + S_{i,j}^W Q_{i,j}^W \phi_{i-1,j} + S_{i,j}^N Q_{i,j}^N \phi_{i,j+1} + S_{i,j}^S Q_{i,j}^S \phi_{i,j-1} - Q_{i,j}^C \phi_{i,j} = -\Omega_{i,j} \rho_{i,j}^- + Q_\sigma^W \sigma^W \quad (1.26)$$

with $Q_\sigma^W = S_{i,j}^W \frac{\epsilon_{i,j}d_{i-1}}{\epsilon_{i,j}d_{i-1} + \epsilon_{i-1,j}d_i}$.



1.5.5 Verifications

We verify the discretization by modeling a capacitor. The relative permittivity of the dielectric inside the capacitor is set to $\epsilon_R = 8$, and a surface charge of $\sigma = 8 \text{ nC.cm}^{-2}$ is imposed on one side, and -8 nC.cm^{-2} on the other side. The expected electric field in the capacitor using the infinite plan approximation is $E = \sigma/(\epsilon_0\epsilon_R) = 1.15 \text{ kV.mm}^{-1}$.

Section 1.5.5 shows the electric field computed using the obtained decomposition. We see that we obtain the expected value for the electric field.

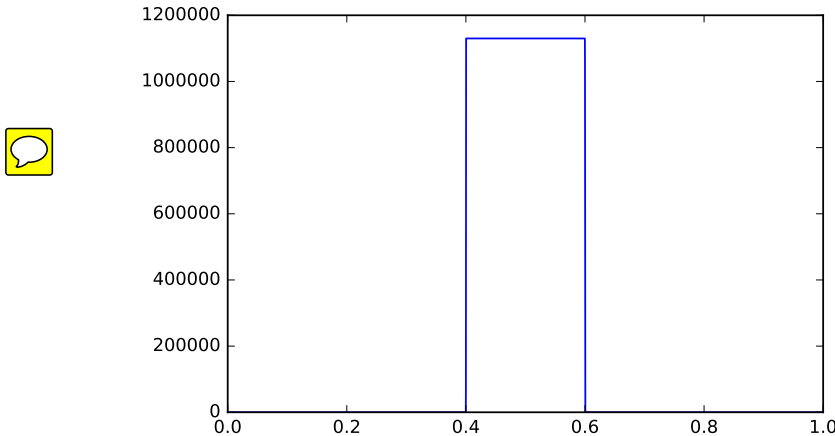


FIGURE 1.11 – Electric field of the capacitor configuration calculated by the Poisson solver in order to validate the discretization and the solver.

1.5.6 Interface at the cell centre

In the previous section, we supposed that the plasma-dielectric dielectric boundary was at the interface between the cells. However, this means that the electric field at the interface is ill-defined. Moreover, the Dirichlet condition is better defined at the cell center. Hence, we chose

to position the plasma-wall interface at the center of the cell. This means that the permittivity is not constant over a cell.

Because the wall boundary^s are only in the radial directions, we consider^e only an interface in the North-South direction. Figure 1.12 shows the domain decomposition. The decomposition is the same as previously, except for the permittivity that can have two different values: one in the North half-planⁿ $\epsilon_{R,i,j}^n$ and another in the South half plan^s $\epsilon_{R,i,j}^s$.

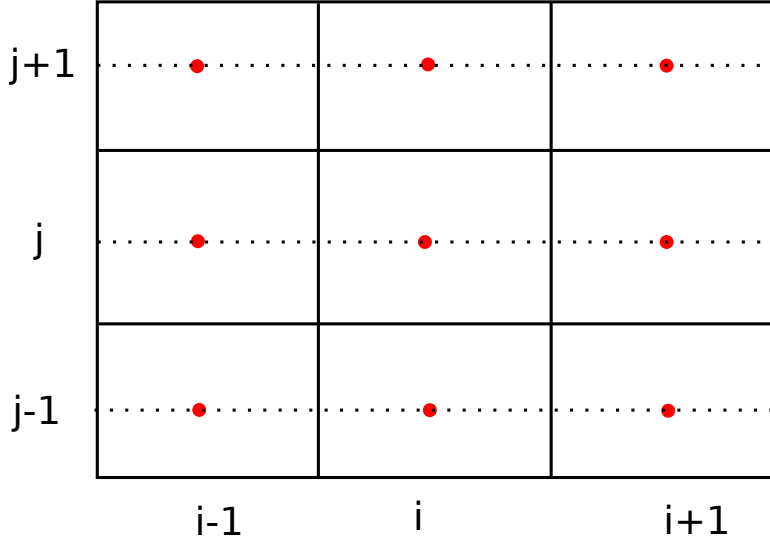


FIGURE 1.12 – Cartesian decomposition of the 2D domain. The dash lines represent discontinuities in the permittivity value.

The discretisation of the Poisson Eq. (1.15) ~~is~~ follows the same path as previously.

~~Except~~ that the electric flux in equation is not constant any more, so that Eq. (1.15) becomes

$$\oint_{C_{i,j}} (-\epsilon \nabla \phi) \cdot \mathbf{n} dS = \sum_{k \in \{E,W,N,S\}} S_{i,j}^k \langle \mathbf{D}_{i,j}^k \cdot \mathbf{n} \rangle. \quad (1.27)$$

We can define

$$\langle \mathbf{D}_{i,j}^E \cdot \mathbf{n} \rangle = \frac{1}{2} \epsilon_{i,j}^N E_{x,i+1/2,j}^- + \frac{1}{2} \epsilon_{i,j}^S E_{x,i+1/2,j}^- \quad (1.28)$$

$$= \frac{-1}{2} (\epsilon_{i,j}^N + \epsilon_{i,j}^S) \frac{\phi_{i+1/2,j} - \phi_{i,j}}{d_i/2} \quad (1.29)$$

so that in the Est-West direction, the flux behave as if the cell permittivity is the mean of the North and South half plan $\epsilon_{i,j} = \frac{1}{2}(\epsilon_{i,j}^N + \epsilon_{i,j}^S)$. Hence, the rest of the computation ~~are~~ similar. For the boundary North and South, the permittivity is constant, hence there is no modification. Consequently, we obtain the discretization

$$S_{i,j}^E Q_{i,j}^E \phi_{i+1,j} + S_{i,j}^W Q_{i,j}^W \phi_{i-1,j} + S_{i,j}^N Q_{i,j}^N \phi_{i,j+1} + S_{i,j}^S Q_{i,j}^S \phi_{i,j-1} - Q_{i,j}^C \phi_{i,j} = -\Omega_{i,j} \rho_{i,j}^- \quad (1.30)$$

with

$$\begin{cases} Q_{i,j}^E = 2 \frac{\epsilon_{i,j}\epsilon_{i+1,j}}{\epsilon_{i,j}d_{i+1} + \epsilon_{i+1,j}d_i} \\ Q_{i,j}^W = Q_{i-1,j}^E \\ Q_{i,j}^N = 2 \frac{\epsilon_{i,j}^N\epsilon_{i,j+1}^S}{\epsilon_{i,j}^Nd_{j+1} + \epsilon_{i,j+1}^Sd_j} \\ Q_{i,j}^S = 2 \frac{\epsilon_{i,j}^S\epsilon_{i,j-1}^N}{\epsilon_{i,j}^Sd_{j+1} + \epsilon_{i,j-1}^Nd_j} \\ Q_{i,j}^C = Q_{i,j}^E S_{i,j}^E + Q_{i,j}^W S_{i,j}^W + Q_{i,j}^N S_{i,j}^N + Q_{i,j}^S S_{i,j}^S \end{cases}$$

As well as $S_{i,j}^E = S_{i,j}^W = d_id_z$, $S_{i,j}^N = S_{i,j}^S = d_jd_z$ et $\Omega_{i,j} = d_jd_id_z$. Here, the system is no more symmetric. However, we can suppose that the only permittivity jump [appears](#) at the cell center, so that $\epsilon_{i,j}^S = \epsilon_{i,j-1}^N$. Hence, $Q_{i,j}^N = 2 \frac{\epsilon_{i,j}^N}{d_{j+1} + d_j}$ and the [system is symmetric](#).

1.5.7 Surface charges for centred interface

in the case of centered plasma-wall interface, we have surfaces charges at the center of the cell. Hence

$$\int_{\Omega_{i,j}} \rho dv = \Omega_{i,j} \bar{\rho} + S_{i,j}^N \sigma_{i,j}. \quad (1.31)$$

The surface charges behave like volume charges. Hence, we obtain

$$S_{i,j}^E Q_{i,j}^E \phi_{i+1,j} + S_{i,j}^W Q_{i,j}^W \phi_{i-1,j} + S_{i,j}^N Q_{i,j}^N \phi_{i,j+1} + S_{i,j}^S Q_{i,j}^S \phi_{i,j-1} - Q_{i,j}^C \phi_{i,j} = -\Omega_{i,j} \bar{\rho}_{i,j} - S_{i,j}^N \sigma_{i,j} \quad (1.32)$$

The discretization obtained for the plasma-wall interface cell-centred is very similar to the one obtained for the interface at the cell interface. However, it conserves the particle domain when the dielectric layer is not modeled and [that](#) Dirichlet conditions are applied, and the electric field at the plasma-wall interface is better defined. Hence, the cell-centred interface will be used.

1.6 Axial Convection model

As introduce [in](#) the previous section, the [2D](#) radial-azimuthal simulation [do not](#) model a priori the axial convection of the particles.

1.6.1 Lafleur's model of convection

Lafleur et al. [24] proposed a way to model the axial convection of the particles in a [1D](#) purely azimuthal simulation. Figure 1.13 shows a schematic illustration of the model. The principle is as follow

- We set a finite axial length, noted L_z on Fig. 1.13.
- We follow the positions of the particle in the axial direction z
- When a particle crosses the boundary, it is removed.
- A new particle is created
 - at $z = 0$ for the ions

— at $z = L_z$ for the electrons

We create a new particle in order to conserve the charge in the simulation. The new particle has a velocity following a Maxwellian flux distribution function of a given temperature. The azimuthal position of the particle is chosen uniformly at random.

Add definition of the Maxwellian and maxellian flux VDF ?

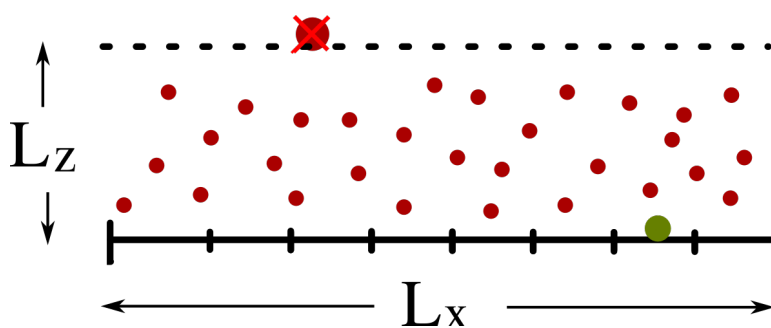


FIGURE 1.13 – Schematic representation of Trevor’s convection model [24]. The red particle is removed of the simulation, and the green particle is created. In this illustration, the particle is an ion, as the reinjection is at $z = 0$.

Lafleur’s model of convection has been adopted in 2D by Croes et al. [10]. The principle is exactly similar. The particles are followed in the 3 directions, and a finite length is used to close to axial direction. It is important to note that even if the particles are followed in the 3 directions, the meshed domain is only 2D. The simulation is not 3D-3 dimension for the velocity (3V), but only 2D-3V.

In Croes et al. [10], the authors have observed that if the newly created particle has a radial position chosen uniformly at random, it would affect the sheath. Hence, they decided to use the same radial position that the removed particle. Figure 1.14 presents a schematic representation of the convection model in 2D.

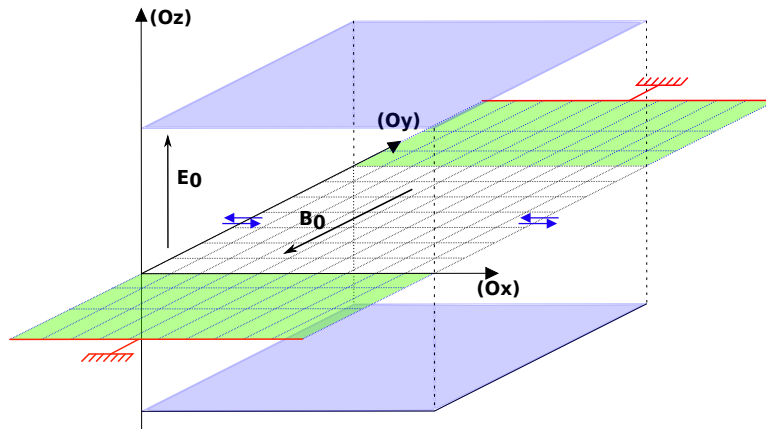


FIGURE 1.14 – Schematic representation of the Lafleur’s convection model adapted in 2D. The new particle radial position corresponds to the removed particle, but its azimuthal position is chosen uniformly at random.

Figure 1.15 shows the evolution as a function of time of the electron mean energy in the simulation in a typical 2D radial-azimuthal simulation, adapted from Croes [9]. We can see

that without the convection, the mean energy quickly rises to unphysical values. When the convection is modeled, using an axial of $L_z = 1$ cm, the energy reaches a steady state.

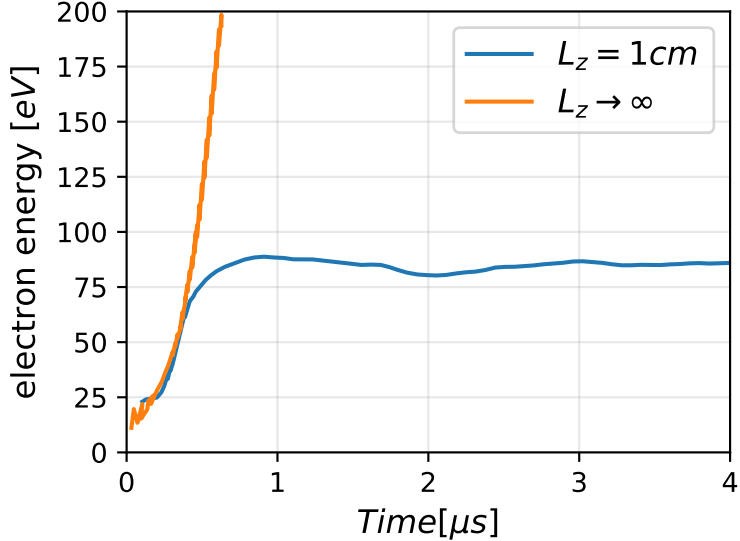


FIGURE 1.15 – Time evolution of the electron mean energy when the convection is not modeled ($L_z \rightarrow \infty$) and with Trevor’s convection model used, $L_z = 1$ cm. Adapted from Croes [9].

1.6.2 Numerical artefacts

Lafleur et al. [24] studied the impact of the convection model on the simulation results. The authors observed in particular that changing the azimuthal length of the simulation domain could affect the simulation results.

Figure 1.16 shows the time evolution of the azimuthal electric field E_θ from the 1D simulation [24].

On the first row (Fig. 1.16.a and b), the length of the periodic azimuthal direction is $L_\theta = 0.5$ cm. Fig. 1.16.a corresponds to the case without axial convection. We clearly see that the ECDI rises and do not saturate. The wavelength is short, of the order of $\lambda = 1.5$ mm. Fig. 1.16.b corresponds to the same case as Fig. 1.16.a but this time with the axial convection modeled. We observe this time a saturation of the oscillation’s amplitude, and the wavelength is close to $\lambda \simeq 1.5$ mm.

On the second row (Fig. 1.16.c and d), the length of the periodic azimuthal direction is $L_\theta = 1$ cm. Fig. 1.16.c corresponds to the case without axial convection, and Fig. 1.16.b corresponds to the same case but this time with the axial convection modeled. In Fig. 1.16.c, we can see that increasing the azimuthal length did not affect the ECDI, as expected. However, in Fig. 1.16.d, the instability is clearly affected. A single oscillation is observed, corresponding to $\lambda = 10$ mm. They are most certainly unphysical.

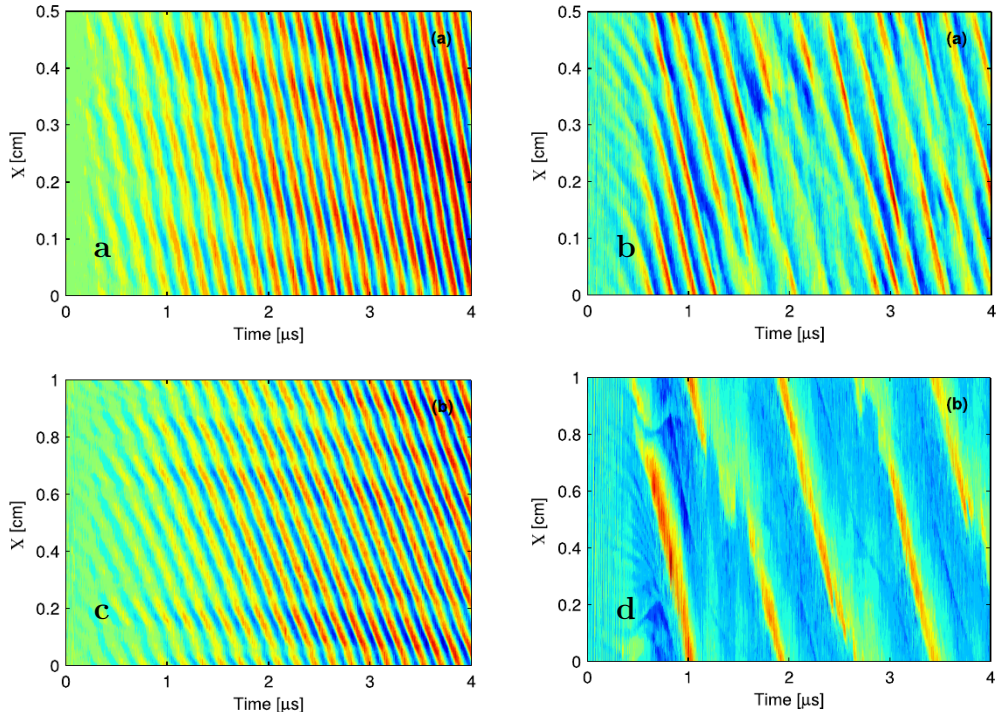


FIGURE 1.16 – Effects of Lafleur’s convection model for two different azimuthal length on the azimuthal electric field. (a) No convection, $L_x = 0.5 \text{ cm}$, (b) convection modeled, $L_x = 0.5 \text{ cm}$, (c) No convection, $L_x = 1 \text{ cm}$, (d) convection modeled, $L_x = 1 \text{ cm}$. The colour of each plots is normalized to the maximum amplitude. Adapted from [24].

Get θ back to y instead of x

Croes [9] observed similar behaviour with the bidimensional simulation. The author investigated the values of the azimuthal length which presented physical and unphysical results for different values of the axial length. Figure 1.17 shows the results obtained (adapted from [9]). We can see that for a given value of the axial length, the azimuthal must be ~~lower~~ than a certain value to present physical results. However, the value of this upper limit depends of the axial length, such that ~~the~~ if the axial length decreases, the upper limit of the azimuthal length decreases as well.

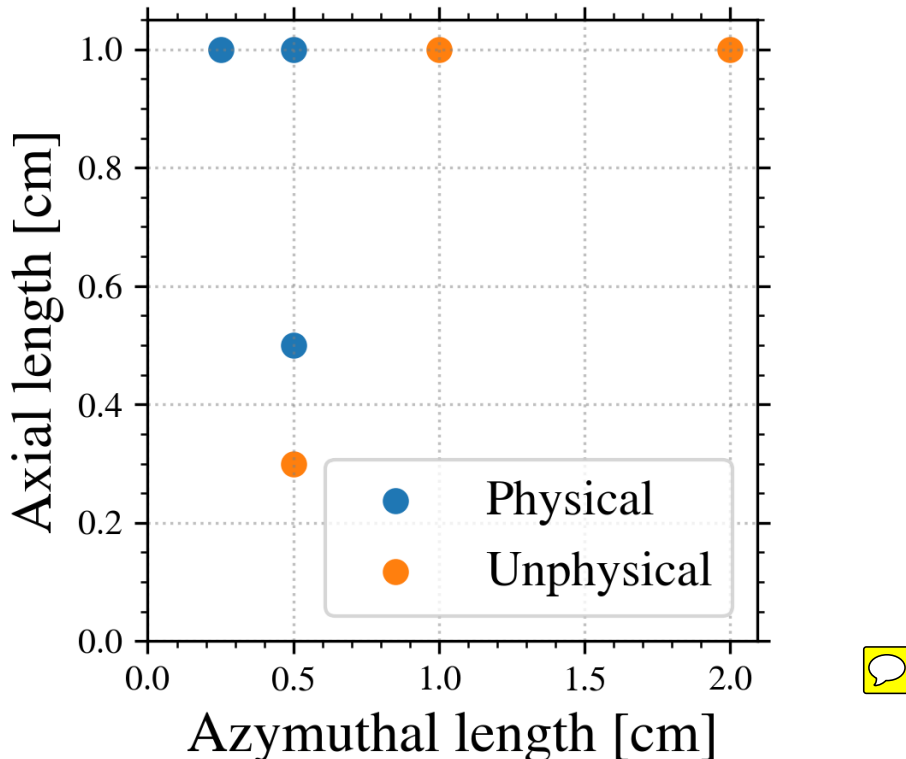


FIGURE 1.17 – Values of the azimuthal length and the axial length for which the simulation result is physical (similar to Fig. 1.16.b) or unphysical (similar to Fig. 1.16.d)

Make this image smaller (smaller font, etc.)

~~No explanation have been proposed, yet.~~ In the next section, we develop a theory that could explain the observation, and a new convection model for the simulation is proposed.

1.6.3 Numerical noise of Lafleur's convection model

Let us consider ~~de~~ Lafleur's convection model in 1D on the charge density. When computing the charge density on the mesh vertices, the axial position is not taken into account. Consequently, the convection process illustrated on Fig. 1.13 is similar to moving a particle arbitrarily (read randomly). Seen by the charge density, this is similar to a Poisson noise, also named shot noise, on the charge density.¹

1. Actually, this noise is the combination of a Poisson noise with a uniform noise, happening twice for every particles convection, once with a positive charge and once with a negative charge.

After a certain number of particles removed and created, the Poisson noise is similar to a Gaussian noise, also named thermal noise, following a normal distribution \mathcal{N} . Hence, the charge density becomes²

$$\rho = \rho_0 + \mathcal{N}(0, \sigma_{\text{Reinj}}), \quad (1.33)$$

with ρ the charge density, ρ_0 the charge density without the convection process, and σ_{Reinj} the standard deviation of the distribution of the noise associated with the convection model. Surprisingly, the noise due to the convection model is similar to the numerical noise induced by the decomposition of the plasma into particles $\mathcal{N}(0, \sigma_{\text{stat}})$. However, the amplitude of this statistical noise decreases with the number of particles per cell used

$$\sigma_{\text{stat}} \propto \frac{1}{\sqrt{N_{pc}}}.$$

On the other hand, the amplitude of the noise induced by the convection model depends on the plasma density n , the axis velocity of the particles v_z and the axial length L_z

$$\sigma_{\text{Reinj}} \propto \frac{n}{L_z} v_z. \quad (1.34)$$

We can see on Eq. (1.34) that the amplitude of the convection induced noise on the charge density is proportional to the inverse of the axial length L_z . This could explain the observation of Fig. 1.17 when using a smaller L_z . However, it does not explain the effects of the azimuthal length observed in Figs. 1.16 and 1.17.

1.6.4 Effect of the noise on the electric field

In order to explain the impact of the azimuthal length on the instability, we can study the azimuthal electric field E_θ resulting of the charge density ρ . As the Poisson equation is linear, we have

$$E_\theta(\theta) = C + \frac{1}{\epsilon_0} \int_0^\theta \rho(s) ds \quad (1.35)$$

$$= C + \frac{1}{\epsilon_0} \int_0^\theta (\rho_0(s) + \mathcal{N}(0, \sigma_{\text{Reinj}})) ds \quad (1.36)$$

$$= C + E_{\theta,0} + E_{\theta,1} \quad (1.37)$$

with C a constant that ensure that the periodical Boundary Conditions (BC) are respected. The part of the electric field $E_{\theta,0}$ corresponds to the unperturbed charge density ρ_0 and $E_{\theta,1}$ corresponds to the noisy charge density $\mathcal{N}(0, \sigma_{\text{stat}})$. Hence, let us focus now on $E_{\theta,1}$. We can study $E_{\theta,1}$ using two equivalent means: the Fourier Transform (FT) and the Brownian bridge.

Fourier Transform

Applying the FT on the equation

$$E_{\theta,1} = \frac{1}{\epsilon_0} \int_0^\theta \mathcal{N}(0, \sigma_{\text{Reinj}}) ds \quad (1.38)$$

2. One can note that the mean of the noise is strictly zero, as the charge density is conserved.

gives

$$\mathcal{FFT}(E_{\theta,1})(k) = \frac{1}{\epsilon_0} \mathcal{FFT} \left(\int_0^\theta \mathcal{N}(0, \sigma_{\text{Reinj}}) ds \right) \quad (1.39)$$

$$= \frac{1}{\epsilon_0} \frac{\mathcal{N}(\mu_{\text{FT}}, \sigma_{\text{FT}})}{k} \quad (1.40)$$

Equation (1.40) shows that $E_{\theta,1}$ also follows a Gaussian distribution, but with a non-zero mean value. It is also inversely proportional to the wave number k . Hence, when we increase the azimuthal length, which means that small wave number can exit in the simulation domain, the amplitude of $E_{\theta,1}$ increases as well.

Brownian Bridge

Equation (1.38), combined with the BC, is the definition of the a Brownian bridge.

A Brownian bridge is a particular Brownian motion that reaches at a given distance the same value that the initial value. Hence, we have [40]

$$\begin{aligned} \mathbb{E}(E_{\theta,1}) &= 0, \\ \text{var}(E_{\theta,1}) &= \sigma_{\text{Reinj}}^2 \frac{L_\theta}{4} \end{aligned}$$

Hence, ~~increases~~ the azimuthal length increases the amplitude of $E_{\theta,1}$.

We believe that when the amplitude of $E_{\theta,1}$ is too large, it can trigger an unphysical oscillation. The next section uses this conclusion in order to adapt the convection model.

1.6.5 Noiseless convection model

~~Have~~ have shown that the convection model induces a noise in the charge density, that produces an azimuthal electric field which amplitudes depends on the azimuthal length.

We propose here a modified version of Lafleur's convection model in order to remove the noise in the charge density, ~~so that is expected to not present the numerical artefacts see previously~~. The noiseless convection model follows the same algorithm that before, but the azimuthal position of the particle created is not chosen uniformly as random, but instead the new particle has the same position as the removed particle. Figure 1.18 shows a schematic illustration of the noiseless convection algorithm applied on a particle.

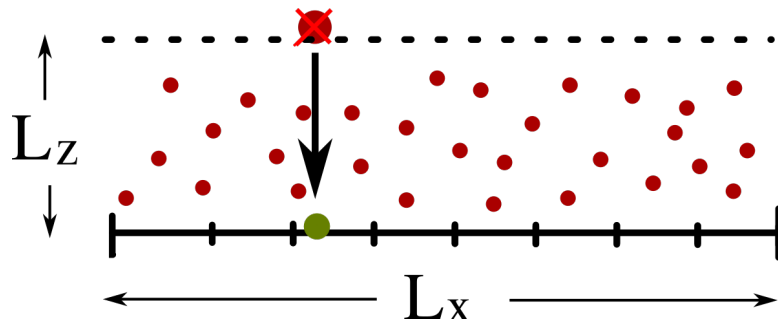


FIGURE 1.18 – Illustration of the noiseless convection model

We have implemented this modified convection model in the 2D radial-azimuthal simulation.



Figure 1.19 shows the time evolution of the azimuthal electric field at the center of the radial dimension with and without the noiseless convection model. It presents the same conditions that in Fig. 1.16.a and b. As previously, the convection stabilises the growth of the instability to a steady-state, but it does not affect the physics.

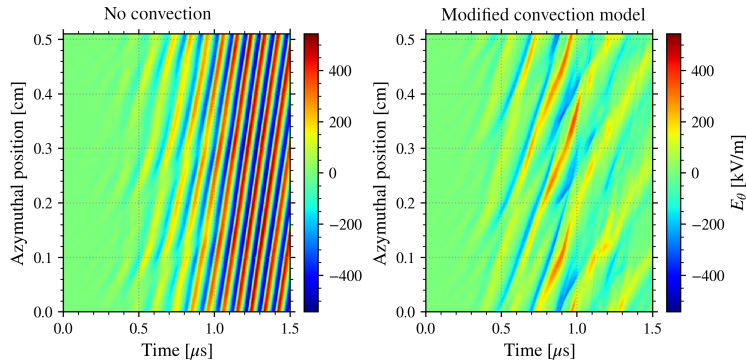


FIGURE 1.19 – Time evolution of the azimuthal electric field at the center of the radial dimension with and without the noiseless convection model.

Figure 1.20 shows the time evolution of the azimuthal electric field at the center of the radial dimension with the convection modeled using Lafleur's model and the noiseless model with a small azimuthal length. We can see that the two models gives almost exactly the same results.

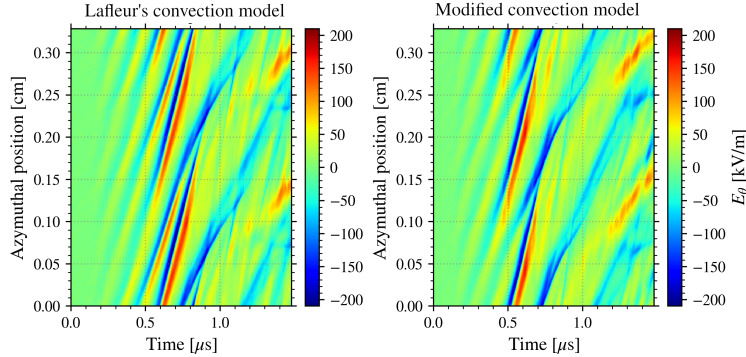


FIGURE 1.20 – Time evolution of the azimuthal electric field at the center of the radial dimension with the convection modeled using (left) Lafleur's model and (right) the noiseless model with a small azimuthal length.

Figure 1.21 shows the time evolution of the azimuthal electric field at the center of the radial dimension with the convection modeled using Lafleur's model and the noiseless model but using a longer azimuthal length than Fig. 1.20. In this cases, we can see that Lafleur's convection model induces oscillations that are not observed with the noiseless model.

These observations have shown that Trevor's convection model induces a noise on the charge density, that do not affect the simulation when the domain size is small, but can rise numerical artefacts when the domain size is larger. We have seen that the minor modification on the model do not affect the simulations results on a small domain, but allow us to use larger simulation domain without any numerical artefacts.

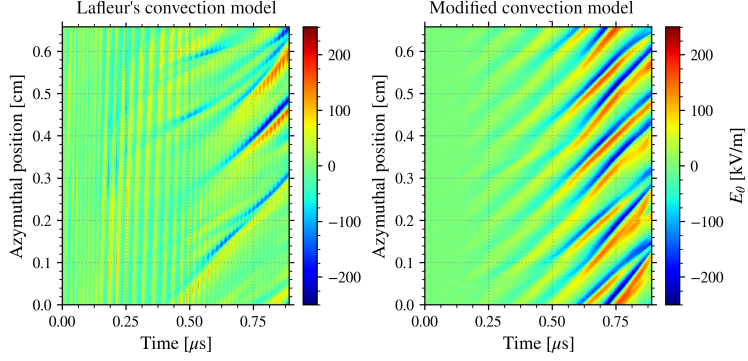


FIGURE 1.21 – Time evolution of the azimuthal electric field at the center of the radial dimension with the convection modeled using (left) Lafleur’s model and (right) the noiseless model with a longer azimuthal length.

Unfortunately, the new model has been developed during the last year of my theses. Hence, the first simulation results have been obtained using Lafleur’s convection model. As seen in Fig. 1.20, on a small geometry the results are not affected, hence there is no need to verify all of the simulations obtained. On the other hand, in order to study the instability, it is useful to have a longer azimuthal, in order to obtain a more resolved frequency spectra. Hence, the modified convection model used in this case.

1.6.6 Effects on a 2D simulation domain

The mathematical development of Section 1.6.4 has been done in 1D. We can legitimately wonder if the results can be extended directly to a 2D domain. A mathematical definition of $E_{\theta,1}$ is more difficult, as we have, neglecting the dielectric layers,

$$E_{\theta,1} = \partial_\theta \phi_1 \text{ such that } \nabla \cdot \nabla \phi_1 = -\frac{\mathcal{N}(0, \sigma_{\text{Reinj}})}{\epsilon_0} \text{ following the BC.} \quad (1.41)$$

The BCs are

- periodic BC in the azimuthal direction,
 - Dirichlet BC in the radial direction, modeling grounded walls,
- which translate as

$$\phi = 0 \text{ for } r = 0 \text{ and } r = L_r, \quad \forall \theta \quad (1.42)$$

$$\phi(\theta = 0) = \phi(\theta = L_\theta), \quad \forall r \quad (1.43)$$

Solving Eqs. (1.41) to (1.43) analytically is much more difficult than the 1D development because of the Dirichlet BC. However, we can investigate it numerically, by solving Eq. (1.41) for a given random source term. Using a Monte Carlo approach, the results are averaged 50 times in order to better observe the mean behaviour in respect to the noise (i.e. increasing signal to noise ratio).

Figure 1.22 shows the Discrete Fourier Transform (DFT) of the source term

$$\rho_1 = \mathcal{N}(0, \sigma_{\text{Reinj}}),$$

the resulting azimuthal electric field $E_{\theta,1}$ and plasma potential ϕ computed on the centreline of the simulation domain in the radial direction, for three different radial length expressed in number of cell N_x . Is also showed the "equivalent" source term ρ_{eq} , which is the source term that would give the frequency spectra of $E_{\theta,1}$ observed in a 1D domain

$$\rho_{\text{eq}} = \epsilon_0 \partial_\theta E_{\theta,1}. \quad (1.44)$$

The results are given for different radial length $N_x = 15, 50$ and 200 , while the azimuthally length $N_y = 200$ is kept constant. We can see that the plasma potential and the electric field show larger amplitude for small wave numbers (large wavelength) compared to large wave numbers in the three cases. However, the amplitude of the smaller wave numbers is affected. In the cases of small radial length ($N_x = 15$ and 50), the spectra of the electric field is not monotonic. This can be explained by the Dirichlet BCs that pin down the fluctuation of the plasma potential.

However, even though the amplitude is reduced in 2D with small radial direction compared to a 1D model, we still observe large amplitude of small wave number oscillations in both the electric field and the plasma potential. Hence, the conclusions of Section 1.6.4 derived in 1D can be legitimately used for 2D domains.

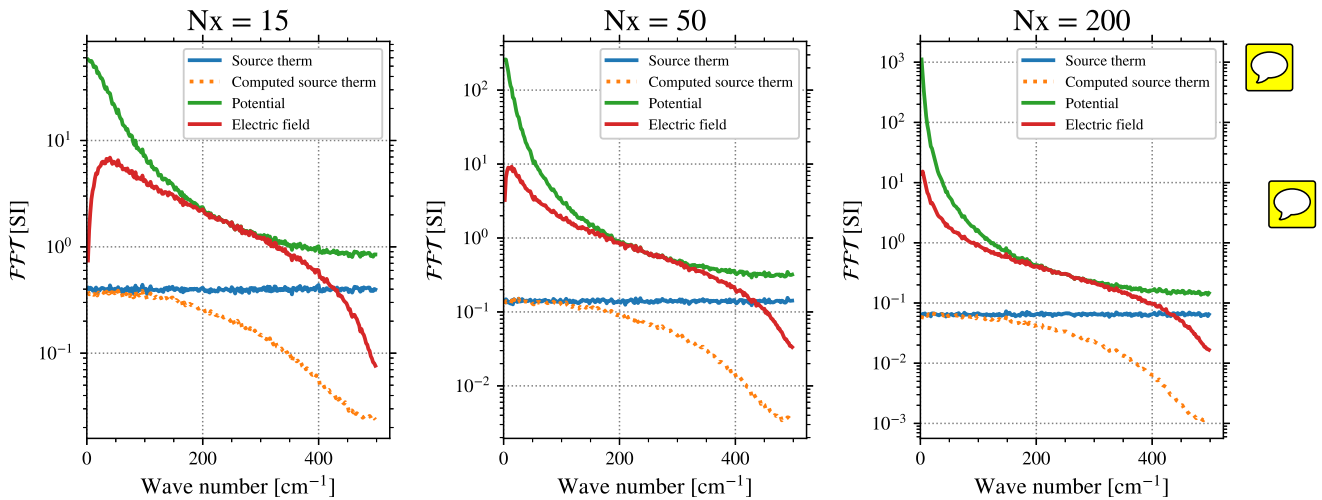


FIGURE 1.22 – DFT of the source term $\rho_1 = \mathcal{N}(0, \sigma_{\text{Reinj}})$, the resulting azimuthal electric field $E_{\theta,1}$ and plasma potential ϕ computed on the centreline of a radial-azimuthal simulation, and the "equivalent" source term defined by Eq. (1.44). $N_y = 200$.

1.7 Secondary electron emission

When an incident electron reaches the wall material, several scenarios are possible, as described in Villemant [41]

1. Elastic reflection: the electron undergoes only elastic collision with the material, hence its energy is constant. However, its reflection is not necessarily specular.
2. Inelastic reflection: the electron loses some of its energy to the material before returning to the plasma.

3. Secondary electron emission: the energy of the primary electron is enough to extract one or more electrons from the material.
4. No emission, the electron is absorbed by the wall.

The probability σ that one event happens instead of another depends predominantly on the particle energy, and weakly on its impact angle. Concerning the mean flux of electron incident and emitted, we uses the mean emission rate, or yield, $\bar{\sigma}$

$$\bar{\sigma} = \frac{\Gamma_{e,\text{secondary}}}{\Gamma_{e,\text{primary}}}$$

which can be developed using the distribution function to

$$\bar{\sigma} = \frac{\iiint_{\Omega} v_x \sigma(\mathbf{v}_e) f(\mathbf{v}_e) d^3 v}{\iiint_{\Omega} v_x \sigma(\mathbf{v}_e) f(\mathbf{v}_e) d^3 v}$$

with Ω the ensemble of \mathbf{v}_e directed toward the wall: $\mathbf{v}_e \cdot \mathbf{n} > 0$, with \mathbf{n} the unit vector normal to and toward the wall.

1.7.1 Models of emission

Several models can be used to describe the electron emission.

Monte Carlo models are the more realistic. They are based on the computation of the trajectory of the electrons through the material, during which the electron can encounter several interactions with the material. Each interactions can modify the electron direction, energy, and generate new electron. Several models have been proposed, as Furman and Pivi [42], Pierron et al. [43]. These models allow a precise characterization of the processes, but depends of a large number of parameters difficult to obtain due to the lack of experimental data.

Analytical models provides a simplified description of the rate of emission. Their complexity depends of the precision desired. The more largely used are the models of Vaughan [44], Barral et al. [14], Sydorenko et al. [45].

In this work, we only are interested in representing qualitatively the electron emission. Moreover, Croes [9] showed that changing the model used do not affect significantly the results. Hence, we will use the model of Barral et al. [14] for its simplicity.

1.7.2 Electron emission model used

The emission model used in the works follow a linear-saturated law for the probability of emission with three parameters. It describes the total emission corresponding to the sum of the elastic and inelastic backscattering and the secondary electron emission.

$$\sigma(\epsilon) = \begin{cases} \sigma_0 + (1 - \sigma_0) \frac{\epsilon}{\epsilon^*} & \text{if } \epsilon < \epsilon_{\max} \\ \sigma_{\max} & \text{if } \epsilon \geq \epsilon_{\max} \end{cases} \quad (1.45)$$

where ϵ is the kinetic energy of the incoming electron, σ_0 is the asymptotic probability of emission at energy null, ϵ^* is the crossover energy above which the probability of emission is higher than one, σ_{\max} is the maximum probability and $\epsilon_{\max} = \frac{\sigma_{\max}-\sigma_0}{1-\sigma_0}\epsilon^*$ is the minimum energy for which $\bar{\sigma} = \sigma_{\max}$. Equation (1.45) is illustrated in Figure 1.23.

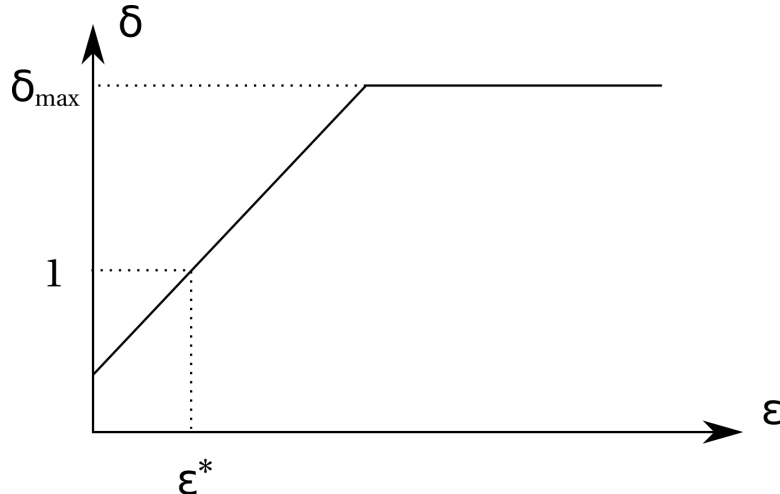


FIGURE 1.23 – Linear-saturated emission model from Barral et al. [14].

We suppose that all of the electrons emitted are isotropically emitted following a Maxwellian flux distribution function of temperature T_{SEE} . The parameters σ_0 , σ_{\max} and ϵ^* can be obtained from experiments. Table 1.2 shows the crossover energy and the probability of emission at energy null for different materials. The value of σ_0 is always close to 0.5, but ϵ^* can vary from 18 to 305 V. Hence, in the following parametric studies, σ_0 will be kept at 0.5 while we vary ϵ^* from low values, corresponding to highly emissive materials, to high values, representing less emissive materials.

TABLE 1.2 – Emission parameters for different materials from Barral et al. [14].

Material	ϵ^* (V)	σ_0
BN-SiO ₂	53	0.45
Al ₂ O ₃	18	0.57
SiC	43	0.69
Graphite	305	0.40

1.8 Electron cross-field transport



The electron mobility in the axial direction μ_e is defined as the ratio between the mean velocity u and the electric field

$$\mu_e = \frac{u_{e,z}}{E_z} \quad (1.46)$$

with $u_{e,z} = \langle v_{e,z} \rangle$ the electron mean velocity. In the PIC simulations, Eq. (1.46) can be used directly to compute μ_{PIC} .

In the classical drift diffusion theory of the electron mobility transverse to a magnetic field, the mobility is due to collisions as seen in Section 1.1.4 on page 16

$$\mu_{\text{classical}} = \frac{e}{m_e} \frac{\nu_m}{\nu_m^2 + \omega_{ce}^2} \quad (1.47)$$

with $\omega_{ce} = \frac{eB}{m_e}$ the electron cyclotron frequency and ν_m the electron-neutral momentum transfer collision frequency.

At the exit plane, the classical mobility predicts a mobility of the order of $\mu_{\text{classical}} = 0.001 - 0.01 \text{ m}^2(\text{Vs})^{-1}$ [23].

The kinetic approach allowed Lafleur et al. [24] to propose a modified mobility due to the oscillations of the electron density and the azimuthal electric field of the ECDI. This effective mobility obtained is

$$\mu_{\text{eff}} = \mu_{\text{classical}} \left(1 - \frac{\omega_{ce}}{\nu_m} \frac{\langle \delta n_e \delta E_\theta \rangle_\theta}{n_0 E_z} \right) \quad (1.48)$$

with δn_e and δE_θ the fluctuations in the azimuthal directions of the electron density and azimuthal electric field, respectively, the operator $\langle \cdot \rangle_\theta$ is the average in the azimuthal direction, and n_0 is the average plasma density. In the case where $\nu_m \ll \omega_{ce}$, Eq. (1.48) can be simplified to

$$\begin{aligned} \mu_{\text{eff}} &= \frac{\frac{e}{m_e} \nu_m}{\omega_{ce}^2} \left(1 - \frac{\omega_{ce}^2}{\nu_m} \frac{\langle \delta n_e \delta E_\theta \rangle_\theta}{n_0 E_z} \right) \\ &= \frac{\langle \delta n_e \delta E_\theta \rangle_\theta}{n_0 E_z} \frac{1}{B_r} \end{aligned} \quad (1.49)$$

which shows that the instability enhances the electron axial mobility in a wave similar to an $E \times B$ drift. The electric field E_θ oscillates and presents a zero mean value, but the average effect on the electron transport is not zero if the correction between δE_θ and δn_e is not zero.

In Lafleur et al. [24], the authors present the instability effect as an electron-ion friction force $R_{ei} = -e \langle \delta n_e \delta E_\theta \rangle_\theta$. Under the assumption that the saturation of the instability is mainly due to ion trapping, the electron-ion friction force can be simplified in the 2D geometry of the simulation to

$$R_{ei}^{sat} = \frac{e |\nabla \cdot (n_e T_e \mathbf{v}_i)|}{4\sqrt{6}c_s} \simeq \frac{en_e T_e v_{i,out}}{4\sqrt{6}c_s L_z} \quad (1.50)$$

where \mathbf{v}_i is the ion velocity, $c_s = (eT_e/m_i)^{1/2}$ is the ion sound speed, and the spatial derivative has been approximated across the axial simulation direction, with $v_{i,out}$ the ion outlet velocity

$$v_{i,out} = \sqrt{\frac{2eU_z}{m_i}}, \quad (1.51)$$

with $U_z = E_z L_z$ the total potential difference in the axial direction.

Using Eq. (1.50) in Eq. (1.49), we obtain the simplified expression of the effective mobility at saturation

$$\mu_{\text{eff}}^{sat} = \frac{\sqrt{\frac{T_e}{U_z}}}{4\sqrt{3}B_r}. \quad (1.52)$$

Equation (1.52) shows that for the radial and azimuthal 2D geometry being used here, the enhanced mobility due to ECDI scales as the square-root of the electron temperature T_e if the simulation parameters are constant. However, it is not the case in general, as the saturation of the instability can be also due to convection, and there are axial gradients in the electron temperature and plasma density as well.

We can note that μ_{PIC} , μ_{eff} and $\mu_{\text{classical}}$ are defined at every position of the simulation, but that $\mu_{\text{eff}}^{\text{sat}}$ can only be globally calculated.

1.9 Sheath model with electron emission

Ici, le model est introduit rapidement... Peut-etre le faire plus explicitement a partire des equations fluides ?

The sheath model featuring SEE processes has been historically studied by Hobbs and Wesson [Hobbs and Wesson \[46\]](#), but is still an active research topic nowadays [\[47\]](#). The sheath is often considered to be collision-less and isothermal, while the plasma is composed of hot Maxwellian electrons and cold ions. A third population of electron-induced secondary electrons is also present in the sheath, and the re-emission rate $\bar{\sigma}$ is assumed to be constant. The SEE process modifies the potential drop in the sheath as [\[46\]](#)

$$\Delta\phi_{\text{sheath}} = T_{e\parallel} \ln \left((1 - \bar{\sigma}) \sqrt{\frac{m_i}{2\pi m_e}} \right) \quad (1.53)$$

with $T_{e\parallel}$ the electron temperature in the direction parallel to the magnetic field, thus normal to the walls. Adding a pre-sheath drop of $T_{e\parallel}/2$ [\[48\]](#), the total potential drop to the wall becomes

$$\Delta\phi = \Delta\phi_{\text{sheath}} + \frac{T_{e\parallel}}{2} = T_{e\parallel} \left(\frac{1}{2} + \ln \left[(1 - \bar{\sigma}) \sqrt{\frac{m_i}{2\pi m_e}} \right] \right) \quad (1.54)$$

In Equations (1.53) and (1.54), we use $T_{e\parallel}$ as in general, and more precisely for low-pressure magnetized plasma, the electrons can be anisotropic.

We can see that Eq. (1.53) becomes negative for a critical value of the emission rate

$$\bar{\sigma}_{\text{max}} = 1 - \sqrt{\frac{2\pi m_e}{m_i}} \simeq 0.985 \text{ for Xenon.} \quad (1.55)$$

However, before that $\bar{\sigma}$ attains $\bar{\sigma}_{\text{max}}$, the model of Hobbs and Wesson [\[46\]](#) presents another behaviour against the hypotheses of Eq. (1.53), as the sheath becomes Space Charge Limit (SCL). In the SCL conditions, the electron emission is so large that the electric field at the wall becomes zero

$$\left. \frac{\partial\phi}{\partial r} \right|_{\text{wall}} = 0 \quad (1.56)$$

In this case, the plasma potential drop to the wall for any ion mass is [\[46\]](#)

$$\Delta\phi_{\text{SCL}} \simeq 1.02 T_{e\parallel}, \quad (1.57)$$

and the limit emission rate is

$$\bar{\sigma}_{\text{cr}} \simeq 1 - 8.3 \sqrt{\frac{m_e}{m_i}} \quad (1.58)$$

For xenon, Eq. (1.58) gives $\bar{\sigma}_{\text{cr}} = 0.983$ [49].³

Figure 1.24 illustrates the sheath model of Hobbs and Wesson [46] by showing the plasma potential profile in the sheath for different values of electron emission rate for a xenon plasma. Fig. 1.24.a gives the potential ϕ normalized by $\Delta\phi_{\text{sheath}}$ from Eq. (1.53), and Fig. 1.24.b gives ϕ not normalized. We can see in Fig. 1.24 that for $\bar{\sigma} < \bar{\sigma}_{\text{cr}}$, the plasma potential reached $\Delta\phi_{\text{sheath}}$. However, for $\bar{\sigma} > \bar{\sigma}_{\text{cr}}$, the plasma potential do not reaches $\Delta\phi_{\text{sheath}}$, resulting in a non-zero current to the wall. Indeed, the sheath is not monotonic in this case, hence the hypotheses needed to develop Eq. (1.53) are not fulfilled.

In Fig. 1.24.b, we can see that at $\bar{\sigma} \simeq \bar{\sigma}_{\text{cr}}$, the plasma potential tends towards T_e , as mentioned by Eq. (1.57).

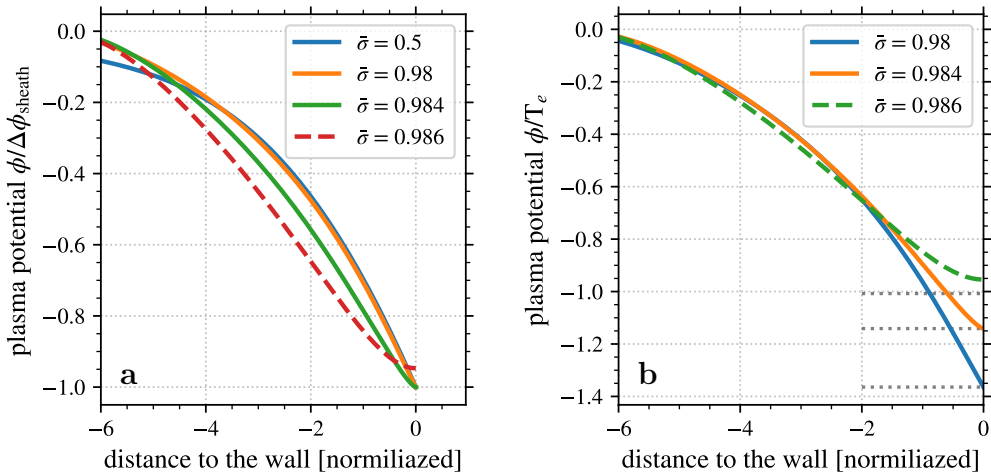


FIGURE 1.24 – Evolution of the plasma potential in the sheath for different values of electron emission rate $\bar{\sigma}$ fro a xenon plasma, (a) normalized by the total potential drop $\Delta\phi_{\text{sheath}}$ from Eq. (1.53), and (b) normalized by the electron temperature, but $\Delta\phi_{\text{sheath}}/T_e$ is noted with the black dotted line.

1.10 Conclusion

In order to study the plasma wall interaction in an HET, we developed a bi-dimensional simulation code using PIC-MCC modeling. As the electrons drift azimuthally due to the $E \times B$ configuration, the ECDI rises, enhancing the cross field transport of the electron toward the anode. The walls closing the chamber in the radial direction are also important for the discharge behaviour. Hence, in order to compare the interaction between these phenomena, we simulate the radial-azimuthal domain.

A special care have been taken during the developement of LPPIC, the 2D-3V PIC-MCC simulation code, concerning

- the modeling of the axial convection, in order to model the energy losses and so attain a steady state,

3. This value of 0.983 is obtained after several approximation, as Eq. (1.56), some of which should not allow to use three significant digits. That's why it does not exactly match with the numerical results presented in Fig. 1.24.



- the modeling of the radial boundary with the dielectric layer included in the simulation domain.

Several theories have also been given in order to better understand the **PIC** simulation results, especially concerning the electron cross-field mobility and the sheath model in presence of electron emission.



Chapitre 2

Parametric study of the dielectric characteristics

We uses the PIC simulation code described in Chapter 1 in order to perform a parametric study over the two aspect of the dielectric walls : the secondary electron emission, and the modification of the electrostatic boundary condition. We observe there impact on the electron cross-field mobility, and the electron temperature. A large discrepancy is observed between the sheath model of Section 1.9 and the PIC simulation results.

Contents

2.1	Simulation parameters	46
2.2	Canonical simulation results	46
2.2.1	Initial phase	46
2.2.2	Stable phase	48
2.2.3	Enhanced electron transport	48
2.3	Modeling the dielectric layer	51
2.3.1	Effect of the dielectric layer	52
2.3.2	Near wall parameters	52
2.3.3	Dielectric model comparison	54
2.4	Effect of electron emission	54
2.4.1	Impact of the electron emission of the mobility	56
2.4.2	Near wall conductivity	57
2.4.3	Three different regimes	57
2.5	Validation of the sheath model	60
2.6	Full dielectric model	62
2.7	Conclusion	63

As introduced in Chapter 1, the HET behaviour is dependent of the axial electron transport toward the anode across the magnetic barrier. Two main phenomena are proposed to enhance the electron mobility,

- the azimuthal instability ECDI
- the electron emission

In order to compare quantitatively the relative importance of the two phenomena, we propose to conduct a parametric study on the dielectric wall characteristics.

As highlighted, the **ECDI** rises due to the $E \times B$ electron drift, but saturate thanks to the axial convection model. Before investigating the time dependent behaviour of the system, we focus in this Chapter 2 on the average values at steady state. The first section describe the parameters of the simulation, while the second section highlight the main characteristics of the simulation result.

2.1 Simulation parameters

The simulation domain corresponds to the exit plan of the thruster. Hence, a neutral pressure P_n of 0.1 mTorr and a plasma density n_e of $1 \times 10^{17} \text{ m}^{-3}$ has been chosen. The fixed axial electric field and radial magnetic field are $E_z = 2 \times 10^4 \text{ m/s}$ and $B_r = 200 \text{ G}$, respectively. The domain measures $L_r = 2 \text{ cm}$ in the radial dimension and $L_\theta = 0.5 \text{ cm}$ in the azimuthal direction. The axial length is fixed at $L_z = 1 \text{ cm}$.

The numerical parameters are chosen to respect the stability criterion of **PIC** simulation, and are presented in Table 2.1

Initialisation

The simulation is initialized with a uniform density of particles, following a Maxwellian distribution for temperature $T_{e,0}$ and $T_{i,0}$ for the electrons and the ions respectively.

2.2 Canonical simulation results

The *canonical* case corresponds to the case when the wall do not include its dielectric mechanism:

- the dielectric layer on the plasma potential
- the electron emission

It is the reference case that will be extensively described and commented. It will be used then to analyse and quantify the effects of the two aspects of the dielectric walls.

2.2.1 Initial phase

The initial phase of the simulation corresponds to the growth of the **ECDI**, and the formation of the sheaths. Because of growth of the instability, the electron transport increases as well, that increases the electron heating.

The time scale of the sheath formation is governed by the ion inertia. It is roughly the same time scale than the saturation of the instability due to ion-trapping.

Figure 2.1 shows the temporal evolution of the electron mean kinetic energy decomposed over the three direction, $\mathcal{E}_{er}, \mathcal{E}_{e\theta}, \mathcal{E}_{ez}$, such that

$$\mathcal{E}_{ed} = \frac{1}{n} \frac{1}{2} m_e \iiint_{\mathbf{v}} v_{e,d}^2 f(\mathbf{v}) d^3 v, \text{ with } d \in \{r, \theta, z\} \quad (2.1)$$

We see that after some high frequency oscillations of $\mathcal{E}_{e\theta}$ and \mathcal{E}_{ez} due to the cyclotron motion, the temperature rises before Stabilizing at $\mathcal{E}_e \simeq 45 \text{ V}$. The radial temperature T_{er} is

TABLE 2.1 – Standard operating and numerical parameters used in the 2D PIC simulations of an HET. The simulation results are given as representative values.

Physical Parameter	notation	Value	Unit
Gas		Xenon	-
Domain dimensions	$L_x \times L_y \times L_z$	$2.0 \times 0.5 \times 1.0$	[cm ³]
Radial magnetic field	B_0	200	[G]
Axial electric field	E_0	2×10^4	[Vm ⁻¹]
Mean plasma density	n_0	3×10^{17}	[m ⁻³]
Initial electron temperature	$T_{e,0}$	5.0	[V]
Initial ion temperature	$T_{i,0}$	0.1	[V]
Secondary electron temperature	T_{see}	1.0	[V]
Neutral gas pressure	P_n	1.0	[mTorr]
Neutral gas temperature	T_n	300	[K]
Neutral gas density	n_g	3.22×10^{19}	[m ⁻³]
Simulation Parameter			
Time step	Δt	4×10^{-12}	[s]
Cell size	$\Delta x = \Delta y = \Delta z$	2×10^{-5}	[m]
Number of particles per cell	N/NG	80	[part/cell]
Simulation result			
Electron temperature	T_e	40	[V]
Electron plasma frequency	ω_{pe}	3.1×10^{10}	[rad/s]
Electron cyclotron frequency	ω_{ce}	3.5×10^9	[rad/s]
Electron Larmor radius	r_{Le}	6×10^{-4}	[m]

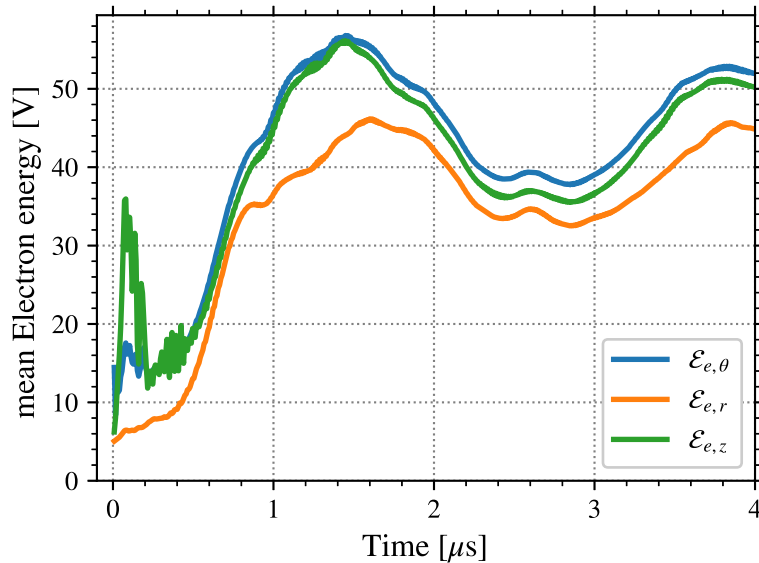


FIGURE 2.1 – Temporal evolution of the electron mean kinetic energy decomposed over the three direction. Is showed only the beginning of the simulation.

less than $T_{e\theta}$ and T_{ez} , but only by a small factor. This means that the electrons temperature is quite anisotropic.

We can see on Figure 2.2 the evolution of the radial profile of the electron density on the plasma potential on the same time scale. We observe of the two parameters the formation of the sheath and the evolution toward a steady state.

2.2.2 Stable phase

After the relatively fast rise of the plasma characteristic, the simulations stabilises at a steady state, as we can see in Figure 2.3.

We observe that after $t \simeq 2\mu\text{s}$, the electron energy \mathcal{E}_e start to oscillate around its final value. The oscillations are than damped and reach their minimum amplitude at $t \simeq 7\mu\text{s}$. Hence, there is no need to simulate for longer than $10\mu\text{s}$ in the following simulations.

Je parle ici d'oscillation. Devrais-je en parler ? Peut-Àtre plus tard ?

Figure 2.4 shows the radial profiles of the electron and ions densities averaged azimuthally at steady state. We can see the sheath close to the wall where the electron density fall rapidly compare to the ions.

2.2.3 Enhanced electron transport

The electron cross-field axial transport is usually characterized by the electron mobility

$$\mu_e = \frac{u_{e,z}}{E_z} \quad (2.2)$$

with $u_{e,z}$ and E_z the electron mean axial velocity and the axial electric field, respectively./

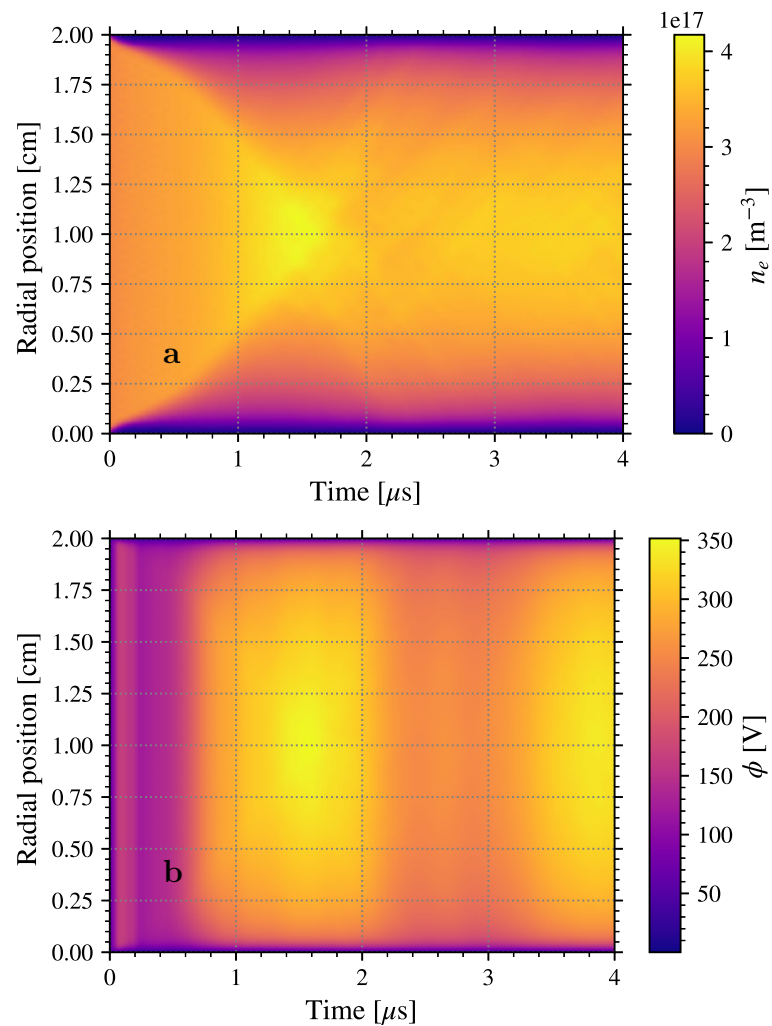


FIGURE 2.2 – Temporal evolution of the radial profile of the (a) electron density and (b) the plasma potential averaged azimuthally

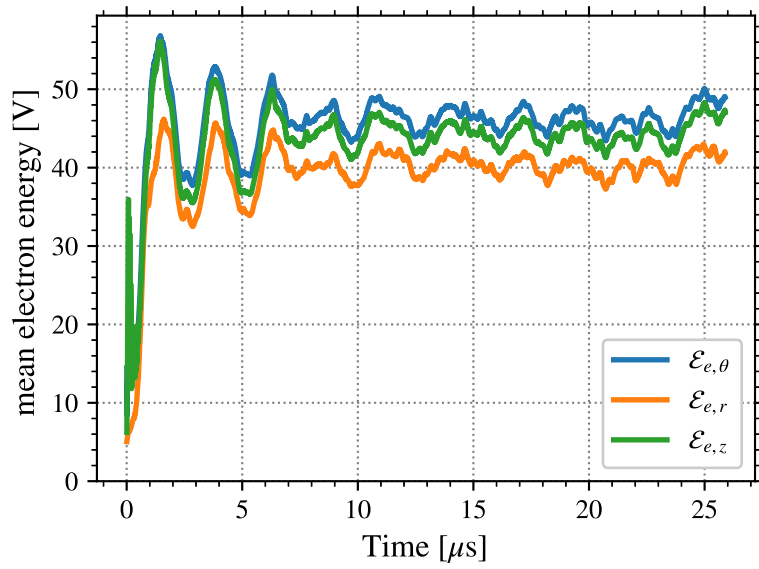


FIGURE 2.3 – Temporal evolution of the electron mean kinetic energy decomposed over the three direction, similar to Fig. 2.1 but during a longer time

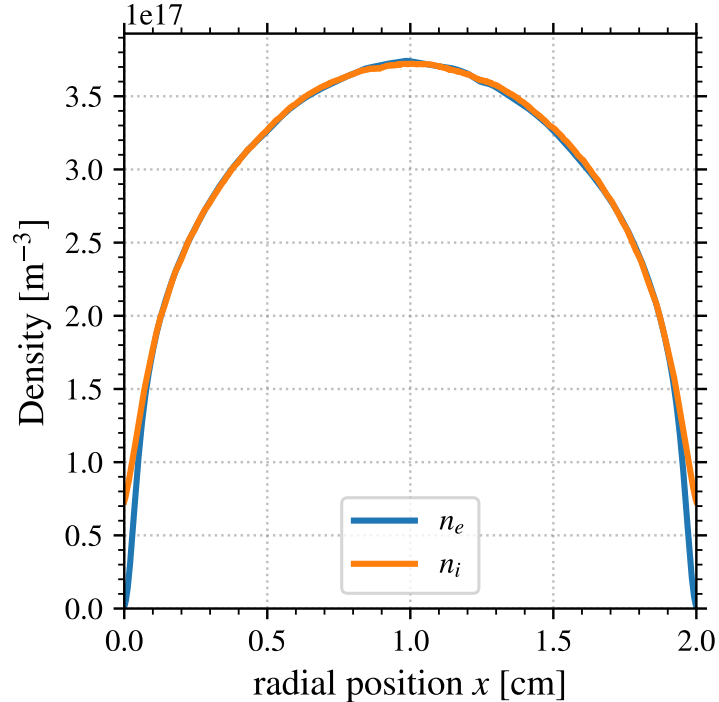


FIGURE 2.4 – Radial profile of the ion and electron densities at steady state, average azimuthally.

In the **PIC** simulations, μ_e is computed at each time step by

$$\mu_{\text{PIC}} = \frac{1}{E_z} \sum_N v_{e,z} \quad (2.3)$$

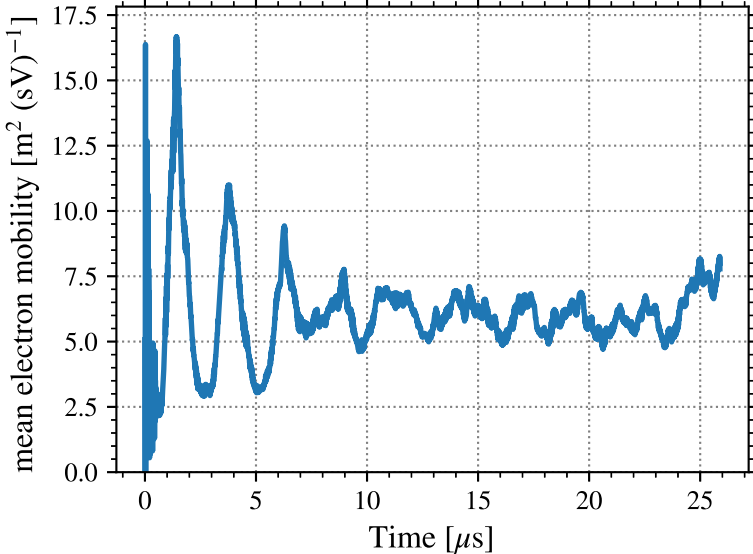


FIGURE 2.5 – Temporal evolution of the electron axial mobility computed in the **PIC** simulation.

Figure 2.5 shows the temporal evolution of the electron mobility μ_{PIC} measured in the simulation. We can see that it presents the same characteristics that the evolution of the electron energy \mathcal{E}_e on Fig. 2.3.

The classical electron mobility from the collisional theory is [24]

$$\mu_{\text{classical}} = \frac{\nu_m \frac{e}{m_e}}{\omega_{ce}^2 + \nu_m^2} \quad (2.4)$$

with ν_m the electron-neutral collision frequency and ω_{ce} is the electron cyclotron frequency. In the conditions of Table 2.1, $\mu_{\text{classical}} \simeq 0.8 \text{ m}^2(\text{sV})^{-1}$.

The measured electron mobility in the **PIC** simulation is one order of magnitude larger than the classical mobility. Is the present case, as no electron is emitted from the wall, the enhancement only comes from the **ECDI**, as proposed by Lafleur et al. [50]. Figure 2.6 illustrates the **ECDI** by showing the azimuthal electric at the center of the channel. We can clearly see the oscillation patterns, of wavelength of the order of 1 mm, as observed in Héron and Adam [38], Janhunen et al. [31] [Other REFs needed!]. The instability is the subject of Chapter 5 [Use REF here], hence it will not be further investigated.

2.3 Modeling the dielectric layer

The first effect of the wall material studied is the layer of dielectric, as introduced in Section 1.5. The simulation parameters are the same as in Section 2.2, but the plasma is separated from the ground wall by a dielectric layer of 3 cm. The relative permittivity of the dielectric is $\epsilon_R = 25$

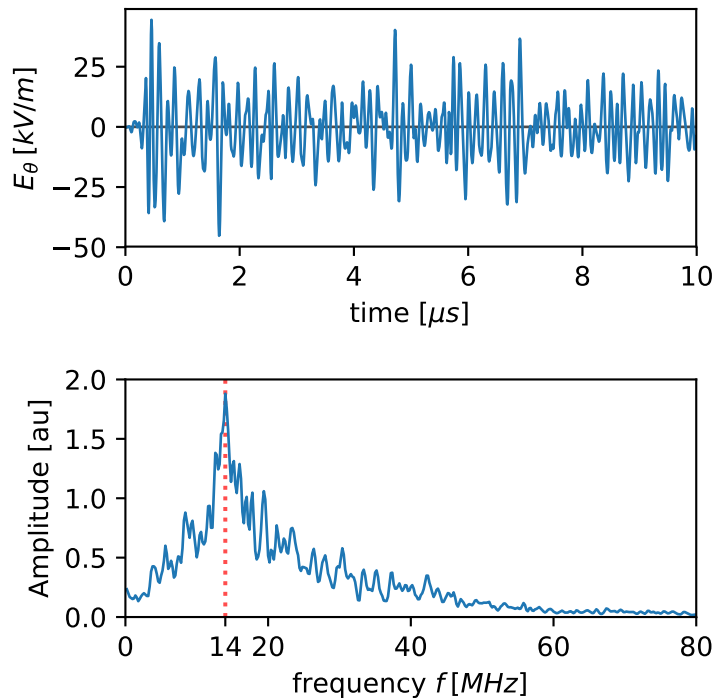


FIGURE 2.6 – Azimuthal instability: temporal evolution of the azimuthal electric field at the center of the simulation, and its frequency spectra

2.3.1 Effect of the dielectric layer

The simulation results presents qualitatively the same results as the case without the dielectric layer. As an example, Figure 2.7 shows the temporal evolution of the axial electron mobility with and without the dielectric layer. We can see a small difference, but not really significant concerning the physical origin of the electron enhanced mobility, and the effect of the dielectric layer. The other variables (mean electron temperature, radial profiles, and so on) follow the same conclusion.

Maybe rerun the cases, or at least check that it has similar parameters than the canonical case

2.3.2 Near wall parameters

Let focus on the surface charge and the near wall electric field. Figure 2.8 shows the temporal evolution of the surface charge at one point of the wall. The position has been chosen to be the center ($L_\theta = 0.25$ cm) of the lower wall, but the observations are similar at other positions.

We can see on Fig. 2.8 that the surface charge oscillates around a mean value close to -4.5 nC/m² and an amplitude of around 1 nC/m².

Est-ce qu'on compare la valeur moyenne à la valeur theo d'un model de gain ?

Ajouter quelque chose dans cette partie ?

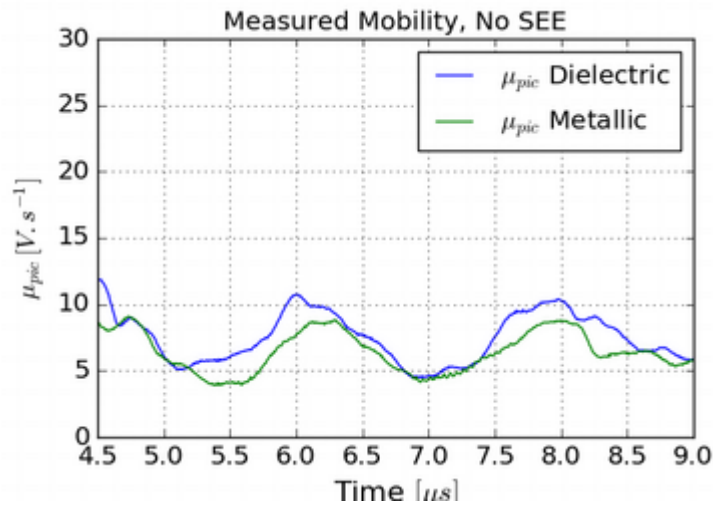


FIGURE 2.7 – Temporal evolution of the axial electron mobility with the dielectric layer and without (ground walls).

[Remake the figure !!](#)

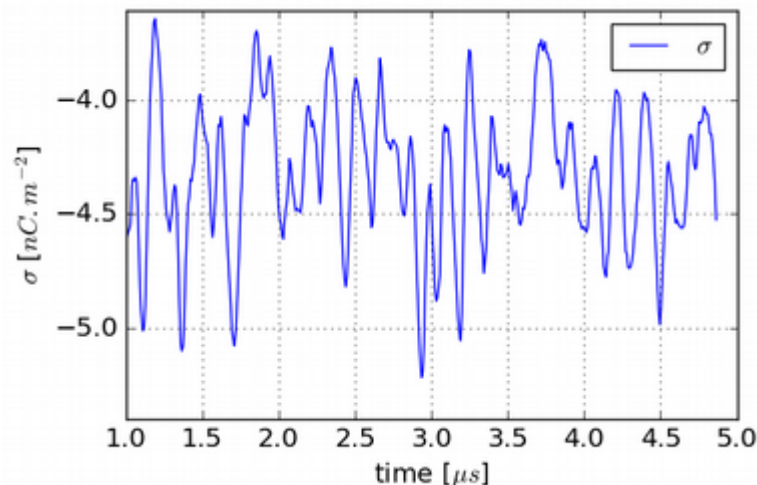


FIGURE 2.8 – Temporal evolution of the surface charges at one position

2.3.3 Dielectric model comparison

As introduced in Section 1.5, another possibility to model the effect of the surface charges on the plasma is to use a Neumann boundary condition [REF]

$$E_r = \frac{\sigma}{\epsilon_0}. \quad (2.5)$$

Equation (2.5) uses two approximations:

- one dimensional
- No electric field in the dielectric

Figure 2.9 shows the radial electric field inside of the dielectric and compare the electric field at the wall and compares it to Eq. (2.5).

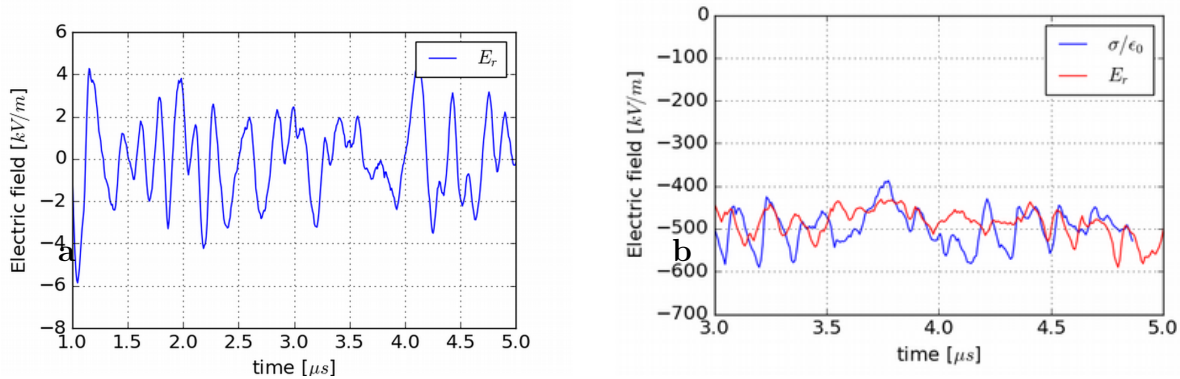


FIGURE 2.9 – Temporal evolution of (a) the radial electric field near the wall at the same azimuthal position than Fig. 2.8, and (b) the comparison with the near wall electric field and Eq. (2.5), using the surface charge of Fig. 2.8.

We can see on Fig. 2.9.a that the electric field in the wall is not zero, but oscillates around a value close to zero (~ 100 V/m). Its amplitude is of the order of 4 kV/m.

Figure 2.9.b shows the near-wall radial electric field compared to Eq. (2.5) at the same position than Fig. 2.8. We can see that the two values are of the same order of magnitude, close to -500 kV/m. However, the two values are not strictly equal, but the maximum error between the two are only of the order of 20%, which mean that the Root Mean Square (RMS) error is around 10%.

2.4 Effect of electron emission

In Section 2.2, the walls were not emissive. However, the dielectric ceramic used in HET can emit electrons [41, 14].

The electron emission model used, introduced in Section 1.7.2, has three parameters $\sigma_0, \epsilon^*, \sigma_{\max}$, such that the emission probability depends as the kinetic energy of the incident electron ϵ as

$$\sigma = \min \left(\sigma_0 + (1 - \sigma_0) \frac{\epsilon}{\epsilon^*}, \sigma_{\max} \right). \quad (2.6)$$

The value of parameters are summarized in Table 2.2. The crossover energy ϵ^* is varied from as low as 4 V, corresponding to a very emissive material, to as high as 200 V, a less emissive material.

TABLE 2.2 – Parameters of the electron emission probability model

Parameter	value
σ_0	0.5
σ_{\max}	2.9
ϵ^*	4 – 200 V

Figure 2.10 shows the electron emission probability for $\epsilon^* = 35.04$ V compared to a Maxwellian Electron Energy Distribution Function (EEDF) of temperature of 45 V. We can see that the saturation of σ at σ_{\max} happens only for the very high energy tail.

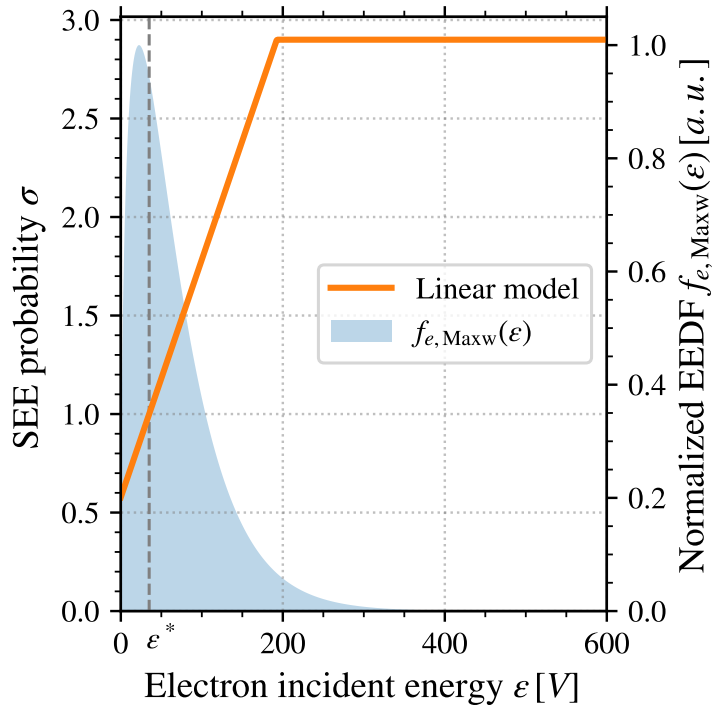


FIGURE 2.10 – Illustration of the electron emission model of Eq. (2.6) compared to a Maxwellian energy distribution function of temperature of 45 V, with $\epsilon^* = 35.04$ V.

In the simulation, we can only measure the average electron emission yield, also named rate,

$$\bar{\sigma} = \frac{\Gamma_{\text{emitted}}}{\Gamma_{\text{incident}}} = \frac{\iiint v_r \sigma(\mathbf{v}) f(\mathbf{v}) d^3 v}{\iiint v_r f(\mathbf{v}) d^3 v}. \quad (2.7)$$

In general, Eq. (2.7) cannot be computed. However, if we suppose that the EEDF is Maxwellian,

Eq. (2.7) can be computed and yields, neglecting the saturation at σ_{\max} ,

$$\bar{\sigma}_{\text{Maxw}}(T_e) = \sigma_0 + (1 - \sigma_0) \frac{2T_e}{\epsilon^*}. \quad (2.8)$$

The saturation at σ_{\max} can be neglected as we have seen that it only affects a small part of the electron population, see Fig. 2.10.

Add the exact calculation and the relative error ?

2.4.1 Impact of the electron emission of the mobility

The effects of the electron emission at the wall on the electron axial mobility is presented in Figure 2.11. Are showed the measured mobility μ_{PIC} , as well as the effective mobility μ_{eff} , the saturation estimate $\mu_{\text{eff}}^{\text{sat}}$ and the classical mobility $\mu_{\text{classical}}$, defined in Section 1.8 respectively by Eq. (1.46), Eq. (1.48), Eq. (1.52) and Eq. (1.47). The values are averaged in time between $t = 5\mu\text{s}$ and $t = 10\mu\text{s}$, and in space over the azimuthal and radial directions.

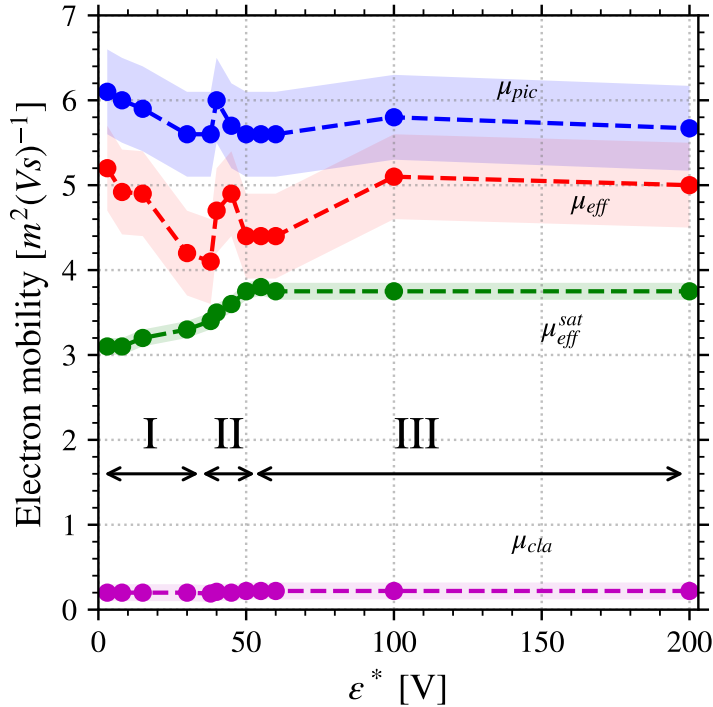


FIGURE 2.11 – Evolution of the electro mobility as a function of the crossover energy ϵ^* . In blue μ_{PIC} is the mobility measured in the simulations, while $\mu_{\text{classical}}$, μ_{eff} and $\mu_{\text{eff}}^{\text{sat}}$ in purple, red and green respectively are calculated with Eqs. (1.46) to (1.48) and (1.52). The three regimes **I**, **II** and **III** are identified.

As expected, the classical mobility in Fig. 2.11 is underestimated by more than one order of magnitude compare to μ_{PIC} . The effective mobility μ_{eff} and the effective mobility at saturation $\mu_{\text{eff}}^{\text{sat}}$ are much closer to μ_{PIC} , with an underestimation of roughly 10% and 30% respectively. The mobility measured in the simulation does not evolve much with the electron emission, even for very high emission rate, i.e very low values of ϵ^* .

On the other hand, $\mu_{\text{eff}}^{\text{sat}}$ decreases slightly when ϵ^* decreases from around 40V to lower values. However, it still provides a reasonable approximation of the electron enhance mobility, even with high electron emission rate.

2.4.2 Near wall conductivity

The information presented in Section 2.4.1 were spatially averaged. However, the mobility coming from the instability is expected to be the higher where the instability is the larger, hence at the center of the channel. On the other hand, the mobility due to wall emission is located close to the wall [51].

Figure 2.12 presents the radial profiles of the mobility measured in the PIC simulations without electron emission and for three values of ϵ^* . Is showed on the left the measured mobility μ_{PIC} and on the right the effective mobility μ_{eff} introduced in Eq. (1.48).

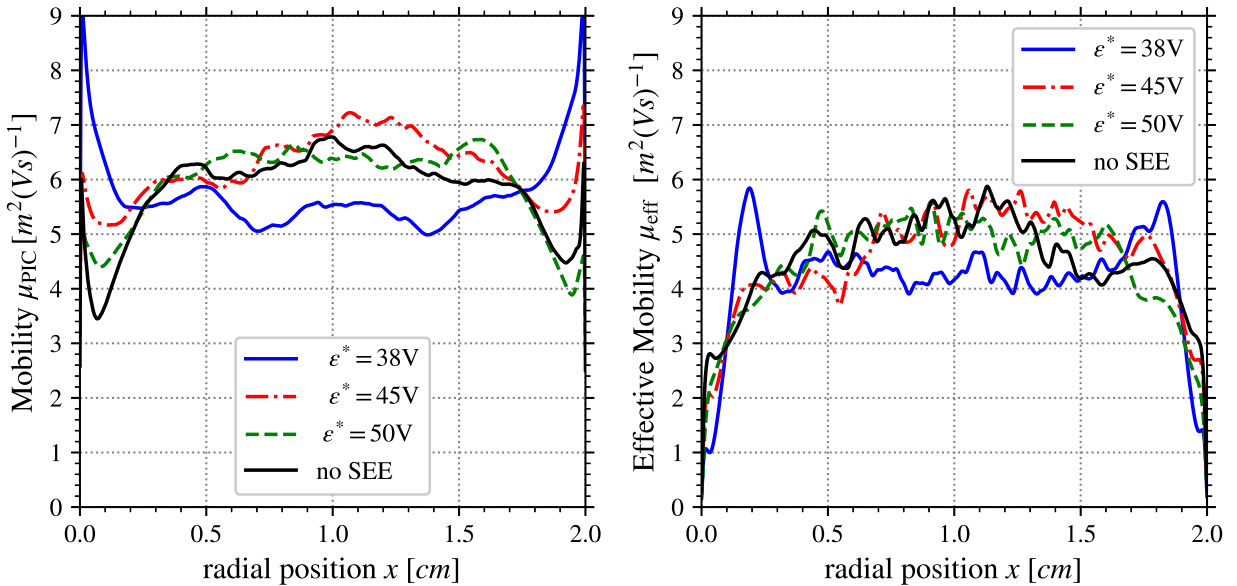


FIGURE 2.12 – Radial profile the electron mobility for different wall emissivity.

We can see in Fig. 2.12 that the mobility measured μ_{PIC} in the center decreases by roughly 20% as the emission rate increases. This observation is in agreement with $\mu_{\text{eff}}^{\text{sat}}$ observed in Figs. 2.11 and 2.12. This is due the electron temperature T_e which decreases from around $T_e = 45V$ at $\epsilon^* = 200V$ to $T_e = 30V$ at low ϵ^* (the evolution of T_e can be seen in Fig. 2.16).

On the other hand, the near wall mobility increases significantly on μ_{PIC} (almost by a factor of 2) with the electron emission. However, we do not see this evolution on $\mu_{\text{eff}}^{\text{sat}}$, meaning that it indeed comes from another physical mechanism that the ECDI.

2.4.3 Three different regimes

In Figure 2.11, three regimes have been identified. Regime I corresponds to low values of ϵ^* (lower than 35V), during which $\mu_{\text{eff}}^{\text{sat}}$ increases with ϵ^* but μ_{PIC} and μ_{eff} decreases. Regime III

corresponds to high values of ϵ^* (higher than 50V), during which $\mu_{\text{eff}}^{\text{sat}}$, and μ_{PIC} are roughly constants, but μ_{eff} increases slightly. Regime **II** is a short transition regime, for $35 < \epsilon^* < 50$ V.

The different regimes easier to differentiate when looking at the temporal evolution of the different variables.

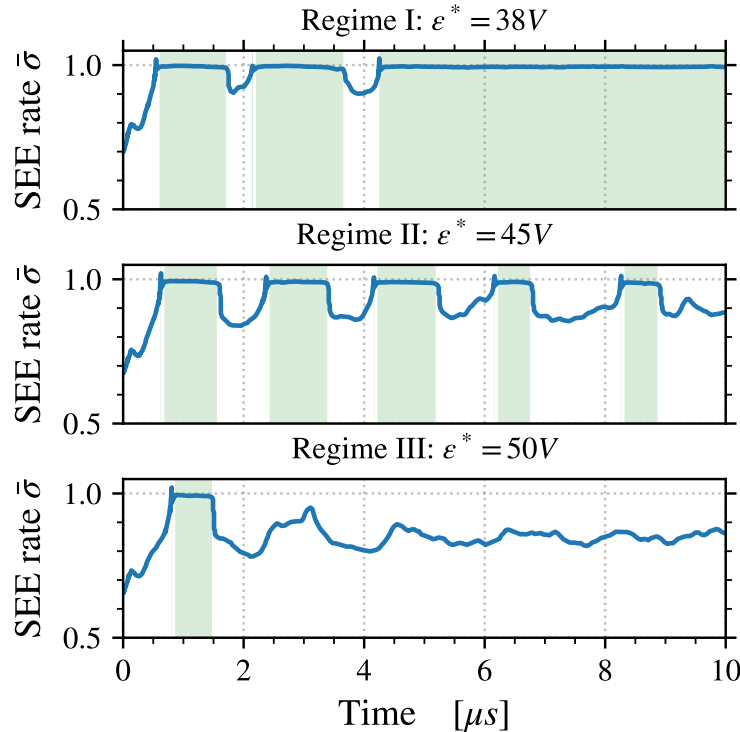


FIGURE 2.13 – Evolution as a function of time of the averaged electron emission rate $\bar{\sigma}_{\text{PIC}}$ in the three regimes observed (two stables, one with oscillations). The light green zones correspond to the periods when $\bar{\sigma}_{\text{PIC}} > \bar{\sigma}_{\text{cr}}$

Figure 2.13 presents the temporal evolution of the space average $\bar{\sigma}_{\text{PIC}}$ for three different values of ϵ^* , corresponding to three different regimes we have identified. In regimes **I** and **III**, $\bar{\sigma}_{\text{PIC}}$ reaches a steady state after a few microseconds.

Regime **I**, with low ϵ^* , is characterized by a saturation of $\bar{\sigma}_{\text{PIC}}$ at a value between $\bar{\sigma}_{\text{cr}}$ and 1, which leads to a non-monotonic potential profile. Regime **III**, for higher ϵ^* , is characterized by a steady state with a SEE rate lower than $\bar{\sigma}_{\text{cr}}$.

The transition between these two stable regimes (monotonic and non-monotonic sheath) passes by regime **II**, an oscillating mode between the two stable regimes. As shown in Fig. 2.11, regime **II** is observed only in a narrow range of ϵ^* . The oscillations of regime **II** are shown in Fig. 2.13 up to 10 μs but have been observed for more than 40 μs . Note that regimes **I** and **III** in Fig. 2.13 are obtained for $\epsilon^* = 38\text{ V}$ and $\epsilon^* = 50\text{ V}$ respectively, i.e. near the boundary of the unstable window (see Fig. 2.11). Consequently, we observe a few oscillations before the steady-state is reached, as these cases are close to the bifurcation.

The physical origin of the bifurcation can be seen with the help of Fig. 2.14, which shows the evolution of the potential drop to the wall as a function of the electron temperature. It is computed using Eq. (2.8) for $\bar{\sigma}$ and Eq. (1.53) on page 42 for the potential drop, which is

summarized as

$$\begin{cases} \bar{\sigma} = \sigma_0 + (1 - \sigma_0) \frac{2T_e}{\epsilon^*} \\ \Delta\phi = T_e \ln \left([1 - \bar{\sigma}] \sqrt{\frac{m_i}{2\pi m_e}} \right) \end{cases} \quad (2.9)$$

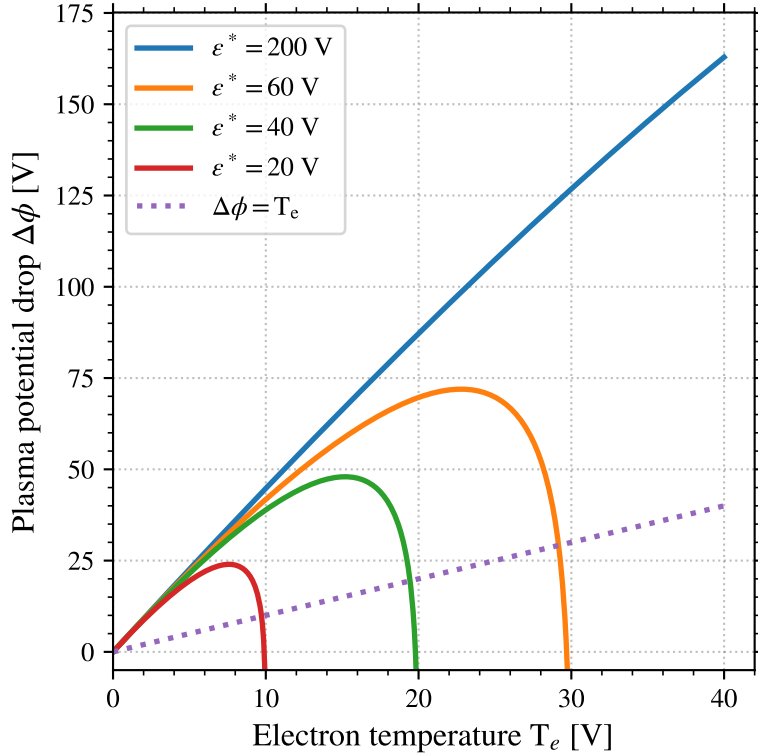


FIGURE 2.14 – Plasma potential drop to the wall as a function of the electron temperature for different values of the cross-over energy ϵ^* using Eq. (2.9). The dashed line is $\Delta\phi = T_e$.

Figure 2.14 shows the evolution of $\Delta\phi$ as a function of T_e obtained with Eq. (2.9) using four different values of ϵ^* . We can see that, starting from low electron temperature, the potential drop increases with the electron temperature, resulting in a better screening of the electrons. This corresponds to regime **III**. However, the $\Delta\phi$ reaches a maximum, after which it drops sharply to zero and below.

When the potential passes the maximum, the electrons are not screen by the sheath any more. Hence, the electrons reach the wall with a higher energy, resulting in a higher electron emission from the wall, hence a smaller potential drop. The sheath is unstable, and quickly attain a SCL [52].

In this regime, the sheath is not monotonic, and the model of Eq. (1.53) on page 42 is no more valid, and the potential drop tends toward $\Delta\phi \simeq T_e$ [46, 49]¹, showed in Fig. 2.14. This corresponds to regime **I**.

During regime **I**, the electron power losses to the wall are very high, and they can exceed the gains. Hence, the electron temperature decreases. If T_e decreases too much, the sheath can come back to the previous regime **III**. The oscillations between regime **I** and **III** defines regimes **II**.

1. see Section 1.9 on page 42 for more details

We have seen in Fig. 2.3 on page 50 that without electron emission, T_e is of the order of 45 V. Using Fig. 2.14, we can expect the observe the transition between regime **III** and **II** for $\epsilon^* \gtrsim 60$ V, as for $\epsilon^* = 60$ V, the maximum of $\Delta\phi$ is at $T_e \sim 25$ V, which is significantly lower than 45 V. The fact that regime **II** appears at $\epsilon^* = 50$ V can be explained because

1. a lower ϵ^* increases the electron losses, hence decreases the electron temperature at equilibrium,
2. the electrons are not Maxwellian.

The first point is confronted in the next section. We can see that the mean electron temperature in the simulation do not evolves a lot with the electron emission for $\bar{\sigma} < 0.8$, correlating to $\epsilon^* > 50$ V. The second point will be studied in section/chapter REF.

2.5 Validation of the sheath model

The PIC simulations used here do not need any sheath model. On the contrary, they can be used in order to validate the sheath modeled introduced in Section 1.9 on page 42 coming from the fluid theory. This sheath model of Eq. (1.53) on page 42 links the plasma potential drop with the electron temperature on the electron emission rate. Equation (2.8) can be used to estimate the electron emission rate given the mean electron temperature measured in the simulations, corresponding statistically to the plasma bulk temperature.

In the PIC simulations, Eq. (2.7) can be computed by counting the number of electrons attaining the wall and emitted during a time-step. We note $\bar{\sigma}_{\text{PIC}}$ this measurement.

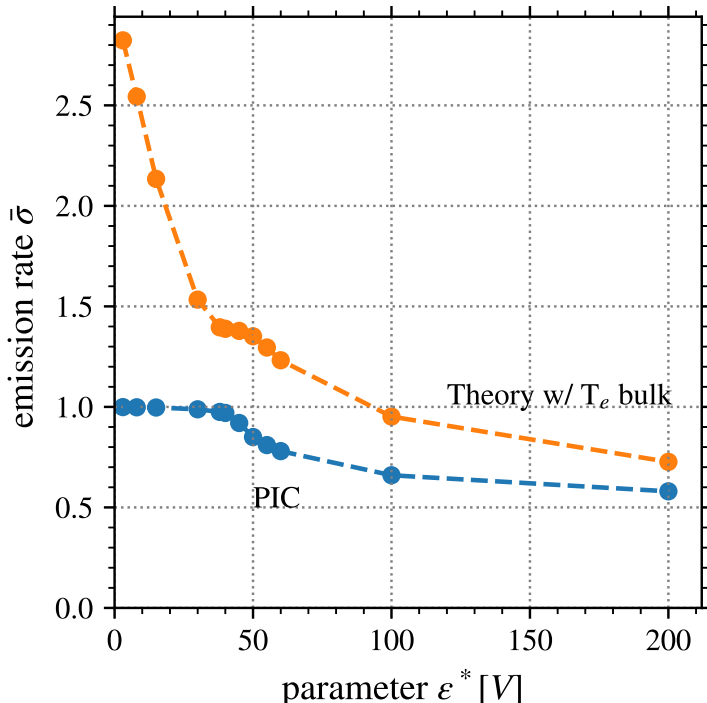


FIGURE 2.15 – Values of the electron emission rate $\bar{\sigma}_{\text{PIC}}$ (blue) measured in the simulation, and $\bar{\sigma}_{\text{Maxw}}$ obtained with Eq. (2.8) using the electron temperature showed in Fig. 2.16.

We can see in Figure 2.15 that the mean electron emission rate lies between 0.6 for large ϵ^* and 1 at low ϵ^* . The saturation of $\bar{\sigma}_{\text{PIC}}$ at 1 for high emissivity ($\epsilon^* < 50V$) was not expected from $\bar{\sigma}_{\text{Maxw}}$. Indeed, σ_{max} is equal to 2.9, and the electron temperature in the bulk measured, when used in Eq. (2.8), predicts a rate between 1.4 and 2.8. This discrepancy at low ϵ^* is due to the **SCL** regime. In Hobbs and Wesson [46], the authors predict that in this regime, a potential well forms such that a fraction of the emitted electrons are returned to the wall, in order to maintain the effective emission rate to $\bar{\sigma}_{\text{cr}} \sim 1$. However, for $c_{\text{rover}} > 50V$, the sheath regime described in Section 1.9 on page 42 should be valid.

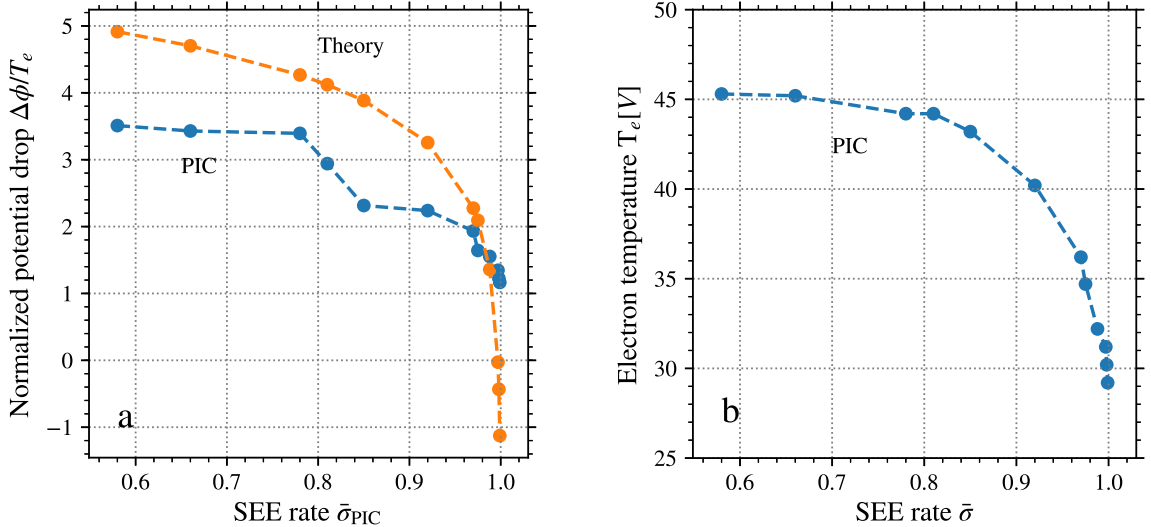


FIGURE 2.16 – (a) Plasma potential drop to the wall normalized by the electron bulk as a function of the electron rate. T_e is italic !; (b) Mean electron temperature measured in the **PIC** simulations as a function of the electron emission rate $\bar{\sigma}$, measured as well in the simulations.

The electron temperature measured in the bulk of the simulation is presented in Fig. 2.16.b for the same cases as in Fig. 2.15. We can see that when $\bar{\sigma}$ increases, T_e monotonically decreases from 45V to around 30V. However, these values are not consistent with the measured emission rate $\bar{\sigma}_{\text{PIC}}$ for $\epsilon^* > 50V$.

Figure 2.16.a shows the evolution of the potential drop to the wall measured in the **PIC** simulation compared to the theory Eq. (1.54) on page 42 (OR is it Eq. (1.53) ... ?). As expected by Eq. (1.57) on page 42, $\Delta\phi$ measured in the simulation saturates to T_e for high emission rate ($\bar{\sigma}_{\text{PIC}} \sim 1$). However, We see that at low emission rate, the potential drop is lower than expected. However, at high emission rate, the expected value tends toward negative values, while the measured values converge toward $\frac{\Delta\phi}{T_e} = 1$.

The sheath model of Section 1.9 used two hypotheses:

- Maxwellian electrons
- Isothermal evolution of the electrons

These two hypotheses will be confronted against the kinetic simulation in the next chapter.

2.6 Full dielectric model

We have observed the effects of the electron emission and the electrostatic boundary condition separately in Section 2.3 and Section 2.4 respectively. In this section, we investigate the interaction between the two phenomena of the dielectric walls.

In Section 2.4, we observed three regimes depending on the emission rate. At high emissivity, the sheath is space-charge limited, resulting in an inverse sheath. At low emissivity, we obtain the standard sheath model with electron emission. The transition between the regimes passes by a oscillating regime.

Section 2.3 showed that when there is no emission, the dielectric boundary condition for the potential do not change the simulation results. Hence, we chose to investigate the interaction when the emission is high. More precisely, the second regime is the most interesting, as it feature a complex behavior.

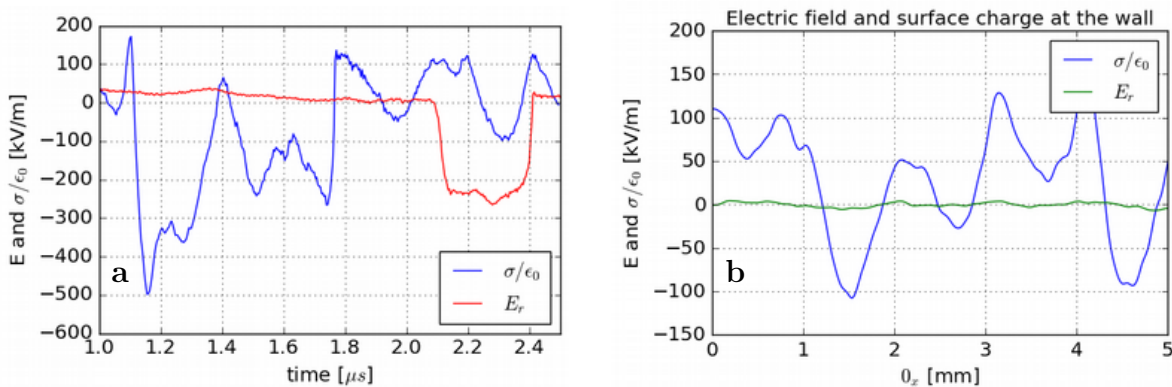


FIGURE 2.17 – Comparison of the (a) temporal and (b) spatial evolution of the radial electric field at the wall compared to the surface charge.

Figure 2.17 shows the (a) temporal and (b) spatial evolution of the radial electric field at the wall compared to the surface charge, similarly to Fig. 2.9.b. We can see that in contrast to the results of Section 2.3, the two values are significantly different. The electric field measured in the simulation is rather uniform and constant, compared to the surface charge.

Moreover, in Fig. 2.17.a, we see that at around $t = 2.1$ s, the electric field sign changes, meaning that the sheath passes from the SCL regime to the normal regime. However, the surface charge is not consistent with this change of regime.

Fig. 2.18 compares the temporal evolution of the mean electron emission rate $\bar{\sigma}_{\text{PIC}}$ for the same parameter $\epsilon^* = 45$ V, with and without the dielectric layer modeled. We see that the oscillations happens for the two models. However, we can observe several differences. The first is the lower level of emission rate. When the wall are grounded, $\bar{\sigma}_{\text{PIC}}$ decreases at around 85%. On the contrary, with the dielectric layer included, the emission rate do not decrease much below 95%. This results in a different overall mean emission rate, that can affect the particle and power balances, hence the mean electron temperature and the performance and the thruster.

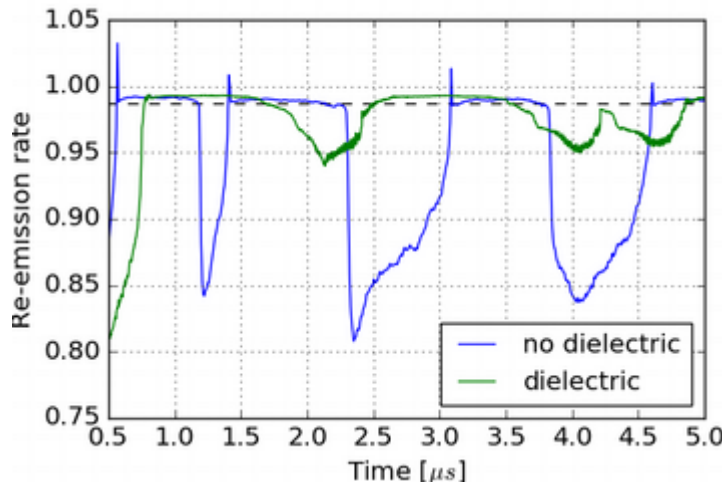


FIGURE 2.18 – Temporal evolution of the mean electron emission rate $\bar{\sigma}_{\text{PIC}}$ for the same parameter $\epsilon^* = 45 \text{ V}$, with and without the dielectric layer modeled.

2.7 Conclusion

Using the **PIC** simulation code introduced in Chapter 1 on page 11, we studied the effects of the dielectric walls on the discharge, and more precisely the effects on the electron cross-field mobility.

To begin with, a *canonical* case, with metallic walls were defined. The metallic walls correspond to grounded, and non-emissive walls. For this reference case, we observed that the convection model used allow us to obtain a steady state. We observed an enhanced electron transport transverse to the magnetic field lines, because of the instability.

Both effects of the dielectric – the electron induced electron emission and the electrostatic boundary condition – were investigated. First, we only modeled the dielectric boundary condition. Then, we studied only the electron emission. Afterwards, the two phenomena have been studied together.

Electrostatic boundary condition

The electrostatic boundary condition were modeled by including in the domain of simulation the thickness of the wall ($L_{\text{wall}} = 3\text{cm}$). Surface charges accumulate at the interface between the plasma and the wall. We observed that the modified boundary condition did not modify significantly the discharge and the axial electron mobility. We saw that the boundary condition used results in a radial electric field E_r of the same order of magnitude than the Neumann boundary condition of Eq. (2.5) on page 54. However, the spatio-temporal evolution are not similar. As the dielectric model used here do not increase significantly the computational time, we recommend to use it instead of the Neumann boundary condition, that do not reproduce the same near-wall behaviour.

Electron induce electron emission

Electron induced electron emission from the wall is modeled using a linear model Section 1.7 on page 38. The crossover energy ϵ^* is varied from a large value (low emissivity material) to small values (high emissivity). We observed in the simulations that when the electron emission rate increases, the mean electron temperature decreases. This decreases the amplitude of the ECDI at saturation, hence decreases the electron mobility in the plasma (see Fig. 2.12 on page 57). However, electron emission induces NWC, which almost double the electron mobility close to the wall when ϵ^* passes from 200V to 30V. Consequently, the overall electron crossfield mobility is almost constant in our simulation.

We observed in our simulation three different regimes depending of the values of ϵ^* . For high values of ϵ^* , the plasma stabilised with an emission rate $\bar{\sigma}_{\text{PIC}} < \text{ratecr}$. When ϵ^* is small, we observe a stable configuration with $\bar{\sigma}_{\text{PIC}} \sim \bar{\sigma}_{\text{cr}}$. Under these conditions, the sheath is space-charge limited. The transition between the two regimes is not stable, but instead passes by a bifurcation regime. During this third regime, the sheath jumps between the two stable regimes. Indeed, the transition passes through an unstable phase, as we can see it on Fig. 2.14 on page 59.

Inconsistent sheath model

The simulation results have been compared to the sheath model of Hobbs and Wesson [46]. We observed a significant discrepancy between the PIC simulations and the sheath model that comes from a fluid approach. In particular, the potential drop and the electron emission rate are both overestimated. These overestimation can lead to erroneous conclusion and prediction when using fluid models. Hence, a better understanding of the plasma-wall transition via the sheath is needed.

The sheath model currently used reposes mainly on two hypothesis

- Maxwellian electrons,
- Isothermal evolution of the electrons in the sheath

Theses hypothesis will be confronted in the next chapter.

Chapitre 3

Anisothermal sheath

In order to explain the discrepancy observed in Chapter 2 between the simulation and the sheath model, we investigate the simulation data. We see that the hypothesis of the sheath model do not stand. Using a simplified 1D PIC simulation, we derive a polytropic closure for the electron. With this new closure equation, we derived a modified sheath model, that fit well the kinetic simulations.

Contents

3.1 Insights for the PIC simulations	66
3.1.1 Electron distribution function	66
3.1.2 Radial evolution of the electron temperature	67
3.2 Simplified 1D for the PIC simulations	69
3.2.1 Description on the simulations	69
3.2.2 Simulation results	70
3.2.3 A model for the EVDF	71
3.3 Collisionless kinetic model and polytropic state law	74
3.3.1 Vlasov equation for the sheath	74
3.3.2 Polytropic state law for the electrons	75
3.3.3 Evolution of the polytropic index	78
3.3.4 Coulomb collision and improvements	79
3.4 Monte Carlo model	79
3.4.1 Description of the Monte Carlo approach	79
3.4.2 Results	81
3.5 Non-isothermal fluid model	83
3.5.1 Comparison with the PIC simulations	84
3.5.2 Modified Bohm criterion	84
3.5.3 Plasma potential drop to the wall	85
3.5.4 Power losses at the wall	87
3.6 Conclusion	89
3.6.1 Realistic heating and ionization	89

Chapter 2 has showed us a discrepancy between the expected plasma-wall interaction quantities – as the plasma potential drop thought the sheath and the electron emission rate – and the PIC simulation results. These discrepancies are expected to explain the difficulties of

the community to model the discharge (see for example Croes [9] section 5.4 and Raitses et al. [25]). Hence, a better understanding of the plasma-wall interaction observed is required.

In this chapter, we come back to the simulation results presented in Chapter 2 in order to gather more insights on the plasma-wall interaction. Then, we develop a simplified simulation in order to isolate the plasma-wall interaction from the rest of the phenomena. This second simulation is unidirectional (1D-3V), un-magnetized, and without electron emission. From this simplified simulation, we derived an anisothermal sheath model, that described well the kinetic simulations. We extend the model to the case where ionization is self-consistent.

3.1 Insights for the PIC simulations

As announced in Section 2.5 on page 60, the sheath model of Section 1.9 on page 42 uses two hypothesis:

- Maxwellian electrons,
- Isothermal evolution of the electrons.

When collisions can be neglected, as it is usually assumed in the sheath, these two hypothesis are linked. Indeed, the 1D Maxwellian distribution function expressed as the total energy is

$$f(\epsilon, \phi) \propto \exp\left(\frac{\epsilon - \phi}{T_e}\right) \propto \exp\left(\frac{\epsilon}{T_e}\right) \exp\left(\frac{-\phi}{T_e}\right), \quad (3.1)$$

where ϵ and T_e are the electron kinetic energy and temperature expressed in Volt. We can see in Eq. (3.1) that the spatial variation (due to the plasma potential ϕ) only affect the amplitude of the distribution function, not its shape in the energy space. Hence, the electron temperature is uniform, i.e. the electrons are isotherm. In addition, we find that $n_e \propto \exp(-\phi/T_e)$, which is the definition of Boltzmann electrons.

Hence, let see if these two hypotheses are respected in the 2D PIC-MCC simulation results

3.1.1 Electron distribution function

Using the kinetic information of the PIC simulations, we present in Figure 3.1 the mean electron energy probability functions (EEPF) in the case $\epsilon^* = 200$ V. Figure 3.1.a shows the projections of the EEPF in the centre of the simulations along the three directions. These projections are compared to the Maxwellian probability function of the same kinetic temperature. Figure 3.1.b shows the total EEPF for both the bulk and the sheath populations. The sheath length is defined as the location where the ions reach the Bohm speed, which is located about 0.4mm from the wall.

We see in Fig. 3.1.a that the electron distribution function is not Maxwellian. In particular the high energy tails are depleted. In order to evaluate the effect of the non Maxwellian EEPF, we numerically integrate the EEPF from the PIC data using Section 1.7 on page 39. The results (not shown) do not differ significantly from the Maxwellian values of Eq. (2.8) on page 56. Hence, we can conclude that even if the Maxwellian hypothesis is not respected in the PIC simulations, it is not enough to explain directly the differences observed in Fig. 2.15 on page 60.

Figure 3.1.b presents the EEPF for the bulk population as well as for the sheath population. We can see that the sheath population is colder than the population at the centre, which could explain the difference of Fig. 2.15 on page 60. This effect is assessed in the next section.

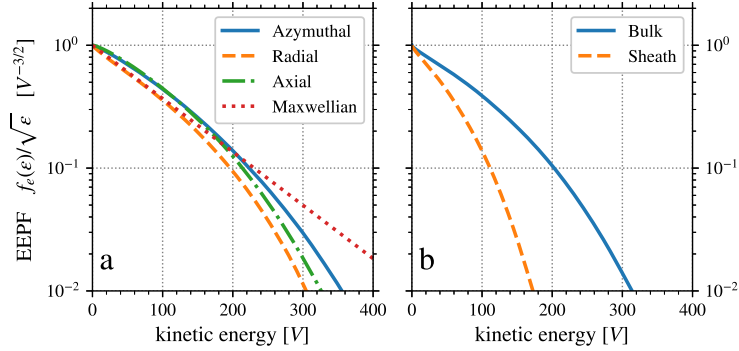


FIGURE 3.1 – Electron energy distribution function of the electrons (a) in the bulk, in the three directions, and (b) in the bulk and in the sheath

Surprisingly, we do not observe in Fig. 3.1 secondary electron beams in the radial direction, unlike previous observations of Sydorenko [26] with a 1D model or Héron and Adam [38] with a 2D model. On the other hand, we do observe SEE beams when we artificially remove the electron cyclotron drift instability by forcing $E_y = 0 \text{ V/m}$ [9]. Hence, it seems that the ECDI, when simulated in 2D, quickly thermalizes the secondary electrons emitted from the walls. In addition, we can see in Fig. 3.1.a that the radial EEPF is close to the EEPF in the other directions, i.e. the electrons are almost isotropic. For instance, for $\epsilon^* = 200 \text{ V}$ we measure $T_{er} = 41.5 \text{ V}$ while $T_{e\theta} \sim T_{ez} = 49 \text{ V}$. The cause of the difference with Héron and Adam [38] is not yet clear, but there the results were only obtained at early times where saturation of the instability has not necessarily been reached, and no electron loss in the axial direction was accounted for. This is supported by Figs. 2.1 and 2.3 which show us that there is a larger anisotropy at the beginning of the simulation ($t < 2\mu\text{s}$) than later. It is possible that at steady state, the electrons in our simulations have had sufficient time to become more isotropic. The energy transfer from the axial and azimuthal directions to the radial direction is not clearly understood yet [31], but we believe that it is due to the instability.

3.1.2 Radial evolution of the electron temperature

We compute the temperature in the **PIC** simulations using the kinetic definition

$$T = \frac{3}{2}m \langle (v - \langle v \rangle)^2 \rangle = \frac{3}{2}m(\langle v^2 \rangle - \langle v \rangle^2),$$

which the averaging performed over the distribution function, hence

$$T = \frac{3}{2} \frac{1}{n} \iiint_{\mathbf{v}} |\mathbf{v} - \mathbf{u}|^2 f(\mathbf{v}) d^3 v \quad (3.2)$$

with T in Joule, and we have the relation with T in Volt

$$T = \frac{k_b T}{e}.$$

Figure 3.2 shows the radial profile of the electron temperature T_e averaged in time over $5\mu\text{s}$ and over the azimuthal direction, for different emissivity. We can see that for all of the values

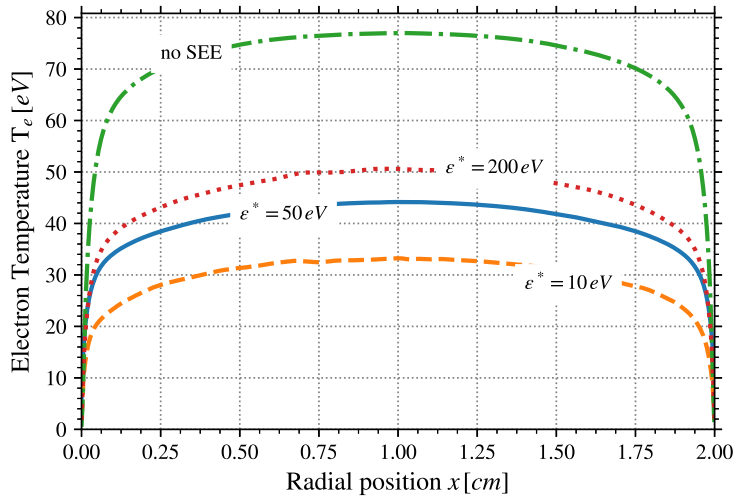


FIGURE 3.2 – Radial profiles of the electron temperature measured in the PIC simulations, without secondary electron emission (label "no SEE") and with different values of ϵ^* .

Problem with value for No SEE and Figs. 2.1 and 2.3

of ϵ^* and even without electron emission, there is a steep gradient of the electron temperature in the sheath. Actually, the profile of T_e is very similar to the profile of the plasma potential ϕ .

The significant difference between the value of the average electron temperature in the whole simulation domain, used before in Section 2.5 on page 60, and the electron temperature close to the wall can be responsible to the over estimation of $\bar{\sigma}$ compared to $\bar{\sigma}_{\text{PIC}}$. Using this information, we compute an estimation of the electron emission rate $\bar{\sigma}$ with Eq. (2.8) on page 56 using the electron temperature close to the wall. The results are presented in Figure 3.3.

We observe in Fig. 3.3 that now, the electron emission rate is well predicted (error less than 5%), except for $\epsilon^* = 10 \text{ V}$ where a large error is still observed. As previously discussed, the case $\epsilon^* = 10 \text{ V}$ presents a very high SEE rate which leads to a potential well close to the wall. Consequently, some secondary electrons emitted at low energy would be reflected back to the wall. Hence, since Eq. (2.8) does not take into account this local effect, it is not surprising that the SEE rate calculated using the mean electron temperature in the sheath is too high.

To summarise, Fig. 3.3 shows that when the sheath potential profile is monotonic, the SEE rate can be well predicted by Eq. (2.8) using the electron temperature close to the wall, which is lower than in the centre of the domain. The particle and energy flux inducing the SEE rate is not well described if we use the electron temperature of the bulk as in the isothermal sheath model. This explains the overestimations of both $\bar{\sigma}$ and $\Delta\phi$ presented in Figs. 2.15 and 2.16. Hence, the isothermal hypothesis used in the sheath model of Section 1.9 is denied by the PIC simulations.

In the next sections, we use a simplified PIC simulation to isolate the origin of the electron temperature gradient.

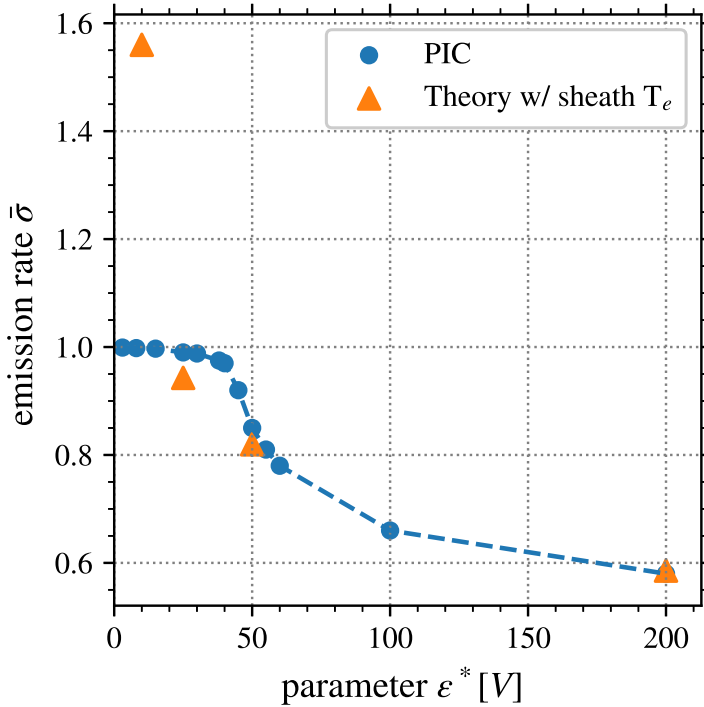


FIGURE 3.3 – Estimation of the electron emission rate $\bar{\sigma}$ as a function of ϵ^* using the values of the electron temperature close to the wall.

3.2 Simplified 1D for the PIC simulations

We have seen in Section 3.1 that the secondary electron emission is not responsible for the temperature gradient. Hence, we will neglect it in this section. The simulations were at low pressure, in which case the electrons are non-local [53, 54]. In low pressure bounded discharges, it is well-known that the EEDF is not Maxwellian in both capacitively coupled plasmas and inductively coupled plasmas [55, 56, 57, 39], in agreement with Fig. 3.1 on page 67.

The impact of non-Maxwellian EEDF on the electron flux at the wall has been studied by Kaganovich et al. [58, 59]. They showed that the electron kinetics at low pressure can significantly reduce the electron flux to the wall, in agreement with kinetic simulations. The main parameter determining the electron flux was found to be the electron scattering frequency. However, to the knowledge of the authors no model describes the sheath with non-Maxwellian EEDF, that could be used in fluid equations.

The evolution of the electron temperature and the non-locality of the electron in bounded plasmas as been studied in Meige and Boswell [57]. Hence, we will use in this chapter similar physical conditions, in order to compare with there conclusions.

3.2.1 Description on the simulations

We use a 1D PIC simulation of an argon plasma confined between two walls separated by a length $L = 10\text{cm}$. The background pressure is varied between 0.05 and 10 mTorr. The direction of the simulation is x , and y, z are perpendicular to the simulation domain.

Parameter	Value	Unit
Pressure P	0.05, 0.1, 0.5, 2, 10	mTorr
Initial density	1.10^{15}	m^{-3}
$T_{e,inj}$	5	V
Domain length L gas	10 Argon	cm -

TABLE 3.1 – Simulation parameters for the 1D PIC simulations.

The same particle source model as in **2DPIC** of the **HET** is used. In order to compensate the particle losses at the wall, we inject with a spatially uniform probability an electron-ion couple for every ion lost at the wall. This corresponds to the following ionization rate :

$$S_{iz} = \frac{1}{L} 2\Gamma_e \quad (3.3)$$

with Γ_e the electron flux to the wall. A second model will be used later, with a self-consistent heating and ionization.

Monte Carlo collisions (MCC) are still used, but we do not model the particle generation of the ionization process, but only the scattering and momentum transfer. As previously, Coulomb collisions are not included in the study as we are at low plasma density (at the steady state the electron density is around $n_e = 10^{15} \text{ m}^{-3}$).

To satisfy generally accepted accuracy conditions for the cell size and time step [60], a time step of $3.7 \cdot 10^{-11} \text{ s}$ is used with a cell length of $1.7 \cdot 10^{-5} \text{ m}$. This allows us to resolve properly the plasma frequency $\frac{2\pi}{\omega_{pe}} = 3.5 \cdot 10^{-9} \text{ s}$ and the Debye length $\lambda_{De} = 3.10^{-4} \text{ m}$. Around 300 particles per cell are used for the simulations, and statistical convergence has been verified for both the cell length and the number of particles per cell.

3.2.2 Simulation results

Figure 3.4 shows the results of the simulation with the parameters of Table 3.1, and a neutral pressure $P = 0.1 \text{ mTorr}$. On the left-hand side we observe the electron and ion density profiles, while on the right the plasma potential and the electron temperature are shown. In Fig. 3.4, the electron and ion densities and the plasma potential feature the usual symmetric profiles with a pre-sheath and a sheath. However, while the electron temperature is almost constant in the plasma bulk at the center of the simulation domain, we observe a steep decrease in the sheath. The electron temperature gradient should affect the density profile in the sheath and the electron heat flux at the wall.

For isotropic distribution functions, it is convenient to introduce the electron energy distribution function (EEDF) f_ϵ [61] :

$$f_\epsilon(\epsilon)d\epsilon = 4\pi v^2 f_e(\mathbf{v})dv \quad (3.4)$$

It is related to the electron energy probability function (EEPF) f_P by

$$f_P(\epsilon) = \epsilon^{-1/2} f_\epsilon \quad (3.5)$$

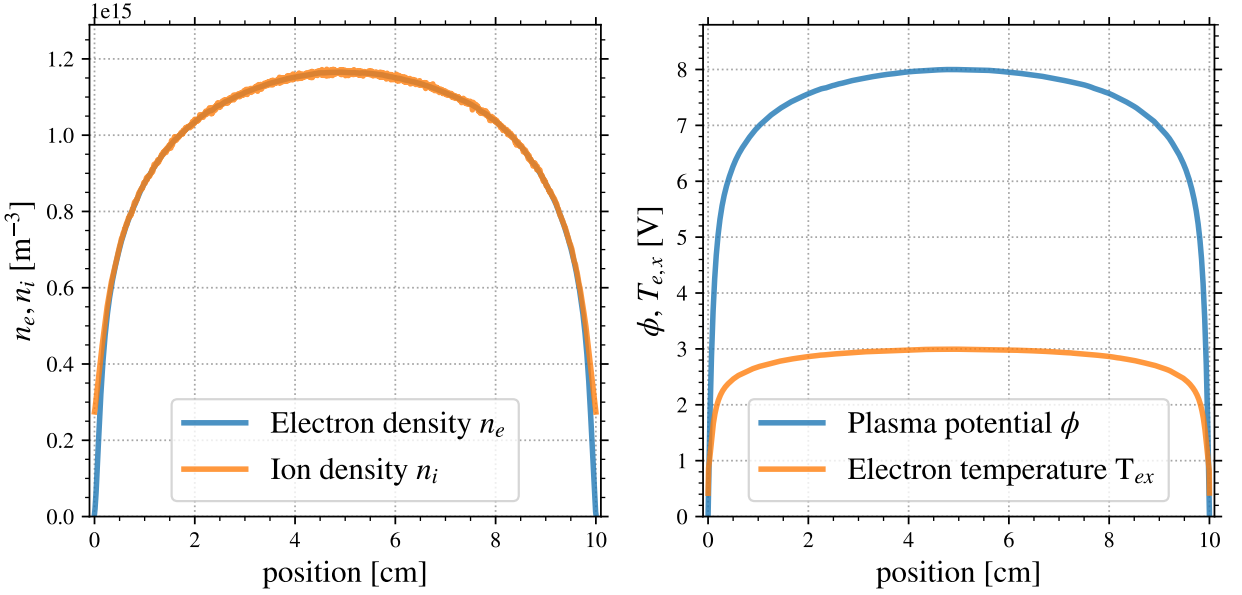


FIGURE 3.4 – Profile of the electron and ion densities (left) and the plasma potential and electron temperature in the PIC simulation with the parameters of Table 3.1, with $P = 0.1\text{mTorr}$.

As the distribution function is anisotropic, and since the direction of interest is the x direction, we focus here on $f_{Px}(\epsilon_x)$ the EEPF in the x direction, with $\epsilon_x = \frac{m_e v_{e,x}^2}{2}$.

Figure 3.5 presents the EEPF measured in the PIC simulations at different positions. As the system is symmetric, the positions have been chosen arbitrarily on the left sheath, and their values correspond to the positions of the cell centres. We can see that the low energy population ($\epsilon < e\Delta\phi$) is nearly Maxwellian, of temperature $T_e = 5\text{ V}$ which is the injection temperature $T_{e,inj}$. This population corresponds to the electrons confined by the sheath. However, the high energy tail ($\epsilon > e\Delta\phi$) is depleted due to the absorption at the wall [57, 59, 62]. This results in a non-Maxwellian EEPF of temperature, defined with Eq. (3.2), lower than $T_{e,inj}$. The small population of electrons with very high energy corresponds to the electrons newly generated that have not yet reached the walls.

3.2.3 A model for the EVDF

In order to describe the EEPF seen in Fig. 3.5, it is possible to use a two- T_e distribution [62, 55, 63] :

$$f_{Px}(\epsilon_x) = A\epsilon_x^{1/2} \begin{cases} \exp(-\frac{\epsilon_x}{T_1} - \frac{\epsilon_b}{T_2}), & \epsilon_x < \epsilon_b \\ \exp(-\frac{\epsilon_x}{T_2} - \frac{\epsilon_b}{T_1}), & \epsilon_x > \epsilon_b \end{cases} \quad (3.6)$$

with ϵ_b the energy of the knee, T_1 and T_2 the two temperatures, and A a normalization constant. In the case of absorption by the walls, we can assume that $\epsilon_b = \Delta\phi$ as the absorption only occurs for the electrons of energy higher than $\Delta\phi$. For the case of Fig. 3.5, we find $T_1 = 5\text{eV}$ and $T_2 = 0.5\text{eV}$. This model is closer to the PIC EEPF, but neglects the tails of newly generated electrons of high temperature, as we can see if in Figure 3.6

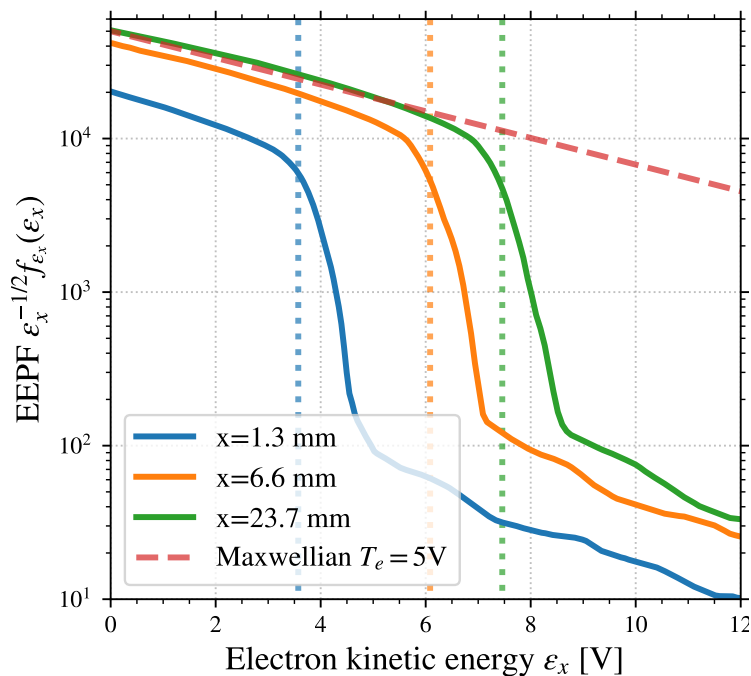


FIGURE 3.5 – Electron energy probability function at different positions in the simulation : at $x = 1.3, 6.6$ and 23.7 mm in blue, orange and green respectively. Also shown are the Maxwellian distribution of temperature $T_e = 5$ V (red dashed line), as well as the local plasma potential relative to the wall $\Delta\phi$ (dotted lines).

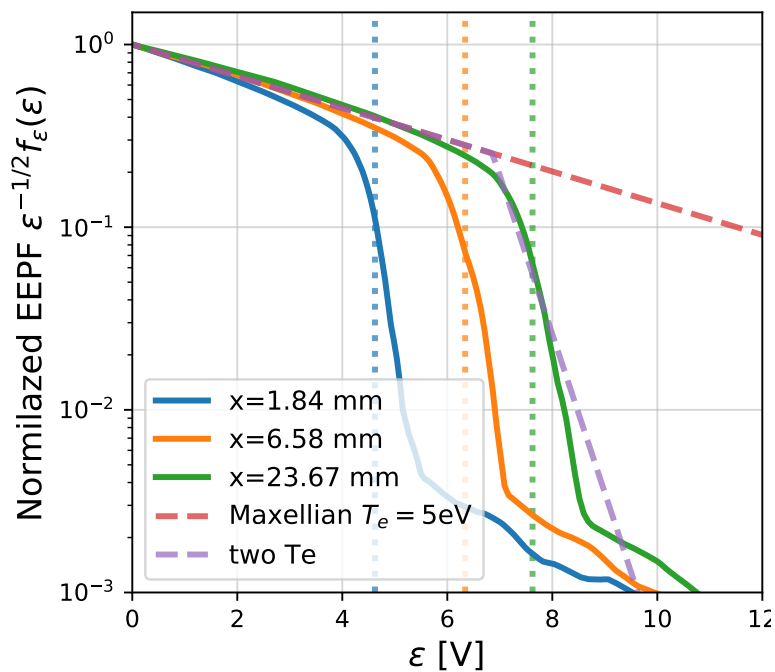


FIGURE 3.6 – Electron energy probability function at different positions in the simulation, as in Fig. 3.5, but overlaid with a Two temperature fit.

The Fit do not fix the knee at ϕ ! Need to be done again.

In the next section, we investigate a way of taking into account this non-local kinetic phenomenon in a fluid model.

3.3 Collisionless kinetic model and polytropic state law

The previous section showed that the electrons are not Maxwellian, similarly to the 2D results. In this section, we use the 1D kinetic equation in order to highlight the important phenomena needed to describe the sheath.

3.3.1 Vlasov equation for the sheath

Because the sheath is thin and the neutral pressure is low, we neglect the collisions in the sheath, so that we only need to solve Vlasov's equation. The stationary 1D-3V Vlasov equation for the EVDF reads:

$$v_x \cdot \partial_x f_e \mathbf{e}_x + \frac{e}{m_e} \nabla \phi \cdot \nabla_v f_e = 0, \quad (3.7)$$

Since the electrostatic potential depends only on x , Eq. (3.7) becomes,

$$v_x \partial_x f_e + \frac{e}{m_e} \partial_x \phi \partial_{v_x} f_e = 0 \quad (3.8)$$

The variables v_y and v_z do not play any role, such that they can be hold constant, and we can solve Eq. (3.8) with f_e as a function of x and v_x only.

In order to solve Eq. (3.8) in the sheath, we use the following boundary conditions:

- At the plasma sheath boundary ($x = x_s$) the EEDF is imposed:

$$f_e(x_s, v_x) = f_0(v_x), \quad (3.9)$$

- At the wall ($x = x_w$) the particles are absorbed, such that

$$f(x_w, v_x < 0) = 0 \quad (3.10)$$

The partial derivative equation (3.8) can be solved by the method of the characteristics. We introduce the function $\gamma(x)$ such that

$$\frac{df_e(x, \gamma(x))}{dx} = \partial_x f_e + \gamma' \partial_{v_x} f_e = 0 \quad (3.11)$$

Combining this equation with Eq. (3.8) for $v_x = \gamma(x)$,

$$\left(\frac{e\phi'}{m_e} - \gamma\gamma' \right) \partial_{v_x} f_e = 0 \quad (3.12)$$

In general $\partial_{v_x} f_e \neq 0$ such that $(e\phi'/m_e - \gamma\gamma')$ can be integrated

$$\frac{\gamma(x)^2}{2} - \frac{e\phi(x)}{m_e} = \frac{\gamma(x_s)^2}{2} - \frac{e\phi_s}{m_e} \quad (3.13)$$

Since the EVDF is conserved along the contour γ ,

$$f_e(x, \gamma(x)) = f_e(x_s, \gamma(x_s)) \quad (3.14)$$

and

$$\gamma(x_s) = \left[\gamma(x)^2 - \frac{2e(\phi(x) - \phi_s)}{m_e} \right]^{1/2} \quad (3.15)$$

with ϕ_s the plasma potential at the sheath edge. Using Eq. (3.9),

$$f_e(x, v) = f_0 \left(\left[v^2 - \frac{2e(\phi(x) - \phi_s)}{m_e} \right]^{1/2} \right) \quad (3.16)$$

Condition (3.10) yields a condition on f_0 :

$$\text{for all } v > \left(\frac{2e\phi_s}{m_e} \right)^{1/2}, f_0(v) = 0 \quad (3.17)$$

This simple collisionless model explains rigorously how the tail of the EVDF is cut by the wall absorption. This asymmetry of the EVDF could press us to separate the electrons into the one going toward the wall and the one going away from the wall. Figure 3.7 shows the EEPF of the electron going toward and from the wall. We can see that there only is a small difference between the EEPF of the two populations. Indeed, as the domain is symmetric and bounded in the two directions, the population coming toward the wall is also depleted by the opposite wall. Hence in the following, we will neglect this asymmetry due to the wall.

Figure 3.8 compares the EEPF from Eq. (3.16) with the PIC simulation between the position $x = 1.3$ mm and $x = 23.7$ mm. The plasma potential reads $\phi(x = 1.3 \text{ mm}) = 4.1 \text{ V}$ and $\phi(x = 23.7 \text{ mm}) = 7.7 \text{ V}$. We can observe a very good agreement between the actual evolution of the EEPF measured in the simulations and the prediction of Eq. (3.16). This confirms the possibility to neglect the collisions in the sheath.

3.3.2 Polytropic state law for the electrons

The evolution of a two-T_e EEDF in a collisionless potential drop has been studied by Zhang et al. [63]. The authors have shown that the evolution of the electron population can be described using a polytropic index γ , such that:

$$\nabla_x (p_{e,x}(x) n_e(x)^{-\gamma}) = 0 \quad (3.18)$$

with $p_{e,x}$ the electron pressure. The value of γ is related to the two temperatures T_1 and T_2 , and for $T_1 > T_2$, we have $\gamma > 1$.

Figure 3.9 shows the PIC simulation results presented in Fig. 3.4 in log scale. Each marker represents one cell of the PIC simulation. Overlaid is a linear regression which slope is the polytropic index γ . The regression is conducted over the whole simulation domain. We can see that the linear regression fits the simulation results with a very good agreement ($R^2 = 0.999$). The value $\gamma = 1.43$ is significantly higher than the isothermal case ($\gamma_{\text{isothermal}} = 1$). Interestingly, while the polytropic law observed in Zhang et al. [63] was only for a collisionless

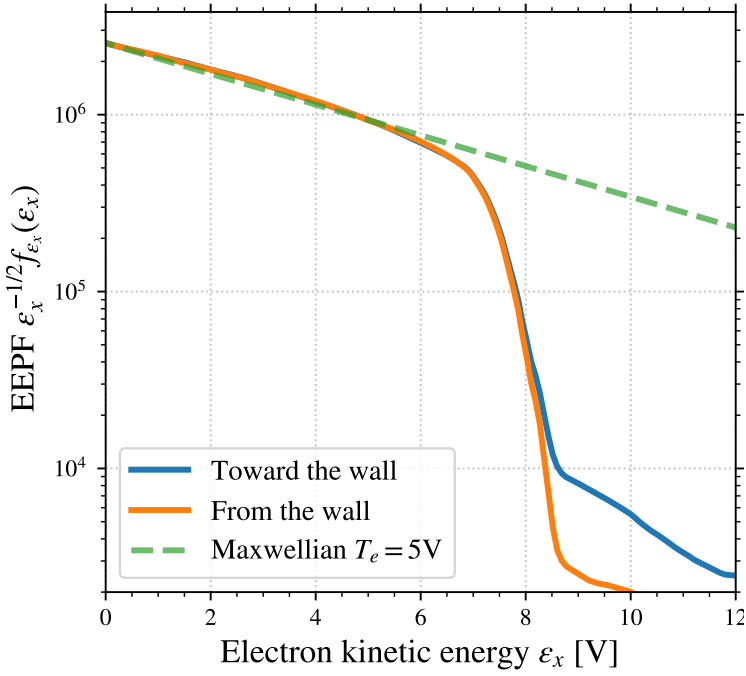


FIGURE 3.7 – EEPF measured in the PIC simulations of the electrons going toward and from the wall at $x = 23.7\text{mm}$. The green dashed line corresponds to a Maxwellian distribution of 5 V.

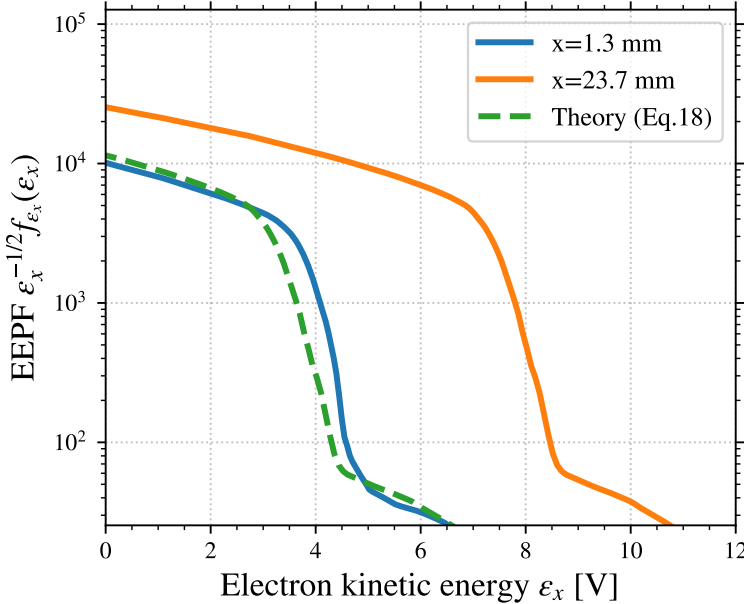


FIGURE 3.8 – Evolution of the EEPF between 1.3mm (in blue) and 23.7mm (in orange) from the wall. Is overlaid (in dashed green) the expected EEPF at $x = 1.3\text{mm}$ using the EEPF at $x = 23.7\text{mm}$ and the potential difference in Eq. (3.16).

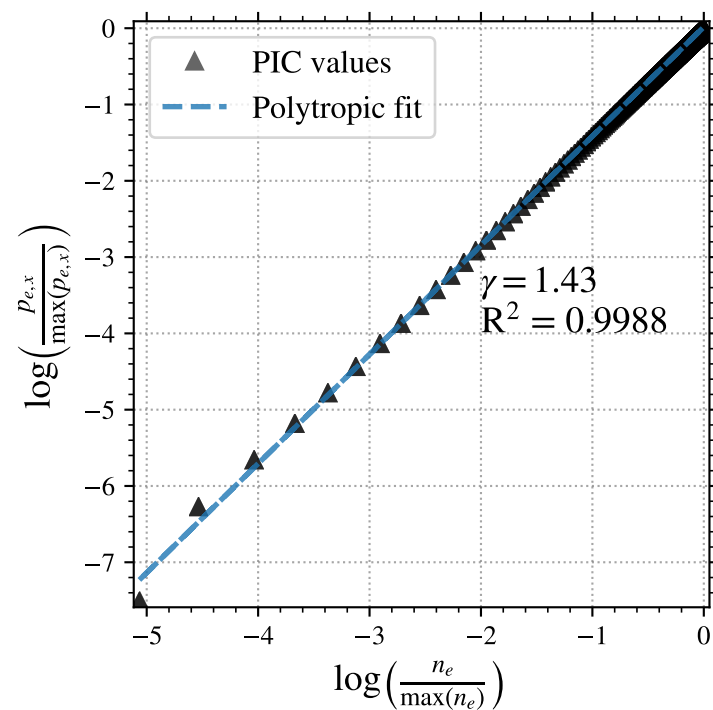


FIGURE 3.9 – Electron pressure as a function of the electron density observed in the PIC simulations of Fig. 3.4 (black markers), and the linear fit (blue dotted line) in order to determine γ .

evolution, here the polytropic law is observed in both the collisionless sheath and the modestly collisional plasma region.

The polytropic law of Eq. (3.18) can be used in order to close the fluid equation without the isothermal hypothesis. The non-isothermal fluid model for the sheath is the subject of the next section. A polytropic index for the ions has already been proposed in order to link the ions kinetics and the fluid parameters [64, 65]. The approach here is essentially the same but applied to the electrons.

3.3.3 Evolution of the polytropic index

We investigate the effect of the neutral pressure on the polytropic index γ . We recall that the electron elastic scattering and momentum transfer are modeled, while the ionization and the heating are not self-consistent, but they are similar to the **2D PIC** models of Chapter 2. Figure 3.10 presents the evolution of γ as a function of the pressure. We can see that the polytropic index decreases from 1.7 to 1.4 as the pressure increases from 0.05 to 10 mTorr. This is in agreement with the fact that the high energy electron population is mostly replenished by the electron-neutral scattering [59]. Increasing the collisions while keeping the other parameters constant provides more electrons to the high energy tail, hence reducing the polytropic index [63].

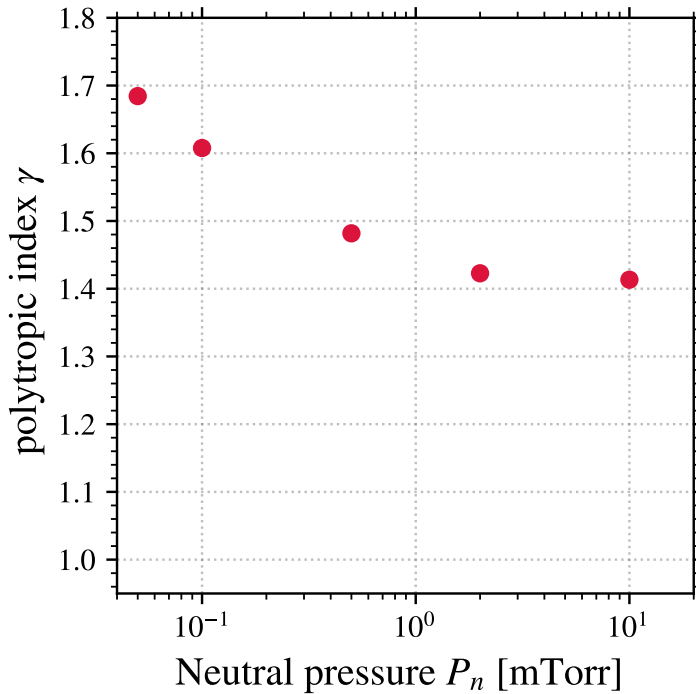


FIGURE 3.10 – Effect of the background neutral pressure over the polytropic index γ in the PIC simulations using **M1**. As a reminder, the isothermal case corresponds to $\gamma = 1$.

Other parameters are also expected to modify γ . For instance the size of the simulation, the electron mean energy, and the nature of the gas.

3.3.4 Coulomb collision and improvements

- compare the order of magnitude of coulom collision and the others
- Discuss about the thermalization model of Krooks (or something like that)

3.4 Monte Carlo model

Even though the **1D PIC** simulations were computed faster than the **2D** simulations, they still took too long when compared to the fluid model. We have seen that the the polytropic index depends on several conditions, as the background pressure (see Fig. 3.10) but also the densities, sizes, heating mechanism, and so on.

Before studying the possibility to derive an analytic law for γ , we try a Monte Carlo approach. A possible application would be similar to Kushner [66], where the author uses a small population of electrons (typically 300-500) and observes their evolutions in a given plasma potential.

This method gets rid of the Poisson equation, which can take between 30% and 50% of the total simulation time. Hence, the Debye length does not have to be highly resolved any more for stability and numerical heating. However, we still need to resolve the sheath, which length is of the order of 5 Debye length [67]. Consequently, a coarser mesh of cell size 5 times larger can be used. The condition on the time step is also reduced. This results in a much faster computation.

3.4.1 Description of the Monte Carlo approach

In order to validate the Monte Carlo approach, we use the converged simulation of the **1D PIC** model. We uses the potential, so the electric field, computed self-consistently in the **PIC** simulation. The Monte Carlo is initialised with a uniform density of electrons. When an electron is collected at the wall, it is re-injected, similarly to the **PIC** simulation.

The electron are pushed, and undergo collisions as described in Section 1.2.

We validate the Monte Carlo computation by comparing the electron density, temperature and distribution function. Figure 3.11 shows the expected EEPF obtained in the **PIC** simulation with a background pressure of $P = 1 \text{ mTorr}$. The maximum plasma potential, at the center of the domain, is $\max(\phi) = 12.2 \text{ V}$.

Time scales

The electron collected at the wall have a kinetic at least equal to the potential drop to the wall $\epsilon = e\Delta\phi$, which corresponds in our case to a limit velocity of $v_{\lim} = 1.5 \times 10^6 \text{ m/s}$. Hence, the limit time of flight between the two boundaries is

$$T_{\text{flight}} = \frac{L}{v_{\lim}} = 0.068 \mu\text{s}$$

The electron-neutral scattering frequency is computed for a background pressure of $P = 100 \text{ mTorr}$ at the temperature of 300 K, which corresponds to a neutral density of $n_g = 3.2 \times 10^{21}/\text{m}^3$.

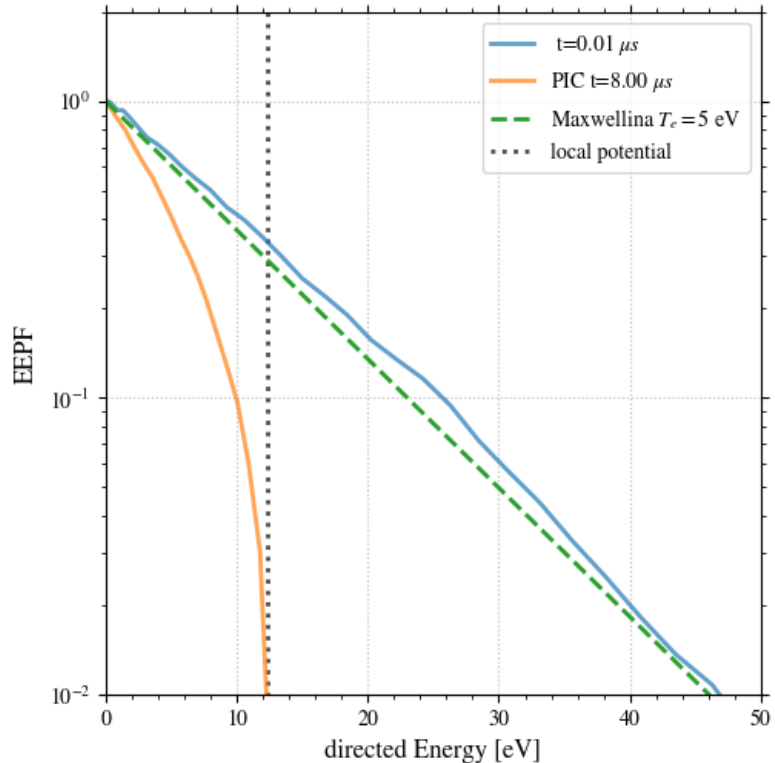


FIGURE 3.11 – Electron energy probability function obtained from (orange) the PIC simulation after convergence, and (blue) at the beginning of the Monte Carlo. Is overlaid the local plasma potential.

For an electron temperature of 5 V, the thermal electron-neutral elastic scattering frequency is

$$\nu_{\text{ela}} = 205 \text{ MHz}.$$

However, at this high energy, electron-neutral scattering is not isotropic, but instead gives mostly small angles (forward scattering) [32]. Hence, a large number of collision is required. The resulting time scale corresponding of the electron-neutral scattering is of the order of

$$T_{\text{ela}} = 0.4 \mu\text{s}$$

Here, $1/\nu$ is 0.004, I don't know why it is that high, when the simulations takes much more time to thermalise

Numerical artefacts

In PIC simulations, numerical parameters can induce numerical heating and thermalization [68]. The numerical heating has been studied in detail [36]. It is due to aliasing effects, and depends of the grid size, time step and number of particles per cell. The choice of these parameter leads to reduce the effect of the heating.

The thermalization is the fact that the distribution of the particle tends toward a Maxwellian. It originates from fluctuations of the electric field due to the discretization of the particle. The first studied showed that the thermalization time τ_T depends on N_D the number of particle per Debye sphere [69, 70]. The presence of collision can affect τ_T [71, 68]. In Turner [71], the author observed the evolution of the thermalization time with N_D as

$$\tau_T = \frac{1}{\omega_{pe}} \frac{34.4}{N_D^{-2} + 28.0 N_D^{-1} \frac{\nu_m}{\omega_{pe}}} \quad (3.19)$$

which gives in our condition a time-scale several order of magnitude larger than the previous. Hence, the effects of numerical parameters on the kinetics informations of the simulation are expected to be negligible.

3.4.2 Results

We measured the electron energy distribution function (EEDF) at 3 cm from the wall. Figure 3.12 shows the evolution of the EEDF at the very early moments of the simulation. The energy of the electron is oriented, meaning that the electron with positive energy are comming from the wall, while the negative energy is used for the electrons going toward the wall.

Two phenomena wan be can see in Fig. 3.12. The first is the rapid decrease of the tail of the distribution function, for energies higher than the plasma potential. The tail for positive energy descreses faster than for negative energy, as the EEPF is measured closer to one wall than the other ($x = 3$ cm against $L - x = 7$ cm). As expected, after $T_{\text{flight}} \simeq 0.07 \mu\text{s}$ the two tails are largely depleted, as they are one order of magnitude smaller than the Maxwellian EEPF.

The second phenomena is presence of waves in the velocity space that can be seen in the low energy populations. They are due to the plasma potential profiles. Indeed, the electrons are initialized with a uniform temperature, but their total energy depends on the local plasma potential.

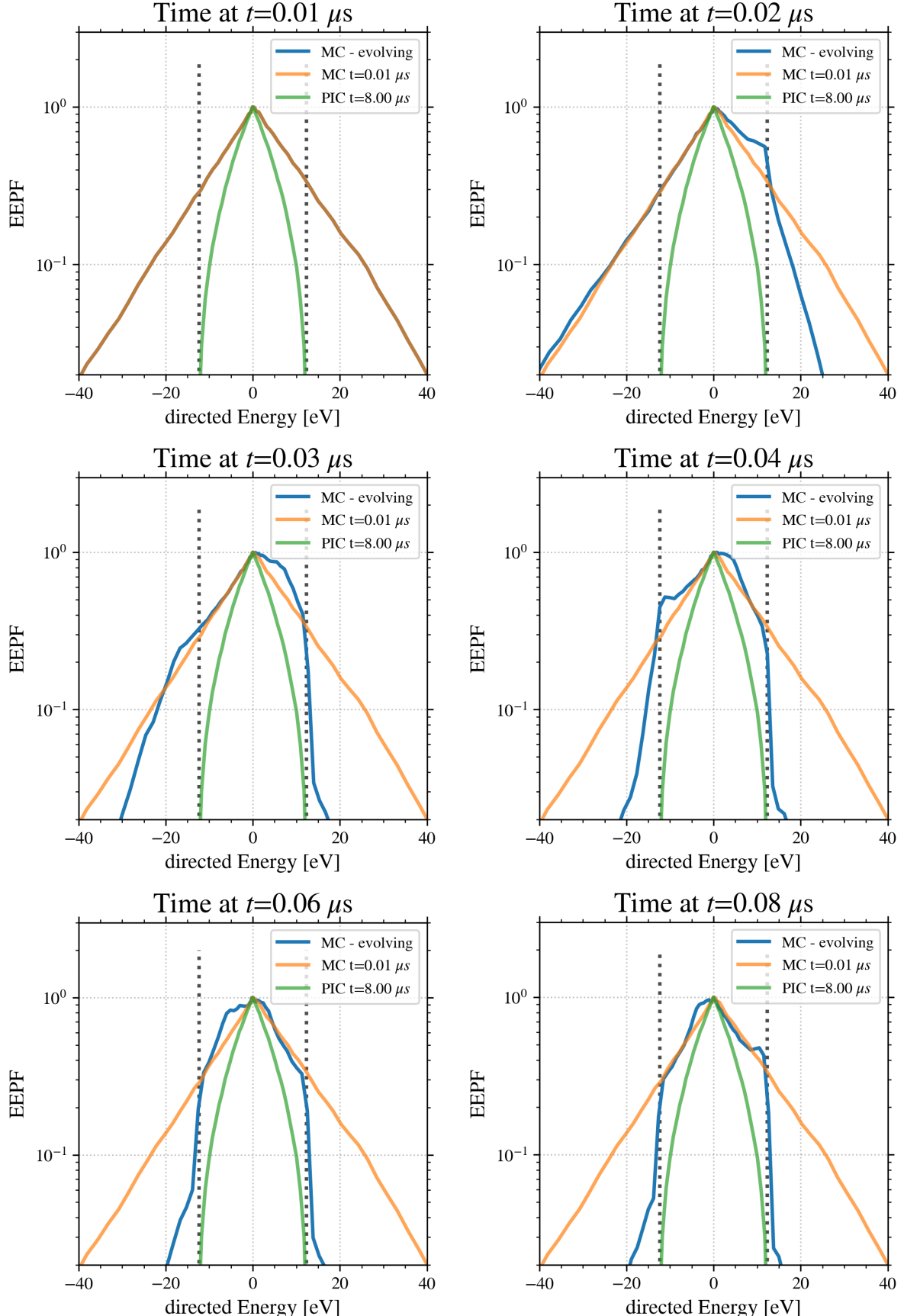


FIGURE 3.12 – Evolution of the directed EEPF measured at $x = 3$ cm from a wall. The positive energy is used for the electron going from the wall, while the negative energy represent the electrons moving toward the wall. The dotted line correspond to the local potential. Are overlaid (orange) the initial Maxwellian distribution and (green) the EEPF obtained at the end of the **PIC** simulation.

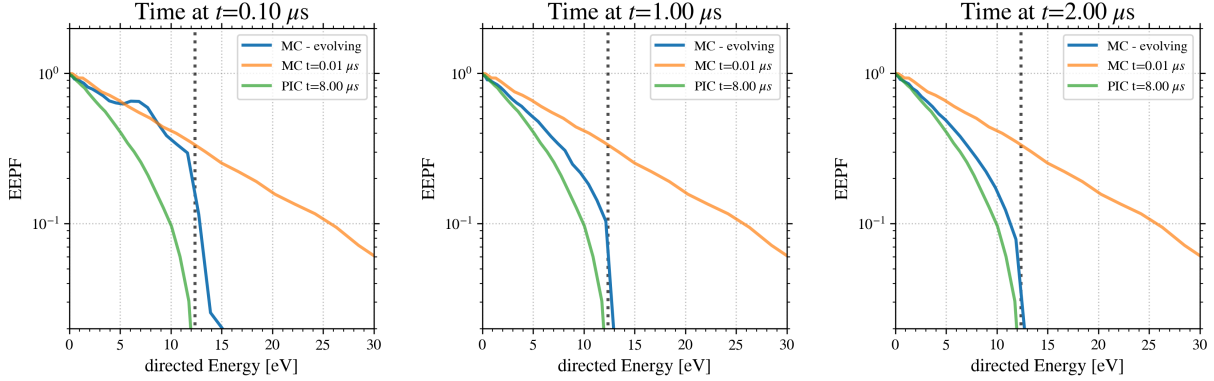


FIGURE 3.13 – Evolution of the directed EEPF measured at $x = 3\text{ cm}$ from a wall. The dotted line correspond to the local potential. Are overlaid (orange) the initial Maxwellian distribution and (green) the EEPF obtained at the end of the **PIC** simulation.

Figure 3.13 shows the evolution of the EEDF over a longer time scale compared to Fig. 3.12. We can see the slow evolution of the low energy population from the initial, but slightly perturbed, Maxwellian distribution toward a distribution of smaller temperature. After $t = 2\text{ }\mu\text{s}$, the EEPF of the Monte Carlo computation is fairly close to the **PIC** EEPF. This is significantly longer than the estimated time scale of the elastic collisions $T_{\text{ela}} = 0.4\text{ }\mu\text{s}$.

This Monte Carlo investigation showed us that in the **1D** model, the EEPF depends on the absorption at the wall but also the electron-neutral collisions. The final shape of the distribution is not simple, and is difficult to described and predict analitically. However, given the potential profile, the Monte Carlo computation reproduces the same distribution in a much shorter time compared to the **PIC** simulation. The obtained EEPF can then be used to determine the electron density and temperature evolution. This could be used to determine efficiently, and precisely, the electron polytropic coefficient.

3.5 Non-isothermal fluid model

We have seen in Section 3.3 that the polytropic law presented in Eq. (3.18) can be used to describe the evolution of the electron temperature, hence closing the fluid equations. Provided that the electron pressure is $p_e = n_e T_e$, assuming the sheath collisionless, and neglecting the electron mean velocity compared to the thermal velocity, the electron momentum conservation

$$\nabla(n_e T_e) + n_e \nabla \phi = 0 \quad (3.20)$$

results in

$$\nabla T_e = -\frac{\gamma - 1}{\gamma} \nabla \phi \quad (3.21)$$

Integrating Eq. (3.20) from the sheath edge, the electron density is hence :

$$n_e(\phi) = n_0 \left[1 + \frac{(\gamma - 1)(\phi - \phi_0)}{\gamma T_{e0}} \right]^{\frac{1}{\gamma-1}} \quad (3.22)$$

with the subscript 0 corresponds to the sheath edge. In Eq. (3.22), we need to have γ strictly greater than one. For $\gamma = 1$, we find the usual Boltzmann electrons :

$$n_e(\phi) = n_0 \exp\left(-\frac{(\phi - \phi_0)}{T_e}\right) \quad (3.23)$$

corresponding to the usual isothermal model.

3.5.1 Comparison with the PIC simulations

The PIC simulations of Section 3.2 can be modeled using a 1D low pressure fluid model with collisionless ions. We use the solver described in Riemann et al. [72], modified to take into account the new electron closure. We simply need to add one equation for the temperature, and the ionization source term is fixed constant in space.

Using the normalized variables and parameters :

$$\lambda = \frac{S_{iz}L}{c_s}, \quad \Phi = -\frac{e\phi}{T_{e,c}}, \quad u = \frac{v_i}{c_s} \quad (3.24)$$

$$n = \frac{n_i}{n_{e,c}}, \quad \chi = \lambda \frac{x}{L}, \quad \epsilon = \lambda \frac{\lambda_{De}}{L} \quad (3.25)$$

$$(3.26)$$

with $T_{e,c}, n_{e,c}$ the electron temperature and density at the center, $c_s = \sqrt{\frac{T_{e,c}}{m_i}}$ the ion sound speed, v_i, n_i the ion speed and density, and S_{iz} the ionization frequency, we can write the set of equations representing the plasma as[72] :

$$\begin{cases} d_\chi(nu) &= \lambda \\ d_\chi(u) &= \frac{d_\chi(\phi)}{u} - \frac{\lambda}{n} \\ d_\chi^2(\Phi) &= \frac{(n-n_e)}{\epsilon^2} \\ S_{iz} &= cst \\ n_e &= \left[1 + \frac{(\gamma-1)\Phi}{\gamma}\right]^{\frac{1}{\gamma-1}} \end{cases} \quad (3.27)$$

Starting from the center, and using the results of the PIC simulations to determine γ , we can use the system of Eq. (3.27) to compute the profile of every variable. The plasma potential is self consistently computed from an arbitrary value at the center. It is then shifted to set the wall potential to 0V. The integration uses the 4th order Runge-Kutta integration scheme of the python package **scipy**.

Figure 3.14 shows the comparison of the electron temperature and the plasma potential with the resolution of the set of Eq. (3.27). We can see a very good agreement between the model and the PIC simulations.

3.5.2 Modified Bohm criterion

The Bohm criterion expresses a necessary condition on the ion velocity at the sheath edge for the formation of a stationary sheath [73]. As discussed in the appendix, it is possible to

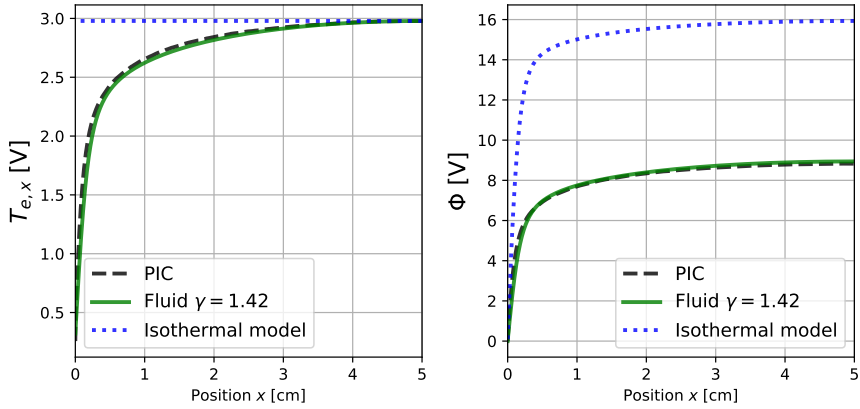


FIGURE 3.14 – Comparison of the electron temperature and plasma potential measured in the PIC simulation with the prediction of the polytropic model with $\gamma = 1.42$.

derive a modified Bohm criterion for the polytropic electrons :

$$\mathcal{M}^2 = \left(\frac{u_0}{c_s} \right)^2 \geq \gamma \quad (3.28)$$

with \mathcal{M} the Mach number, u_0 the ion mean velocity at the sheath edge and $c_s = \left(\frac{eT_{e0}}{m_i} \right)^{1/2}$ the ion acoustic velocity at the sheath edge. The derivation of this modified Bohm criterion is analogous to the isothermal case. In the same way as for the isothermal Debye sheath, we assume that the sheath criterion is saturated :

$$\mathcal{M}^2 = \gamma. \quad (3.29)$$

In addition, the ion flux at the wall is equal to the flux at the sheath edge :

$$\Gamma_i = n_0 \sqrt{\frac{\gamma e T_{e0}}{m_i}} \quad (3.30)$$

3.5.3 Plasma potential drop to the wall

The electron flux at the wall is the thermal flux :

$$\Gamma_e = \int_0^{+\infty} v f_e(x = x_w, v) dv \quad (3.31)$$

Using the model of two-Te EEDF described in 3.2.3, we obtain

$$\Gamma_e = \frac{1}{4} n_{e,w} \bar{v}_w \quad (3.32)$$

with $n_{e,w}$ the electron density at the wall, and $\bar{v}_w = \sqrt{\frac{8eT_{e,w}}{\pi m_e}}$ the mean electron speed at the wall, using $T_{e,w}$ the electron temperature at the wall. Using Eq. (3.21), we have :

$$T_{e,w} = T_{e0} \left(1 - \frac{\gamma - 1}{\gamma} \frac{\Delta\phi_0}{T_{e0}} \right) \quad (3.33)$$

with $\Delta\phi_0$ the potential drop between the sheath edge and the wall. Using the current equality : $\Gamma_i = \Gamma_e$ at the wall we find with Eqs. (3.30), (3.32) and (3.33) :

$$\left[1 + \frac{\gamma - 1}{\gamma} \frac{\Delta\phi_0}{T_{e0}} \right]^{\frac{1}{\gamma-1}} \sqrt{1 - \frac{\gamma - 1}{\gamma} \frac{\Delta\phi_0}{T_{e0}}} = \sqrt{\frac{4\gamma\pi m_e}{m_i}} \quad (3.34)$$

Equation (3.34) cannot be solved analytically, but it can be solved numerically. We use the function `fsolve` from python package `scipy.optimize` to plot the solution of Eq. (3.34) in Fig. 3.15. Meanwhile, we estimate $\frac{\Delta\phi_0}{T_{e0}}$ using the fluid model of Section 3.5 by reading the potential at the position for which the ions reach the modified Bohm velocity. The small difference between the solution of Eq. (3.34) and the fluid solution is due to the presence of ionization in the sheath.

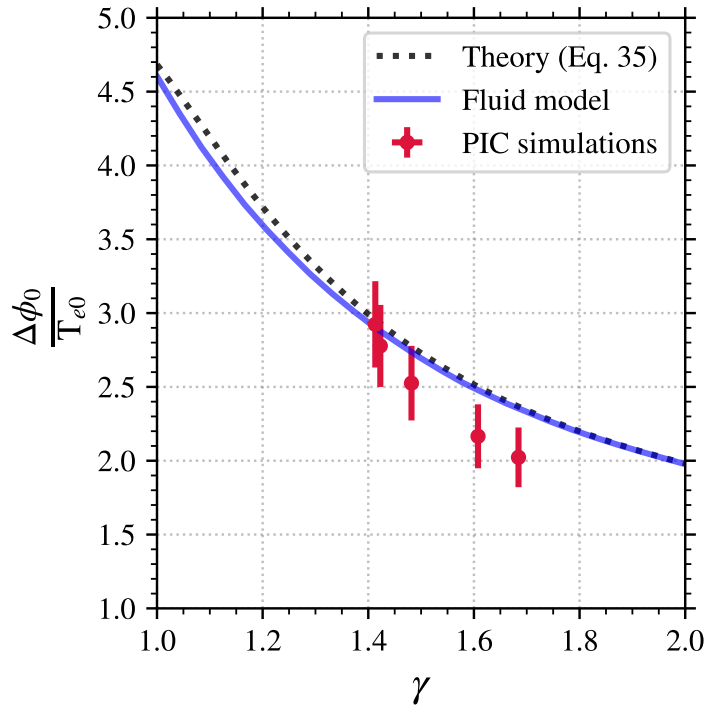


FIGURE 3.15 – Evolution of the potential drop normalized to the electron temperature as a function of the polytropic index γ from the theory of Eq. (3.34), from the fluid model of Section 3.5.1 and from the PIC simulations results (the same cases as in Fig. 3.10). Errors correspond to 10% .

Figure 3.15 shows the evolution of normalized plasma potential drop to the wall $\frac{\Delta\phi_0}{T_{e0}}$ as a function of γ . Error bars indicate an uncertainty of 10%. This uncertainty value corresponds to an aggregation of the numerical fluctuation of the PIC simulation (that decreases when more particles per cell are used), and the estimation of the sheath edge position. A more accurate estimation of these uncertainties would require a dedicated study with many additional simulations, hence we choose the reasonable value of 10% [60]. We can see that in the limit where $\gamma \rightarrow 1$, we find with Eq. (3.34) the usual isothermal value $\frac{\Delta\phi_0}{T_{e0}} \simeq 4.68$ for argon. The value observed in the fluid model is very close to the results of Eq. (3.34). This is due to the

very small size of the sheath, as seen in Fig. 3.4. When γ increases, $\frac{\Delta\phi_0}{T_{e0}}$ decreases significantly. The decrease of $\Delta\phi_0$ is consistent with the depletion of the high energy tail of the electrons, as the plasma needs less screening of the electrons in order to stay quasi-neutral.

Figure 3.15 also presents the potential drop measured in the same PIC simulations as presented in Fig. 3.10. The error bars correspond to an estimate of the aggregation of the uncertainties from the PIC simulation and the averages. The sheath edge is defined using the modified Bohm criterion (Eq. (3.29)), as for the fluid model. We can see a very good agreement with the theories. The trend of decreasing potential drop with increasing γ is clearly observed, and the values agree within about 10%. This is significantly more accurate than the 50% discrepancy with respect to the isothermal model.

The solutions of Eq. (3.34) can be fitted between $\gamma = 1$ and $\gamma = 2$ with a good precision ($R^2 = 0.98$) by :

$$\frac{\Delta\phi_0}{T_{e0}} = 0.7 + \frac{4.1}{\gamma^{1.7}} \quad (3.35)$$

3.5.4 Power losses at the wall

As expressed in the previous section, the electron flux to the wall is equal to the ion flux :

$$\Gamma_e = \Gamma_i = n_0 \sqrt{\frac{\gamma e T_{e0}}{m_i}} \quad (3.36)$$

with $n_{e,0}$ and T_{e0} the electron density and temperature at the sheath edge. Following the two-T_e EEDF as described in Section 3.3, the electron energy flux to the wall is a thermal flux from a Maxwellian distribution function of temperature T_{ew} . Hence it reads [?] :

$$Q_e = \Gamma_e 2T_{ew} \quad (3.37)$$

Using Eq. (3.33), we obtain

$$\frac{Q_e}{\Gamma_e} = 2T_{e0} \left[1 - \frac{(\gamma - 1)}{\gamma} \frac{\Delta\phi_0}{T_{e0}} \right] \quad (3.38)$$

with $\frac{\Delta\phi_0}{T_{e0}}$ calculated from either Eq. (3.34) or Eq. (3.35). From Eq. (3.38) we see that in the isothermal limit we find the usual $2T_e$ mean energy by electron leaving the plasma. However, for $\gamma > 1$, the mean energy by electron decreases.

Figure 3.16 shows the evolution of the average energy of electrons leaving the plasma at the wall normalized to the electron temperature in the plasma bulk from Eq. (3.38). We can see that the ratio is significantly lower than the isothermal value $\frac{Q_e}{\Gamma_e} = 2T_{e0}$ when $\gamma > 1$. Overlaid in Fig. 3.16 are the PIC simulation results. We can see that the PIC results are lower than the isothermal value, but do not agree well with Eq. (3.38). The discrepancy could be due to the two-T_e hypothesis used in Eq. (3.37). Indeed, we can see in Fig. 3.7 that there is a small population of high energy electrons. This population is not big enough to modify the electron flux to the wall, hence the potential drop [74], but may increase the mean energy of electron leaving the plasma. We tested the hypothesis for one case ($P_n = 2$ mTorr). Once the steady state was reached, we stopped generating the electron-ion couples. We observed that during a transition time of around $0.74\mu s$, the mean energy per electron decreased significantly from

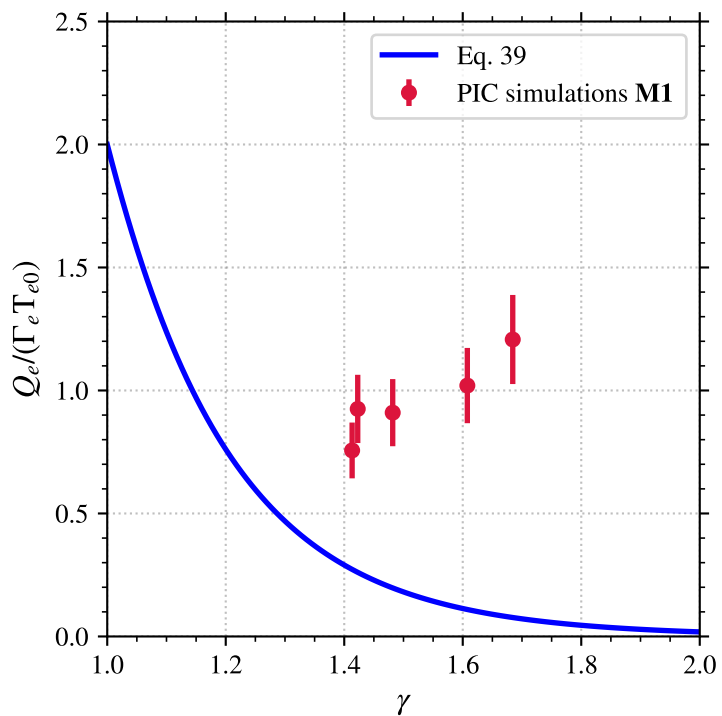


FIGURE 3.16 – Evolution of the mean energy per electron leaving the plasma at the wall normalized to the electron temperature at the sheath edge as a function of the polytropic index γ from the theory of Eq. (3.38). The simulation result (marker) corresponds to the model M1.

0.9 V to 0.3 V, while the electron flux to the wall Γ_e and the electron temperature $T_{e,0}$ was not yet affected. This is more consistent with Eq. (3.38) and seems to confirm the hypothesis, but more investigations on the heat flux are needed.

3.6 Conclusion

The usual models used to described the plasma-wall interaction have been shown to be inconsistent with the **PIC** simulation.

Using the kinetic informations of the **PIC** simulations, we have seen that the electrons are not Maxwellian, in contrast to the hypothesis of the usual models. The electron distribution function is affected by two phenomena:

- the absorption of high energy electron at the wall
- the electron-neutral scattering

The absorption depletes rapidly the high energy tail of the EEPF for energies higher than the local plasma potential relative to the wall. However, the low energy population is not affected by the wall

The collisions affect the electrons more slowly, by replenishing the high energy tail by scattering. Indeed, in the directions parallel to the wall, the high energy tail is not depleted. However, for large energies ($\epsilon > 10$ V), the electron-neutral scattering angle is small [32], hence the time scale over which the collisions impact the EEPF is much longer than the typical time between two collisions.

The electron trajectory in the discharge chamber is hence mostly collisionless. We have successfully confirmed this by confronting the EEDF measurements to the 1D stationary Vlasov equation. Following the work of Zhang et al. [63] on the collisionless evolution of non-Maxwellian electron though a potential drop, we have found that a polytropic closure for the electron describes very accurately the electron temperature evolution:

$$T_e n_e^{1-\gamma} = cst, \text{ with } \gamma \text{ the polytropic index}$$

The polytropic state law for the electron, when used in fluid model, allows to obtain the same densities and plasma potential that in the **PIC** simulation. This paves the way for a modified sheath model to compare the **2D PIC** simulation of the **HET** of Chapter 2. But for that, the electron induced secondary electron emission has to be taken into account.

3.6.1 Realistic heating and ionization

In the study used, the ionization and the heating mechanism were not physical, but allow to obtain a steady state as in the simulations of Chapter 1.

Hence, we study the impact of the wall absorption in a case of self consistent heating and ionization. The electrons are heated "inductively" with a radio-frequency (RF) electric field in the direction normal to the simulation grid [57, 75?]. The electrons are heated in the y direction, and momentum is transferred to the x and z axis via electron-neutral collisions. The heating electric field $\mathbf{E}_{rf} = E_{rf} \mathbf{e}_y$ is independent of x in the simulation domain, its frequency is 13.56 MHz, and its amplitude is adjusted in order to obtain the desired absorbed power $P_{abs} = \langle \mathbf{J}_e \cdot \mathbf{E}_{rf} \rangle$.

Parameter	value	unit
Pressure	0.1	mTorr
P_{abs}	0.25	W/m^{-3}
Length L	10	cm

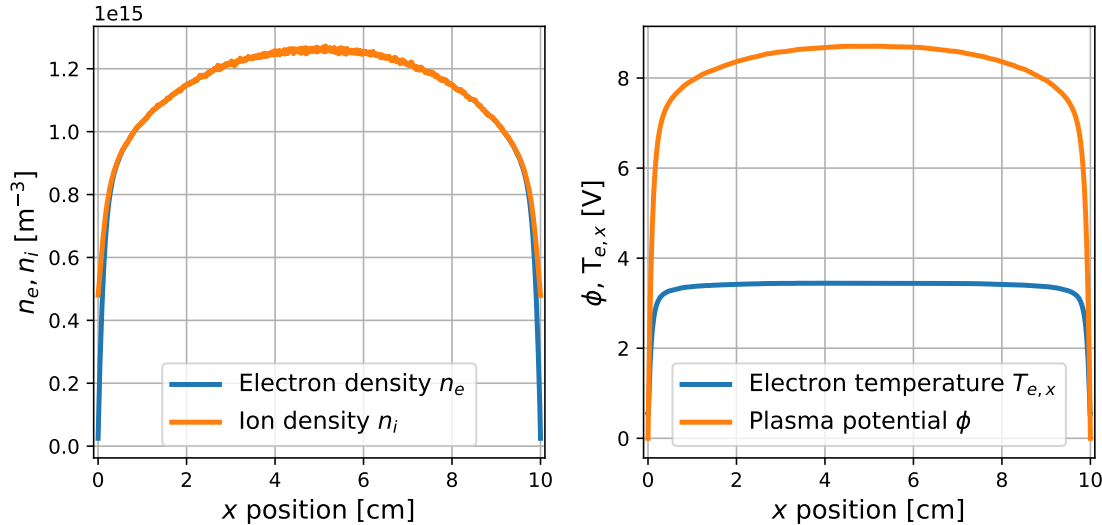
TABLE 3.2 – Input parameters for the simulation using the model **M2**.FIGURE 3.17 – Results of the PIC simulation for the model **M2**, using RF inductive heating.

Figure 3.17 presents the simulation results for the electron density, plasma potential and electron temperature using the parameters of Table 3.2. We can see that the different variables (density, electron temperature and the plasma potential) are not much affected compared to **M1**.

Figure 3.18 presents the electron pressure as a function of the electron density measured in the simulation in log scale. We see that the trend is not purely linear. Hence, the linear regression used in order to obtain the polytropic index is conducted twice:

- In the whole domain: $\gamma = 1.5$
- Only in the sheath: $\gamma = 1.6$

The linear relation conducted of the whole domain is less precise than for the simulation result of **M1** ($R^2 = 0.992$). However, we can see that the linear relation still describes quite well the electron evolution in the sheath. The polytropic indexes obtained are close to the simulation using **M1** at the same pressure.

Figure 3.19 shows the comparison of the electron temperature and the plasma potential in the PIC simulation using the model **M2** with the prediction of the fluid model of Section 3.5. We can see that the agreement between the PIC results and the fluid models is less satisfactory than in Fig. 3.14 when using the model **M1**, but it is still significantly better than the isothermal model. Hence, even with a self-consistent heating and ionization in the plasma, the polytropic model stands as a better model for the sheath and the pre-sheaths.

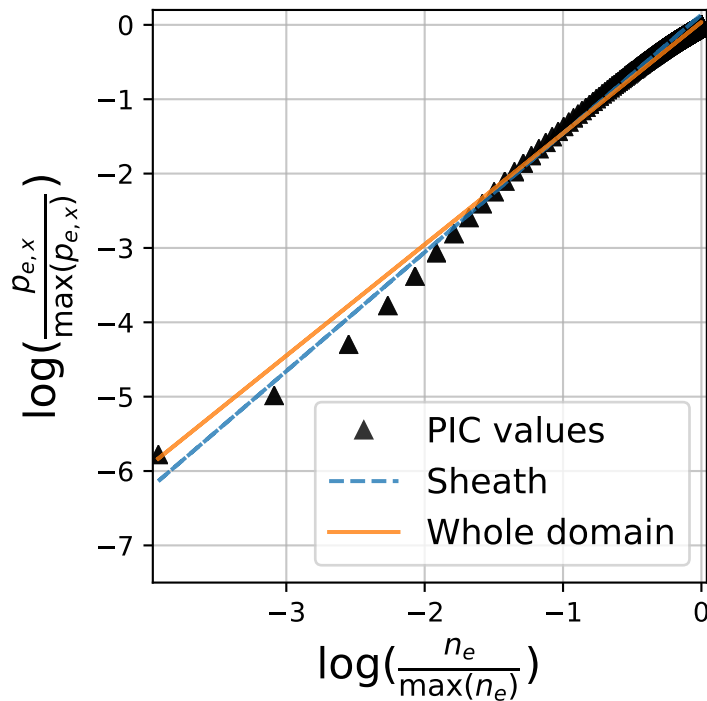


FIGURE 3.18 – Estimation of the polytropic index in the sheath and in the whole domain in the PIC simulation using the model **M2**.

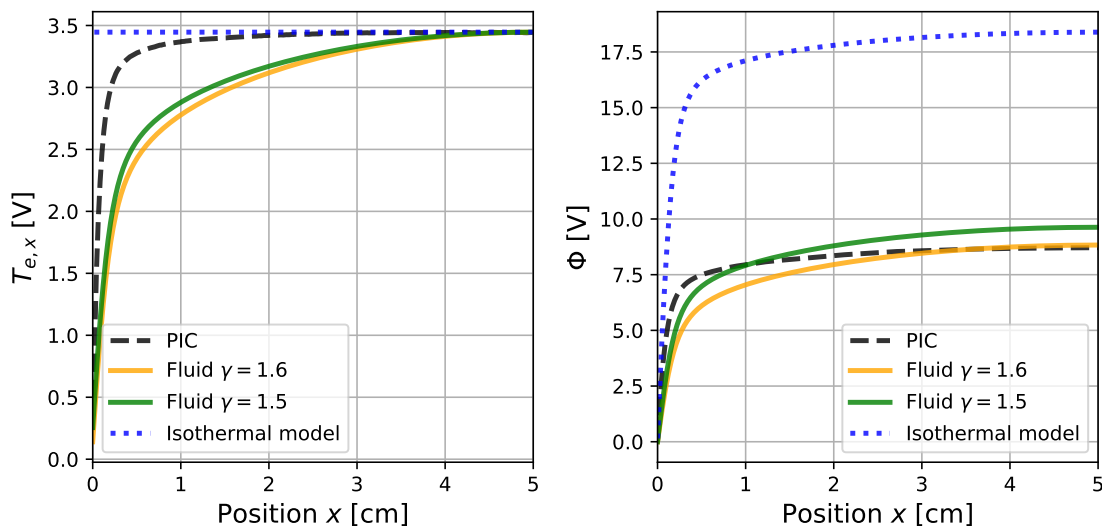


FIGURE 3.19 – Comparison of the electron temperature and plasma potential measured in the PIC simulation with the prediction of the fluid model with $\gamma = 1.5$ (average index in the domain) and $\gamma = 1.6$ (index in the sheath).

Annexe A

Bibliographie

- [1] u/ucarion. R/space - I made a delta-v subway map of the Solar System. www.reddit.com/r/space/comments/29cxi6/i_made_a_deltav_subway_map_of_the_solar_system/. 2
- [2] Kathleen A. Zona. NASA - Liquid Hydrogen—the Fuel of Choice for Space Exploration. www.nasa.gov/topics/technology/hydrogen/hydrogen_fuel_of_choice.html. 3
- [3] C Charles. Plasmas for spacecraft propulsion. *Journal of Physics D : Applied Physics*, 42(16) :163001, 2009. doi : 10.1088/0022-3727/42/16/163001. 3
- [4] Stéphane Mazouffre. Electric propulsion for satellites and spacecraft : Established technologies and novel approaches. *Plasma Sources Science and Technology*, 25(3) :033002, 2016. doi : 10.1088/0963-0252/25/3/033002. 3
- [5] Dan Lev, Roger M. Myers, Kristina M. Lemmer, Jonathan Kolbeck, Hiroyuki Koizumi, and Kurt Polzin. The technological and commercial expansion of electric propulsion. *Acta Astronautica*, 2019. doi : 10.1016/j.actaastro.2019.03.058. 3
- [6] J Vaudolon, V Vial, N Cornu, and I Habbassi. PPS-X00 Hall Thruster Development at Safran. In *IAC*, Bremen, Germany, 2018. doi : IAC-18-C4.4.9x45869. 5, 6
- [7] C Boniface, J.C Charbonner, L Lefebvre, V Leroi, and T Lienart. An Overview of electric propulsion activities at CNES. In *IEPC*, Geaorgia Institute of Technology, Atlanta, Geaorgia, USA, 2017. 5, 9
- [8] Olivier Duchemin, Julien Rabin, Lahib Balika, Mathieu Diome, Jean-Marie Lonchard, and Xavier Cavelan. Development Status of the \PPS5000 Hall Thruster Unit. In *IEPC-2017-415*, Georgia Institute of Technology, Atlanta, Georgia, USA, 2017. 5
- [9] Vivien Croes. *Modélisation bidimensionnelle de la décharge plasma dans un propulseur de Hall*. PhD thesis, Université Paris-Saclay, 2017. 6, 30, 31, 33, 39, 66, 67
- [10] Vivien Croes, Trevor Lafleur, Zdeněk Bonaventura, Anne Bourdon, and Pascal Chabert. 2D particle-in-cell simulations of the electron drift instability and associated anomalous electron transport in Hall-effect thrusters. *Plasma Sources Science and Technology*, 26(3) :034001, 2017. doi : 10.1088/1361-6595/aa550f. 6, 22, 23, 30

- [11] Vivien Croes, Antoine Tavant, Romain Lucken, Roberto Martorelli, Trevor Lafleur, Anne Bourdon, and Pascal Chabert. The effect of alternative propellants on the electron drift instability in Hall-effect thrusters : Insight from 2D particle-in-cell simulations. *Physics of Plasmas*, 25(6) :063522, 2018. doi : 10.1063/1.5033492. 6
- [12] Nathan B. Meezan, William A. Hargus, and Mark A. Cappelli. Anomalous electron mobility in a coaxial Hall discharge plasma. *Physical Review E*, 63(2), 2001. doi : 10.1103/PhysRevE.63.026410. 6, 16
- [13] N. Gascon, M. Dudeck, and S. Barral. Wall material effects in stationary plasma thrusters. I. Parametric studies of an SPT-100. *Physics of Plasmas*, 10(10) :4123–4136, 2003. doi : 10.1063/1.1611880. 7
- [14] S. Barral, K. Makowski, Z. Peradzyński, N. Gascon, and M. Dudeck. Wall material effects in stationary plasma thrusters. II. Near-wall and in-wall conductivity. *Physics of Plasmas*, 10(10) :4137–4152, 2003. doi : 10.1063/1.1611881. 8, 10, 39, 40, 54
- [15] L Landau. On the vibrations of the electronic plasma. *Journal of Physics*, X(1) :25–34, 1945. doi : doi.org/10.1016/B978-0-08-010586-4.50066-3. 8
- [16] J. H. Malmberg and C. B. Wharton. Collisionless Damping of Electrostatic Plasma Waves. *Physical Review Letters*, 13(6) :184–186, 1964. doi : 10.1103/PhysRevLett.13.184. 8
- [17] D. S. Filippychev. Modeling beam instability in plasma. *Computational Mathematics and Modeling*, 1(1) :71–74, 1990. doi : 10.1007/BF01128315. 9
- [18] Petr Cagas, Ammar Hakim, and Bhuvana Srinivasan. Boundary Conditions for Continuum Simulations of Wall-bounded Kinetic Plasmas. *arXiv :1906.07056 [physics]*, 2019. 9
- [19] R. W. Boswell and I. J. Morey. Self-consistent simulation of a parallel-plate rf discharge. *Applied Physics Letters*, 52(1) :21–23, 1988. doi : 10.1063/1.99327. 9
- [20] Seiji Samukawa, Masaru Hori, Shahid Rauf, Kunihide Tachibana, Peter Bruggeman, Gerrit Kroesen, J Christopher Whitehead, Anthony B Murphy, Alexander F Gutsol, Svetlana Starikovskaia, Uwe Kortshagen, Jean-Pierre Boeuf, Timothy J Sommerer, Mark J Kushner, Uwe Czarnetzki, and Nigel Mason. The 2012 Plasma Roadmap. *Journal of Physics D : Applied Physics*, 45(25) :253001, 2012. doi : 10.1088/0022-3727/45/25/253001. 9
- [21] Paul Lascombes. Electric Propulsion For Small Satellites Orbit Control And Deorbiting : The Example Of A Hall Effect Thruster. In *15th International Conference on Space Operations*, Marseille, France, 2018. American Institute of Aeronautics and Astronautics. ISBN 978-1-62410-562-3. doi : 10.2514/6.2018-2729. 9
- [22] I Adamovich, S D Baalrud, A Bogaerts, P J Bruggeman, M Cappelli, V Colombo, U Czarnetzki, U Ebert, J G Eden, P Favia, D B Graves, S Hamaguchi, G Hieftje, M Hori, I D Kaganovich, U Kortshagen, M J Kushner, N J Mason, S Mazouffre, S Mededovic Thagard, H-R Metelmann, A Mizuno, E Moreau, A B Murphy, B A Niemira, G S Oehrlein, Z Lj Petrovic, L C Pitchford, Y-K Pu, S Rauf, O Sakai, S Samukawa, S Starikovskaia, J Tennyson, K Terashima, M M Turner, M C M van de Sanden, and A Vardelle. The 2017 Plasma Roadmap : Low temperature plasma science and technology. *Journal of Physics D : Applied Physics*, 50(32) :323001, 2017. doi : 10.1088/1361-6463/aa76f5. 9

- [23] J C Adam, J P Boeuf, N Dubuit, M Dukeck, L Garrigues, D Gresillon, A Heron, G J M Hagelaar, V Kulaev, N Lemoine, S Mazouffre, J Perez Luna, V Pisarev, and S Tsikata. Physics, simulation and diagnostics of Hall effect thrusters. *Plasma Physics and Controlled Fusion*, 50(12) :124041, 2008. doi : 10.1088/0741-3335/50/12/124041. [9](#), [41](#)
- [24] T. Lafleur, S. D. Baalrud, and P. Chabert. Theory for the anomalous electron transport in Hall effect thrusters. I. Insights from particle-in-cell simulations. *Physics of Plasmas*, 23(5) :053502, 2016. doi : 10.1063/1.4948495. [9](#), [16](#), [22](#), [23](#), [29](#), [30](#), [31](#), [32](#), [41](#), [51](#)
- [25] Y Raitses, I D Kaganovich, A Khrabrov, D Sydorenko, N J Fisch, and A Smolyakov. Effect of Secondary Electron Emission on Electron Cross-Field Current in \$E \times B\$ Discharges. *IEEE Transactions on Plasma Science*, 39(4) :995–1006, 2011. doi : 10.1109/TPS.2011.2109403. [10](#), [66](#)
- [26] Dmytro Sydorenko. Particle-in-Cell Simulations of Electron Dynamics in Low Pressure Discharges with Magnetic Fields. page 230, 2006. [10](#), [67](#)
- [27] G. Fubiani, L. Garrigues, and J. P. Boeuf. Modeling of negative ion extraction from a magnetized plasma source : Derivation of scaling laws and description of the origins of aberrations in the ion beam. *Physics of Plasmas*, 25(2) :023510, 2018. doi : 10.1063/1.4999707. [10](#)
- [28] Francesco Taccogna, Pierpaolo Minelli, Mario Capitelli, and Savino Longo. Physics of Hall-effect thruster by particle model. pages 1390–1399, 2012. doi : 10.1063/1.4769702. [10](#)
- [29] Francis F. Chen and Francis F. Chen. *Plasma Physics*. Number Francis F. Chen ; Vol. 1 in Introduction to Plasma Physics and Controlled Fusion. Springer US, New York, 2. ed., 5. printing edition, 2006. ISBN 978-0-306-41332-2. OCLC : 836567560. [16](#)
- [30] Hiroko Ueda, Yoshiharu Omura, Hiroshi Matsumoto, and Takashi Okuzawa. A study of the numerical heating in electrostatic particle simulations. *Computer physics communications*, 79(2) :249–259, 1994. [17](#)
- [31] Salomon Janhunen, Andrei Smolyakov, Dmytro Sydorenko, Marilyn Jimenez, Igor Kaganovich, and Yevgeny Raitses. Evolution of the electron cyclotron drift instability in two-dimensions. *Physics of Plasmas*, 25(8) :082308, 2018. doi : 10.1063/1.5033896. [17](#), [22](#), [51](#), [67](#)
- [32] V. Vahedi, M. A. Lieberman, G. DiPeso, T. D. Rognlien, and D. Hewett. Analytic model of power deposition in inductively coupled plasma sources. *Journal of Applied Physics*, 78 (3) :1446–1458, 1995. doi : 10.1063/1.360723. [17](#), [81](#), [89](#)
- [33] LXCat project, www.lxcat.net. [17](#)
- [34] Phelps database, www.lxcat.net. retrieved on November 16 2016. [18](#)
- [35] Cross sections extracted program {MAGBOLTZ}. version 7.1 june 2016. [18](#)

- [36] C. K. Birdsall. Particle-in-cell charged-particle simulations, plus Monte Carlo collisions with neutral atoms, PIC-MCC. *IEEE Transactions on Plasma Science*, 19(2) :65–85, 1991. doi : 10.1109/27.106800. [19](#), [20](#), [81](#)
- [37] J Boris. Relativistic plasma simulation-optimization of a hybrid code. In *Fourth Conference on Numerical Simulations of Plasmas*, 1970. [20](#)
- [38] A. Héron and J. C. Adam. Anomalous conductivity in Hall thrusters : Effects of the non-linear coupling of the electron-cyclotron drift instability with secondary electron emission of the walls. *Physics of Plasmas*, 20(8) :082313, 2013. [21](#), [22](#), [51](#), [67](#)
- [39] A Domínguez-Vázquez, F Taccogna, and E Ahedo. Particle modeling of radial electron dynamics in a controlled discharge of a Hall thruster. *Plasma Sources Science and Technology*, 27(6) :064006, 2018. doi : 10.1088/1361-6595/aac968. [21](#), [22](#), [69](#)
- [40] Oliver C. Ibe. 9 - Brownian Motion. In Oliver C. Ibe, editor, *Markov Processes for Stochastic Modeling (Second Edition)*, pages 263–293. Elsevier, Oxford, 2013. ISBN 978-0-12-407795-9. doi : 10.1016/B978-0-12-407795-9.00009-8. [35](#)
- [41] Marc Villemant. *Modélisation et caractérisation expérimentale de l'influence de l'émission électronique sur le fonctionnement des propulseurs à courant de Hall*. PhD thesis. [38](#), [54](#)
- [42] M. Furman and M. Pivi. Probabilistic model for the simulation of secondary electron emission. *Physical Review Special Topics - Accelerators and Beams*, 5(12), 2002. doi : 10.1103/PhysRevSTAB.5.124404. [39](#)
- [43] J. Pierron, C. Inguimbert, M. Belhaj, T. Gineste, J Puech, and M. Raine. Electron emission yield for low energy electrons : Monte Carlo simulation and experimental comparison for Al, Ag, and Si. *Journal of Applied Physics*, 121(21) :215107, 2017. doi : 10.1063/1.4984761. [39](#)
- [44] J.R.M. Vaughan. A new formula for secondary emission yield. *IEEE Transactions on Electron Devices*, 36(9) :1963–1967, Sept./1989. doi : 10.1109/16.34278. [39](#)
- [45] D. Sydorenko, A. Smolyakov, I. Kaganovich, and Y. Raitses. Modification of electron velocity distribution in bounded plasmas by secondary electron emission. *IEEE Transactions on Plasma Science*, 34(3) :815–824, 2006. doi : 10.1109/TPS.2006.875727. [39](#)
- [46] G D Hobbs and J A Wesson. Heat flow through a Langmuir sheath in the presence of electron emission. *Plasma Physics*, 9(1) :85–87, 1967. doi : 10.1088/0032-1028/9/1/410. [42](#), [43](#), [59](#), [61](#), [64](#)
- [47] E. Ahedo and F. I. Parra. Partial trapping of secondary-electron emission in a Hall thruster plasma. *Physics of Plasmas*, 12(7) :073503, 2005. doi : 10.1063/1.1943327. [42](#)
- [48] E. Ahedo. Presheath/sheath model with secondary electron emission from two parallel walls. *Physics of Plasmas*, 9(10) :4340–4347, 2002. doi : 10.1063/1.1503798. [42](#)
- [49] Dan M Goebel and Ira Katz. Fundamentals of Electric Propulsion : Ion and Hall Thrusters. page 493. [43](#), [59](#)

- [50] T. Lafleur, S. D. Baalrud, and P. Chabert. Theory for the anomalous electron transport in Hall effect thrusters. II. Kinetic model. *Physics of Plasmas*, 23(5) :053503, 2016. doi : 10.1063/1.4948496. 51
- [51] A. I. Morozov. Wall conduction in a highly magnetized plasma. *Journal of Applied Mechanics and Technical Physics*, 9(3) :249–251, 1972. doi : 10.1007/BF00916781. 57
- [52] Y. Raitses, D. Staack, A. Smirnov, and N. J. Fisch. Space charge saturated sheath regime and electron temperature saturation in Hall thrusters. *Physics of Plasmas*, 12(7) :073507, 2005. doi : 10.1063/1.1944328. 59
- [53] Ira B. Bernstein and T. Holstein. Electron Energy Distributions in Stationary Discharges. *Physical Review*, 94(6) :1475–1482, 1954. doi : 10.1103/PhysRev.94.1475. 69
- [54] V. A. Godyak and R. B. Piejak. Paradoxical spatial distribution of the electron temperature in a low pressure rf discharge. *Applied Physics Letters*, 63(23) :3137–3139, 1993. doi : 10.1063/1.110227. 69
- [55] S Mouchtouris and G Kokkoris. A hybrid model for low pressure inductively coupled plasmas combining a fluid model for electrons with a plasma-potential-dependent energy distribution and a fluid-Monte Carlo model for ions. *Plasma Sources Science and Technology*, 25(2) :025007, 2016. doi : 10.1088/0963-0252/25/2/025007. 69, 71
- [56] V A Godyak, R B Piejak, and B M Alexandrovich. Electron energy distribution function measurements and plasma parameters in inductively coupled argon plasma. *Plasma Sources Science and Technology*, 11(4) :525–543, 2002. doi : 10.1088/0963-0252/11/4/320. 69
- [57] Albert Meige and Rod W. Boswell. Electron energy distribution functions in low-pressure inductively coupled bounded plasmas. *Physics of Plasmas*, 13(9) :092104, 2006. doi : 10.1063/1.2339024. 69, 71, 89
- [58] I. Kaganovich, M. Mišina, S. V. Berezhnoi, and R. Gijbels. Electron Boltzmann kinetic equation averaged over fast electron bouncing and pitch-angle scattering for fast modeling of electron cyclotron resonance discharge. *Physical Review E*, 61(2) :1875–1889, 2000. doi : 10.1103/PhysRevE.61.1875. 69
- [59] I. D. Kaganovich, Y. Raitses, D. Sydorenko, and A. Smolyakov. Kinetic effects in a Hall thruster discharge. *Physics of Plasmas*, 14(5) :057104, 2007. doi : 10.1063/1.2709865. 69, 71, 78
- [60] M. M. Turner, A. Derzsi, Z. Donkó, D. Eremin, S. J. Kelly, T. Lafleur, and T. Mussenbrock. Simulation benchmarks for low-pressure plasmas : Capacitive discharges. *Physics of Plasmas*, 20(1) :013507, 2013. doi : 10.1063/1.4775084. 70, 86
- [61] Pascal Chabert and Nicholas Braithwaite. *Physics of Radio-Frequency Plasmas*. 70
- [62] T Lafleur, C Charles, and R W Boswell. Electron temperature characterization and power balance in a low magnetic field helicon mode. *Journal of Physics D : Applied Physics*, 44(18) :185204, 2011. doi : 10.1088/0022-3727/44/18/185204. 71

- [63] Yunchao Zhang, Christine Charles, and Rod Boswell. A POLYTROPIC MODEL FOR SPACE AND LABORATORY PLASMAS DESCRIBED BY BI-MAXWELLIAN ELECTRON DISTRIBUTIONS. *The Astrophysical Journal*, 829(1) :10, 2016. doi : 10.3847/0004-637X/829/1/10. [71](#), [75](#), [78](#), [89](#)
- [64] S. Kuhn, K.-U. Riemann, N. Jelić, D. D. Tskhakaya, D. Tskhakaya, and M. Stanojević. Link between fluid and kinetic parameters near the plasma boundary. *Physics of Plasmas*, 13(1) :013503, 2006. doi : 10.1063/1.2161181. [78](#)
- [65] N. Jelić, K.-U. Riemann, T. Gyergyek, S. Kuhn, M. Stanojević, and J. Dušovnik. Fluid and kinetic parameters near the plasma-sheath boundary for finite Debye lengths. *Physics of Plasmas*, 14(10) :103506, 2007. doi : 10.1063/1.2793737. [78](#)
- [66] M. J. Kushner. Monte-Carlo simulation of electron properties in rf parallel plate capacitively coupled discharges. *Journal of Applied Physics*, 54(9) :4958–4965, 1983. doi : 10.1063/1.332763. [79](#)
- [67] P Chabert. What is the size of a floating sheath ? *Plasma Sources Science and Technology*, 23(6) :065042, 2014. doi : 10.1088/0963-0252/23/6/065042. [79](#)
- [68] P. Y. Lai, T. Y. Lin, Y. R. Lin-Liu, and S. H. Chen. Numerical thermalization in particle-in-cell simulations with Monte-Carlo collisions. *Physics of Plasmas*, 21(12) :122111, 2014. doi : 10.1063/1.4904307. [81](#)
- [69] John M. Dawson. Thermal Relaxation in a One-Species, One-Dimensional Plasma. *Physics of Fluids*, 7(3) :419, 1964. doi : 10.1063/1.1711214. [81](#)
- [70] David Montgomery. Thermal Relaxation in One- and Two-Dimensional Plasma Models. *Physics of Fluids*, 13(5) :1405, 1970. doi : 10.1063/1.1693081. [81](#)
- [71] M. M. Turner. Kinetic properties of particle-in-cell simulations compromised by Monte Carlo collisions. *Physics of Plasmas*, 13(3) :033506, 2006. doi : 10.1063/1.2169752. [81](#)
- [72] K.-U. Riemann, J. Seebacher, D. D. Tskhakaya Sr, and S. Kuhn. The plasma-sheath matching problem. *Plasma Physics and Controlled Fusion*, 47(11) :1949, 2005. doi : 10.1088/0741-3335/47/11/006. [84](#)
- [73] K U Riemann. The Bohm criterion and sheath formation. *Journal of Physics D : Applied Physics*, 24(4) :493–518, 1991. doi : 10.1088/0022-3727/24/4/001. [84](#)
- [74] V. Demidov, C. DeJoseph, and A. Kudryavtsev. Anomalously High Near-Wall Sheath Potential Drop in a Plasma with Nonlocal Fast Electrons. *Physical Review Letters*, 95 (21), 2005. doi : 10.1103/PhysRevLett.95.215002. [87](#)
- [75] R. Lucken, V. Croes, T. Lafleur, J.-L. Raimbault, A. Bourdon, and P. Chabert. Edge-to-center plasma density ratios in two-dimensional plasma discharges. *Plasma Sources Science and Technology*, 27(3) :035004, 2018. doi : 10.1088/1361-6595/aaaf61. [89](#)

